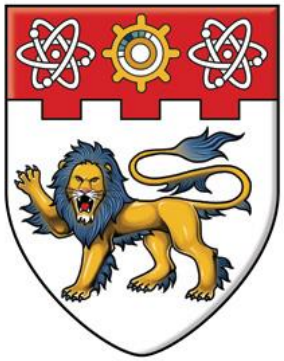

NANYANG TECHNOLOGICAL UNIVERSITY

Nanosheets of Iron-based Compounds: Synthesis and Their Lithium Storage Properties

XU CHEN

SCHOOL OF MATERIALS SCIENCE AND ENGINEERING

2014

Nanosheets of Iron-based Compounds: Synthesis and Their Lithium Storage Properties

Xu Chen

SCHOOL OF MATERIALS SCIENCE AND ENGINEERING

A thesis submitted to the Nanyang Technological University in partial fulfillment of the requirement for the degree of

Doctor of Philosophy

2014

Acknowledgement

First of all, I would like to thank my supervisor A/P Alex Yan Qingyu, who has offered continuous guidance and support throughout my PHD study.

I sincerely thank Professor Subodh Mhaisalkar, who introduced me to this project. I would also thank the principle investigator Professor Harry Hoster from TUM CREATE and Professor Rachid Yazami for their valuable advice.

I would like to acknowledge our collaborators professor Juan Bisquert, associate professor Germà Garcia Belmonte, researcher Antonio Guerrero and Juan Toribio from James I University, Spain. They conducted fitting of the EIS spectrum and proposed a new model to study the conversion reaction of reversible lithium storage.

I sincerely thank my brilliant present and previous seniors Dr. Zhou Wenwen, Dr. Zhu Jixin, Dr. Lu Ziyang, Dr. Zeng Yi, Dr. Chen Jing, Dr. Xiao Ni, Dr. Zhao Weiyun, Dr. Shi Wenhui and Mr. Sim Daohao who have shared with me their valuable experience on hands-on experiment design and knowledge on material selection, materials characterization and battery assembly and testing. The PHD journey has been sometimes depressing. I would like to thank my labmates Ms. Tan Huiteng, Ms. Liu Weiling, Ms. Yin Lisha, Ms. Ko Yahwen and Mr. Zhang Wenyu, who make my PHD journey enjoyable and whose friendship I would cherish forever.

I would like to say special thanks to my parents, who have always believed in me and offer unconditional and constant support as I grow up. I would also like to thank my husband Mr. Wang Hao who supports every decision I have made and comforts me during any stressful situations. Last but not least, I would like to dedicate the thesis to my son, wishing him grow up to be a healthy and loving person.

Table of Contents

List of Figures

List of Tables

Abstract

Future applications of energy storage devices require electrode materials with higher energy and power densities, better cycling stability and better rate capability. Many bulk and micrometer-sized electrode materials have failed to satisfy the high requirements. Therefore, design and fabrication of various novel nanostructures with controlled morphology, size, composition and crystallinity have attracted increasing research attention.

Two-dimensional (2D) nanostructures are suitable for energy storage because of their large surface area and shorter paths for fast charge transport. Nanosheets of some single-morphology, single-component, and well-crystalline electrode materials have been developed to possess improved lithium storage properties in capacity and cycling stability compared with their bulk counterparts.

In this present work, the optimizations of electrode materials are extended to fabrication and electrochemical characterization of hierarchically-constructed nanosheets, composite hierarchical nanosheets and amorphous nanosheets. The focus is to develop facial and controllable approaches for fabrication of these novel electrode materials. The hierarchical nanosheets and hybrid nanosheets are expected to benefit from the multi-functionality and advantageous of individual nanostructures or constituent components, leading to higher capacity, improved cycling stability and rate capability. The amorphization of electrode materials tends to demonstrated distinct lithium storage mechanism and kinetics compared with their crystalline counterparts.

At first, the morphology advantages of hierarchically-constructed FeS nanosheets are demonstrated. The carbon coated FeS nanosheet hierarchically constructed by small nanograins is prepared via a surfactant-directed solution-based synthesis. Results indicate that hierarchical FeS particles and hexagonal-shaped FeS nanoplates could also be obtained by adjusting the experimental conditions. The hierarchical FeS nanosheet delivers promising lithium storage property of a specific capacity of 233 mAh g^{-1} in 100^{th} cycle at a 10C discharge rate. It is proposed that the constituent nanograins offer large electrode-electrolyte interaction area and shorter charge transport. At the same time, the flexible nanosheets can effectively accommodate large volume change induced during the charge/discharge process the nanosheets holding nanograins can maximize the electrical connectivity. In addition, in-situ formed amorphous carbon coating further improves the cycling stability by absorbing and trapping polysulfides generated during the conversion reaction of sulfides preventing the dissolution of polysulfide from deteriorating ionic conductivity of electrolyte.

Next, hybrid hierarchical nanosheets composed of Troilite FeS and Wurzite ZnS have been synthesized via the same organic solution-based synthesis. The compositional ratio of FeS and ZnS can be varied by varying the compositional ratio in precursor. Among the synthesized samples with varying ratios, sample with Fe/Zn = 7.29:1 shows best lithium storage properties over other ratios and pure FeS nanosheets in terms of capacity and rate capability. The improved lithium storage performance of hybrid hierarchical nanosheet can be attributed to: (1) the advantageous hierarchical nanosheet structure provides better stress tolerance for both conversion reaction and alloying reaction upon cycling; (2) each nanosheet are composed of fine building

blocks of FeS and ZnS nanocrystals, which offers shorter diffusion path for charge transport; (3) The co-presence of the heterogeneous sulfides could behave as dispersants to each other. During repeated reversible electrochemical reactions, the heterogeneous metals reduced from the composite sulfides during lithiation are not liable to aggregate, nor are the heterogeneous sulfides formed during delithiation.

Finally, the combined effects of amorphization and nanostructuring on the lithium storage performance of FeOOH are investigated. In this work, amorphous FeOOH nanosheet is prepared by surfactant-assisted oxidation of self-synthesized FeS nanosheets. The resultant amorphous FeOOH nanosheets are porous and have a high BET surface area of 223 $m^2 g^{-1}$. The amorphous FeOOH nanosheet demonstrates good lithium storage capacity and superior rate capability (e.g. discharge capacity of 465 mAh g^{-1} at a current density of 2C), which can be attributed to its high surface area, porous nanostructure and loose amorphous nature. When characterized as lithium storage electrode, it has conversion reaction with Li^+. A new equivalent circuit directly modeling conversion reaction between electrode and Li^+ is proposed. The conversion reaction subcircuit reproduces the hysteresis in the discharge/charge voltage profile, indicating that the lithium storage via conversion reaction in amorphous FeOOH has a thermodynamic origin rather than being limited by Li transport.

1. Introduction

1.1 Background

Today, with greater projected energy demand and increasingly serious environmental pollution, renewable energy sources are gradually replacing burning fuels to produce electricity. Current renewable electricity generation systems, such as wind and photovoltaic devices, still need additional flexibility to meet users' demand. Generation of sustainable energies from their respective sources fluctuates with time and weather conditions; hence the use of electricity produced from sustainable energy sources requires efficient and stable storage.[1]

Lithium ion batteries (LIBs) are attractive over other energy storage systems in terms of energy and powder densities, environmental impact, no memory effect and flexibility in manufacturing.[2] Lithium storage properties of electrode materials determine the overall performance of LIBs. LIBs of higher energy and power densities and capable of fast charging are required for future applications. Therefore, lithium storage materials with higher energy and power densities, better cycling stability, better rate capability and better cost-effectiveness are in great demand.

Many bulk and micrometer-sized electrode materials have failed to satisfy the high requirements. Research has moved to design, fabrication and characterization of various novel nanostructures with controlled and beneficial nanostructure morphology and sizes. Nanosheets are especially suitable for lithium storage because of their maximized exposed area, minimized path length enabling faster charge transport and

their flexibility to accommodate stress induced during prolonged cycling. And in literature, Nanosheets of some single-morphology, single-component, and well-crystalline lithium storage materials have been developed and demonstrated to possess improved lithium storage properties in capacity and cycling stability compared with their bulk counterparts. However, there is still room for property improvement of lithium storage material with more complex morphology, more favorable compositions and crystallinity.

Inspired by the present research gap, in this present work, the optimizations of lithium storage materials are extended to fabrication and electrochemical characterization of nanosheets of hierarchical construction, two constituent compositions and amorphous loose structure. We put ahead several hypothesis that hierarchical nanosheets and composite nanosheets can benefit from the multi-functionality and advantageous of their constituent nanostructures or components, leading to property enhancement. And, amorphization of materials tends to demonstrate distinct lithium storage mechanism and kinetics compared with their crystalline counterparts. And, it is important to develop facial and controllable approaches for fabrication of these novel electrode materials and investigate how the morphology, composition and crystallinity can be tuned to enhance of lithium storage property of materials.

1.2 Literature Review

1.2.1 Energy Storage Systems

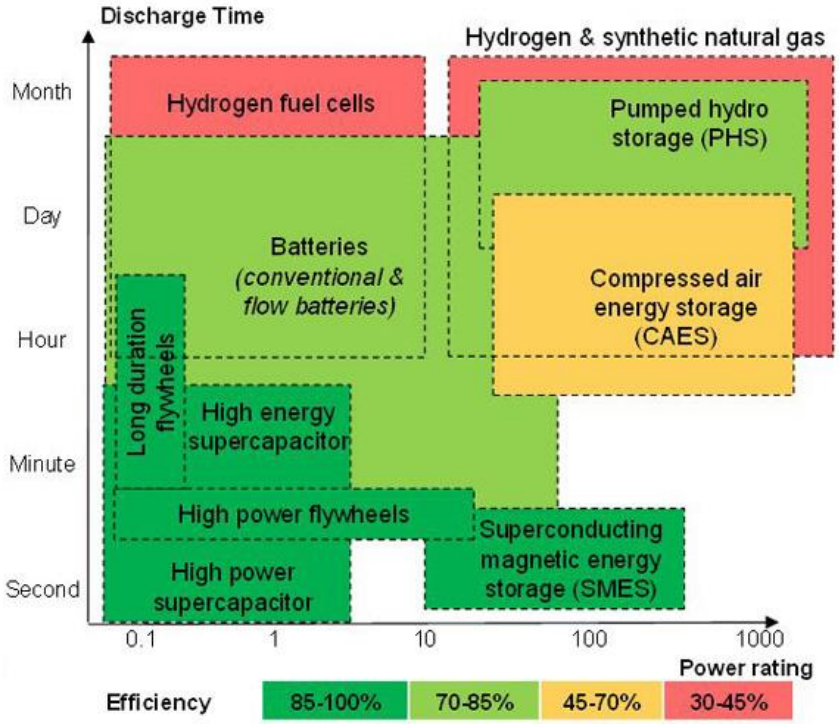

Figure 1-1: Illustration of electricity storage systems with varying power ratings, discharge time and efficiency[1]

Electricity storage systems offer more convenient and flexible connections between base-load electricity generation systems and the end-user market. Electricity storage systems vary in uses depending on their power ratings (energy and power densities), discharge time and response time as illustrated in Figure 1-1. Electrochemical energy storage system includes rechargeable batteries and supercapacitors, which are important for two challenging applications: electrochemical power source for propulsion and load leveling (i.e. electricity storage from renewable sources).[3]

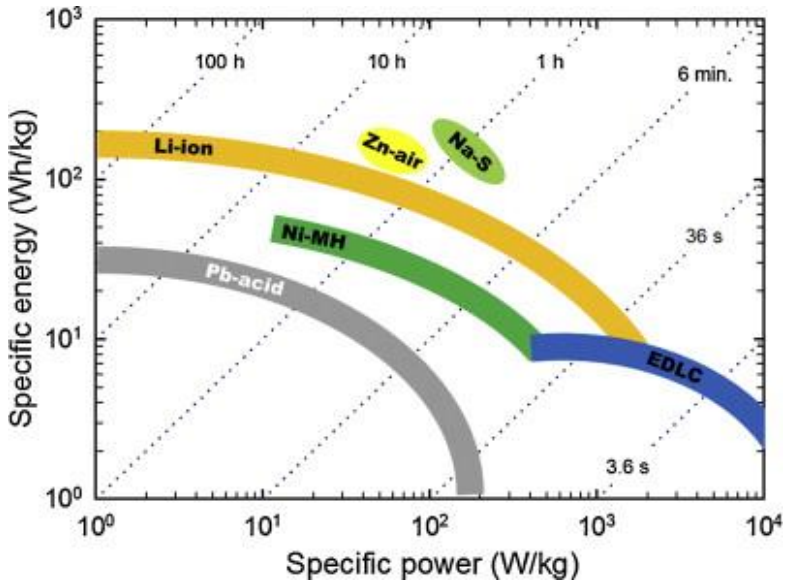

Figure 1-2: Ragone plot comparing the specific energy and power densities of several rechargeable batteries and supercapacitors (EDLCs)[3]

Based on their applications, both rechargeable batteries and supercapacitors are evaluated based on their specific energy and power densities. Figure 1-2 provides a Ragone plot illustrating the specific energy and power densities of several families of rechargeable batteries and supercapacitors (electrochemical double layer capacitors). Comparing with EDLCs, rechargeable batteries encompass a wider range of specific energy densities and discharge time for various practical applications to maximize efficiency of energy use. Rechargeable batteries have reversible electrochemical reaction during repeated charge and discharge process. Besides, they are more cost-effective and eco-friendly than primary batteries.[4] Nowadays commercially

available rechargeable battery systems include lead-acid battery, NiCd battery, NiMH (nickel metal hydride) battery and lithium ion batteries.[4]

1.2.2 Lithium Ion Batteries

Lithium ion batteries (LIBs) are advantageous over other rechargeable batteries in terms of energy and powder densities, environmental impact, no memory effect and flexibility in manufacturing.[2] Firstly, LIBs have higher energy density than lead-acid battery, NiCd battery and NiMH battery. Secondly, They have no memory effect (Memory effect is defined as the effect that causes the device to hold less charge as they gradually loses their maximum energy capacity after many cycles of charging/discharging, only 'remembering' the smaller charge capacity), and thus no scheduled cycling is required to prolong their lifetime. In addition, they experience much less self-discharge than Ni-based batteries. Lastly, LIBs can be made into various shapes and sized to accommodate to applications with different usage patterns, such as portable electronics.

In lithium ion batteries, the intrinsic nature of electrochemical redox reactions generally determines the specific energy and powder density limits. According to Figure 1-2, specific energy densities of lithium ion batteries range from 10 to 200 Wh kg^{-1}. However, efficient engineering of battery components are also essential for improving the energy and power densities of LIBs.

The primary concept of LIBs with reversible intercalation to oxides and graphite was firstly proposed in the 1970s by J.O. Besenhard.[5, 6] Akira Yoshino assembled the

first prototype cell with $LiCoO_2$ as cathode and carbonaceous material anode in 1985.[7] Without using metallic lithium, safety of lithium ion battery was greatly improved, which leads to its commercial release by Sony in 1991.

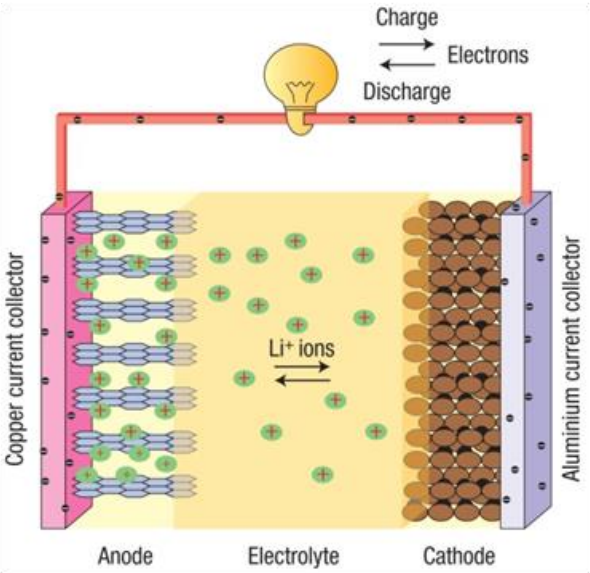

Figure 1-3: Schematic demonstration of a working lithium ion battery [8]

Lithium ion batteries are basically electrochemical cells that store and release electricity via reversible movement of Li ions between the positive electrode and the negative electrode. A typical lithium ion battery is composed of cathode, anode, Li ion conductive electrolyte and separator. The charging and discharging process of a lithium ion battery is illustrated in Figure 1-3. During charging, Li ions are extracted from the cathode side, transported through the electrolyte to the anode side. During discharging, Li ions are extracted from the anode and inserted into the cathode, while the electrons are released from the anode, flow through the external circuit to power external electronic devices. Taking the most widely commercialized lithium ion

batteries assembled with $LiCoO_2$ cathode and graphite anode as an example, the chemical reactions taking place during charge and discharge can be expressed as: [2]

Cathode: $LiCoO_2 \leftrightarrow Li_{1-x}CoO_2 + xLi^+ + xe^-$

Anode: $C + xLi^+ + xe^- \leftrightarrow Li_xC$

And, the overall reaction of the working cell during the first charge and subsequent charge/discharge cycles can be expressed as:

Initial charge: $LiCoO_2 + C \leftrightarrow Li_{1-x}CoO_2 + Li_xC$

Subsequent charge/ discharge: $Li_{1-x}CoO_2 + Li_xC \rightleftharpoons Li_{1-x+dx}CoO_2 + Li_{x-dx}C$

The total capacity of LIBs is related to the cathode capacity, anode capacity and the specific mass of other cell components including electrolyte, separator and case.[9, 10] To achieve high energy densities and power densities of lithium ion batteries for future electric vehicles, electrode materials with a superior performance have become critical for producing high-performance LIBs, particularly in terms of reducing cost while improving the functionality.

1.2.3 Lithium Storage Electrode Materials

As discussed in the previous section, energy and powder density, safety and cost of LIBs are largely dependent on the specific capacity, rate capacity, safety and cost of the electrode materials. Lithium, as a group I alkali metal, is highly reactive. Generally, electrode materials in LIBs can be classified into three categories based on their

interaction mechanism with lithium ions: intercalation, conversion reaction and alloying as illustrated in Figure 1-4.[11, 12]

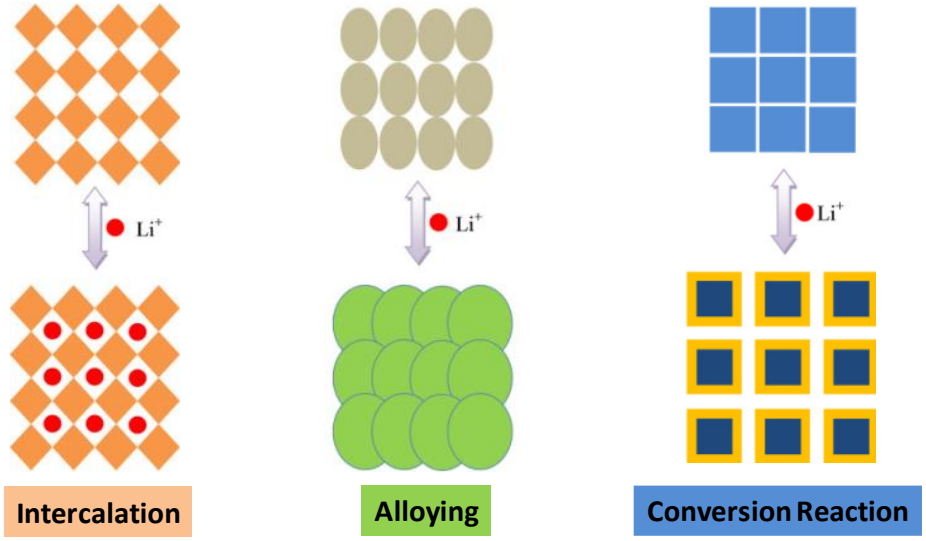

Figure 1-4: Schematic illustration of three different types of lithium storage materials [12]

1.2.3.1 Intercalation

Intercalation electrode material are electroactive with crystal structures that can serve as host solids into which lithium ions can reversibly insert from electrolyte.[13]

Cathode materials of LIBs are all of intercalation-type. The most widely employed cathode material in commercial LIBs is $LiCoO_2$ (LCO), which offers high energy density.[14, 15] LCO has layered structure with layers of lithium lying between slabs of octahedra formed by Co and O atoms, thus lithium ions can intercalate/de-intercalate between the layers without significant change in crystal structure.[11] Comparing with $LiCoO_2$, Lithium manganese oxide (LMO) is more environmental friendly but suffers from limited cyclability.[16, 17] Spinel $LiMn_{1.5}Ni_{0.5}O_4$ has a high

redox potential at around 4.8V and can reach a specific capacity of greater than 140 mAh g^{-1}.[18] Besides, the fast solid-state diffusion in spinel ensures high rate capability.[19] Another important group of novel cathodes for advanced LIBs is the layered–layered cathode materials, which is essentially a composite of $[Li_2MnO_3]_x [LiMO_2]_y$ mixing at atomic level, [20] where M = $[Mn_{0.5}Ni_{0.5}]$ or $[Mn_{0.33}Ni_{0.33}Co_{0.33}]$ and other possible combinations of transition metal cations.[21] This category of cathode materials demonstrate high capacities of greater than 250 mAh g^{-1} with a relatively low capacity fading at high rates.[21, 22] The final cathode family is olivine $LiMPO_4$ materials. The lithiation and de-lithiation of Li_xMPO_4 occur *via* first-order phase transitions. $LiFePO_4$ (LFP) is cost-effective and non-toxic, and it offers moderate energy density, which is one of the most popular cathode materials candidates in commercial LIBs.[23, 24] There are also intensive research to develop $LiMnPO_4$ and $LiCoPO_4$ as promising cathode materials with higher redox potential and hence, higher energy density.[25, 26]

Intercalation anode electrodes usually have layered crystal structure, and have Li ions diffusing along the Van Der Waals gaps between the layers. Example of such layered anode materials are graphite, anatase titanium oxide, lithium titanates and some metal sulfides (e.g. MoS_2 and WS_2).[27-29] Graphite is the mostly employed anode materials for commercial LIBs because it possesses low and flat potential plateau, good cycling stability and low-cost. However, the low theoretical capacity of graphite ~372 $mAhg^{-1}$ with the formation of LiC_6, is insufficient to meet the future energy-density demand for LIBs. Besides, the transport rate of Li ions in graphite is less than

10^{-6} cm^2s^{-1}, which results in inferior rate capacity of graphite anode and limited powder density of current LIBs.[30]

1.2.3.2 Alloying

Metals and semimetals that can electrochemically form alloys with lithium can be classified as alloying electrode materials in LIBs.[31] The specific capacities of these alloying-type materials can reach extremely high values both by weight and by volume. For example, silicon possesses a specific volumetric capacity of 8365 mAh cm^{-3} and a weight capacity of 3590 mAh g^{-1} compared to 975 mAh cm^{-3} and 372 mAh g^{-1} for graphite, respectively. However, the practical utilization of these alloying metals has been severely handicapped by the huge volume changes induced by the alloying reaction. Stresses and strains brought about by the large volume change may induce particle cracking/pulverization, which causes disconnections between active materials and current collectors, and create new surfaces that consume lithium, resulting in electronic insulation and capacity irreversibility of the overall cells.[32, 33]

1.2.3.3 Conversion Reaction

Metal oxides, metal sulfides, metal nitrides and metal phosphides can have reversible conversion reaction with Li.[34] Generally, conversion reaction can be expressed as:

$$\mathrm{M_a}X_b + (\mathrm{b}\cdot\mathrm{n})\mathrm{Li} \leftrightarrow aM + bLi_nX$$

Where M is transition metals, X is anion, and n represents formal oxidation state of X.

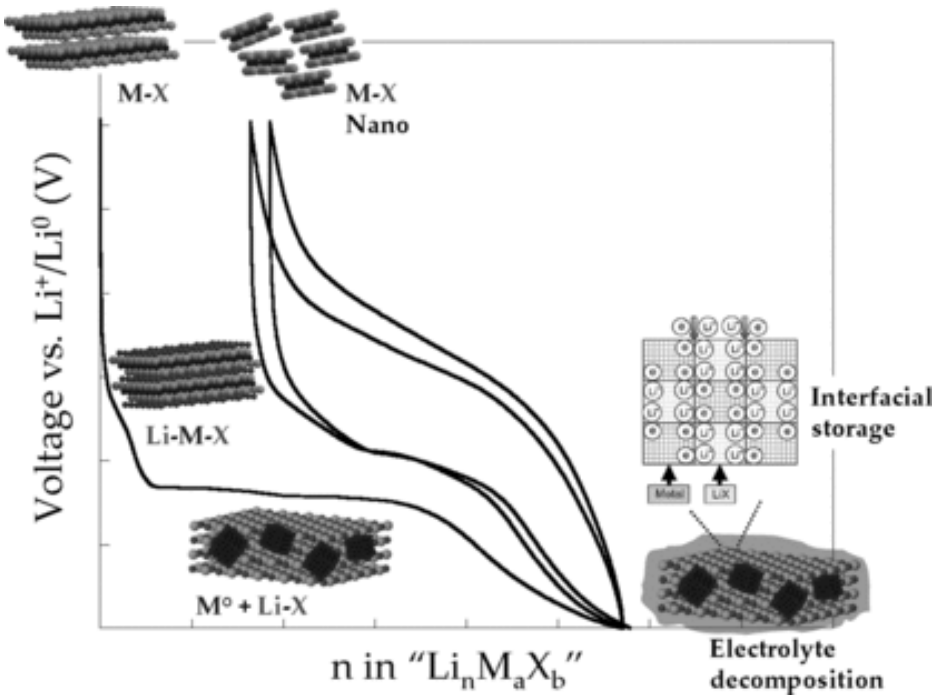

Figure 1-5: Voltage vs. composition profile of a conversion reaction electrode for the first two and half cycles. The different stages of the complex reaction are indicated. Te light grey, dark grey and black balls depict X, Li and M, respectively. Inset is the scheme of the interfacial storage mechanism[35]

The key to the reversibility of the conversion reaction lies in the formation of metal nanoparticles upon complete reduction of above-mentioned transition metal compounds, and the reduced nanoparticles are embedded in the matrix of the lithium binary compounds (Li_nX), forming with a large interfacial area.[35] When applied by a reverse polarization, metal nanoparticles are oxidized in accompany with the

decomposition of the Li_nX matrix releasing Li. The nanometric character of the metal particles is shown to sustain after repeated reduction-oxidation.[32]

Conversion reaction usually proceeds in two steps (Figure 1-5). The first step of conversion reaction is intercalation during which compounds decompose to lower binaries and Li_nX. This intermediate intercalation process indicates that direct conversion to metallic nanoparticles from binary compounds is not energetically favored.[36, 37] The second step is the real conversion reaction, during which metallic particles of 1-10 nm in size dispersing in a matrix of Li_nX is developed, and in some cases the initial morphology of compound is also preserved.[36, 37]

It can be observed that the conversion and de-conversion reaction does not show long plateau, and is replaced by a sloping curve as shown in Figure 1-5. This is attributed to remarkable change in surface area of the active material, which will react at slightly different energies compared with their bulk counterparts.[38, 39] In addition, there is voltage difference between conversion and de-conversion reaction, which is resulting from differences in free energy between crystalline and amorphous materials as the formed Li_nX /M nanocomposites are of amorphous character.[40]

Upon 1st discharge below 1V for most conversion reaction compounds, higher capacity values than theoretically predicted are usually observed. Electrolyte decomposition for Solid-Electrolyte Interface (SEI) formation and interfacial storage are proposed to be responsible for the extra capacity during the 1st discharge as illustrated in Figure 1-5.[41, 42] SEI is several nanometers in thickness composing of a thin solid layer surrounded by a gel-like polymeric layer. The main components of

SEI are LiF, Li_2CO_3 and alkylcarbonates, which irreversibly consume lithium ions.[37] Stable SEI formation is essential as it contributes to structural integrity of active materials during cycling. Interfacial storage, namely, is the capacitive storage of lithium ions on the Li_nX side and electrons at the metallic side at the LinX/M interface.[43] And, the capacitive charge storage is reversible and present at all rates.[43]

1.2.4 Iron-based Electrode Materials

A series of transition metal oxides and sulfides have been considered as potential electrode materials for rechargeable lithium batteries.[35, 44, 45] Among these candidates, iron oxides (including FeO, Fe_2O_3 and Fe_3O_4), iron Oxyhydroxide (FeOOH) and Iron Sulfides (including FeS_2 and FeS) have drawn particular attention because of their non-toxicity, natural abundance and improved safety for large-scale applications.[46]

Conversion reaction in iron oxide electrodes was firstly observed in 1980s. Afterwards, Fe_2O_3 and Fe_3O_4 have drawn particular attention because of their high theoretical capacity of ≈1000 mA h g^{-1}. As a result, intensive research has been conducted in which the electrochemical lithium storage properties are evaluated for iron oxides synthesized into 0D, 1D, 2D and 3D nanostructures by various synthetic methods. Excellent capacity performance (> 900 $mAhg^{-1}$) sustained up to 50-100 cycles have been widely reported. FeO, with a theoretical capacity of 744 mA h g^{-1}, has also been synthesized into nanosize and the cycling performance needs improvement.[47]

Both FeS_2 and FeS are well-studied in the 1980's and early 1990's in lithium battery field with molten salt electrolytes.[48, 49] In room temperature with liquid electrolyte, FeS and FeS_2 has initial capacity of 500 and 600 mAh g^{-1}, respectively. But both of them have poor reversibility. The poor reversibility is due to the formation of lithium polysulfide intermediates during reaction, and the lithium polysulfides are partially soluble in organic electrolyte, reducing ionic conductivity of the electrolyte, which results in severe inefficiencies.[50, 51] However, FeS_2/Li couple is employed in primary AA cells and are still in commercial market used in reserve batteries.[52]

However, those iron-based conversion reaction electrode materials suffer from poor cyclability, which is caused by large volume change during prolonged cycling process. The low conductivity of these materials may result in performance deterioration at high current densities. Strategies, such as designing into nanostructures, introducing porosity and amorphization, are expected to maintain structural integrity and mitigate pulverization.

1.2.5 2-Dimensional Nanostructuring Electrode Materials

1.2.5.1 Nanostructuring electrode Materials

Nanostructuring greatly improves the Li storage properties of anode materials in LIBs. [53] First of all, Nanostructuring plays an important role in the functioning of conversion-reaction anode materials. First of all, reversibility of conversion reaction is nano-enabled. The key to the reversibility of the conversion reaction lies in the

formation of metal nanoparticles upon complete reduction of above-mentioned transition metal compounds, and the reduced nanoparticles are embedded in the matrix of the lithium binary compounds (Li_nX) with a large interfacial area, which is very active and easy to decompose and react with the embedding metal nanoparticles when a reverse electrical polarization is applied.[35, 54, 55] But, the Li_nX matrix is electrically insulating and results in slow kinetics. Nanostructuring of anode materials offers shorter path for ion and electron transport, and enables reversibility of the redox reaction and faster kinetics, which is important for its better reversibility and high-rate performance.[56] In addition, the conversion reaction takes place in accompany with major structural stress and volume change, which may result in particle decohesion and electrical insulation with current collectors. Nanostructuring can better accommodate the volume change and hence, helps improve the cycling performance. Finally but most importantly, nanostructuring of both anode and cathode materials provides larger effective interaction area between the electrode material and electrolyte.[44] In Summary, nanostructure-based anodes offer larger surface area contacting with electrolyte, shorter mass and charge transport distance and better accommodation for volume change during charge-discharge cycles, so that the energy density, power density and cycling stability of LIBs can be expected.[53, 57]

1.2.5.2 Electrode Materials with 2D Nanoarchitectures

The manner of lithium storage and the storage capability of electrode materials are greatly affected by their structural properties.[58, 59] And, different structures have

their unique performance based on surface and structural properties.[59] 2D nanostructures are suitable for energy storage applications due to their maximized exposed surface area and shortened paths for fast charge transport. Materials with higher surface area are especially favored in anode applications, because the large surface area gives rise to improved capacities owing to interfacial lithium storage, meaning that excess Li can be accommodated at the electrode-electrolyte interfaces.[59, 60]

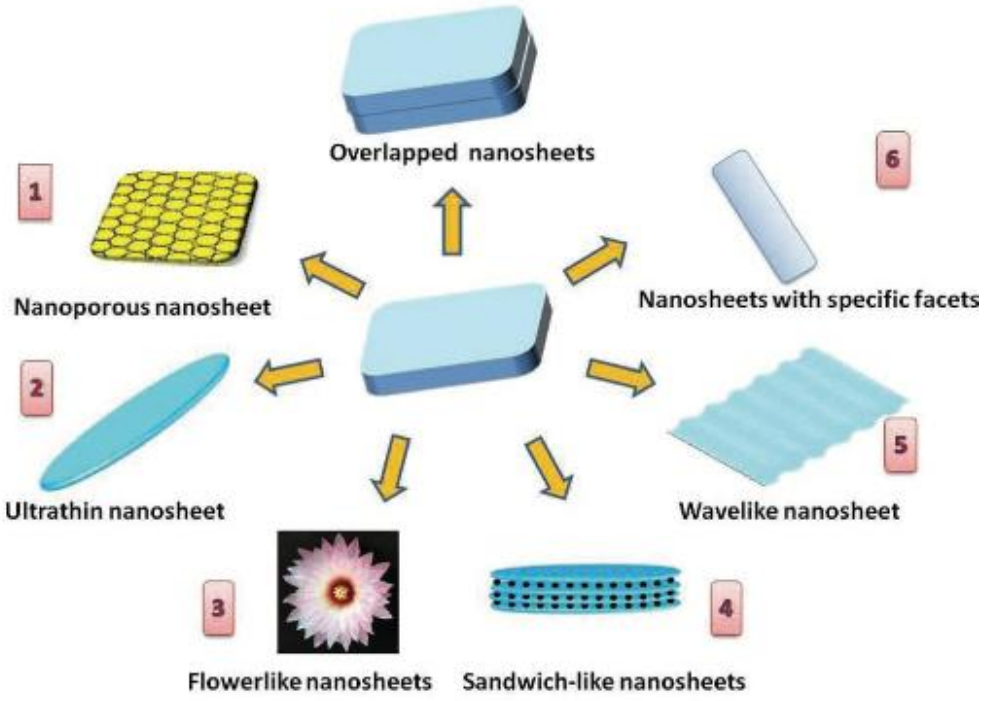

Figure 1-6: Novel 2D Nanoarchitectures suitable for energy storage and catalysis applications [59]

2D nanostructures can be divided into six categories as demonstrated in Figure 1-6. Ultrathin nanosheets are of special interest in lithium storage owing to their thicknesses of sub-5nm, [61, 62] which offers more effective sites and much faster

lithium storage kinetics. For example, graphene, which is one-atom thick, can have lithium stored on both sides of its planar sheets creating LiC_2 structure, and improve its specific capacity to 744 mAh g^{-1} from 372 mAh g^{-1} of graphite.[63] Nanosheets with nanoporous framework is also attractive for energy storage applications, because they provide large electrode-electrolyte interaction area and reduced charge diffusion length, thus the rate capability and power density are enhanced.[64] Therefore, combining these two characteristics of nanosheets, hierarchically nanoporous and ultrathin is of great interest for further improvement of electrode materials.

1.2.5.3 Synthesis of ultrathin nanosheets

It is challenging to choose the suitable synthetic process complying with the Ostwald ripening to obtain ultrathin nanosheets. [59] Ultrathin nanosheets of metal sulfides and metal oxides can be synthesized by chemical vapor deposition (CVD),[65-68] liquid or electrochemical exfoliation[69-74] and surfactant-assisted controlled growth.[66]

Chemical vapor deposition enables preparation of large-area ultrathin transition metal dichalcogenides (TMDs). One of the examples is a two-step thermolysis process for the deposition of three-layered (~2nm) MoS_2 nanosheets by dip-coating ammonium thiomolybdates $[(NH_4)_2MoS_4]$ followed by sulfurization in sulfur vapor.[66] The resulting ultrathin MoS_2 exhibited n-type behaviors with ON/OFF ratio of ~ 10^5 and electron mobility as high as 6 $cm^2\ V^{-1}s^{-1}$ in field-effect transistors (FET).[66]

Joensen and co-workers demonstrated ultrasound-promoted hydration of lithium-intercalated compound to prepare single-layer MoS_2.[71] A lithium intercalation

process takes place in solid MoS_2 with n-butyl lithium dissolved in hexane to form Li_xMoS_2. The lithiated product can be readily exfoliated to few-layer nanosheet by sonication in water. This method has a very high-yield (~100%) to prepare single-layer MoS_2 and also enables synthesis of the metallic 1T phase MoS_2, which is favored in energy storage and catalysis applications.[71, 75] Rui and coworkers reported the synthesis of 2.1-3.8 nm thick V_2O_5 nanosheets by liquid exfoliation in formamide. The ultrathin thickness allow high-rate lithium ion and electron transport, leading to remarkable energy and powder density of the V_2O_5 nanosheets as LIB cathode.[76]

2D ultrathin nanosheets of those metal sulfides and metal oxides with layered structures, which features that within each layer the neutral atoms are covalently or ionically bonded with their neighbors, whereas the adjacent layers are held by van der Waals connection along the third axis,[77] can be easily obtained by exfoliation. Direct growth of 2D ultrathin nanostructures of metal sulfides and metal oxides with non-layered crystal structure is relatively less reported. However, it still possible to obtain ultrathin nanosheets of non-layered metal sulfides and metal oxides via controlled colloidal synthesis in solution. [78, 79]

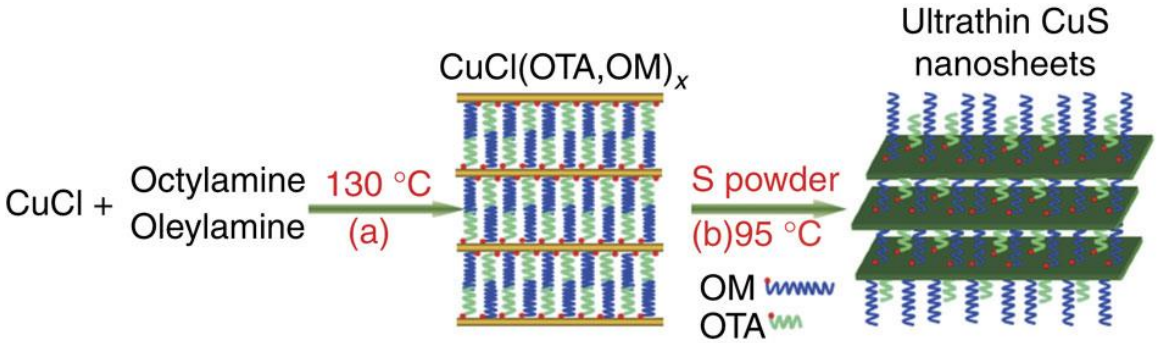

Figure 1-7: Scheme of the forming process of ultrathin CuS nanosheets [79]

Ultrathin Co_3O_4 nanosheets of 2-3nm thickness was synthesized with the assistance of hexamethylenetetramine (HMT) as structure directing agent (SDA) at low temperature, and the size can be controlled by regulating the HMT concentration. The synthesized structure possess a large surface area and is ideal for surface lithium storage.[78]

Zhang and coworkers report a soft-templating synthesis of ultrathin CuS nanosheets with a thickness of ~3.2nm and lateral length up to ~453 nm.[79] In the synthesis, The ($CuCl(OTA, OM)_x$) lamellar complex is formed as a reaction intermediate (as shown in Figure 4), and the lamellar structure acts as the soft template directing the planar growth of CuS after the addition of sulfur source. When tested as electrode material in LIBs, the ultrathin CuS nanosheets exhibit large capacity and good cycling stability. In addition, this method can be extended to the synthesis of ultrathin ZnS, Bi_2S_3 and Sb_2S_3 nanostructures. However, synthesis of hierarchical nanoporous ultrathin nanosheet is rarely studied.

1.2.6 Electrochemical Impedance Spectroscopy

Electrochemical Impedance Spectroscopy (EIS) is powerful in analyzing complex processes involving variables such as electrolyte, materials and interface geometry in the field of wet chemistry.[80]

Nyquist plots derived from EIS measurement are usually interpreted by using electrical equivalent circuit (EECs). In the past decades, EIS has been intensively employed in the analysis of lithium battery systems to determine process kinetic factors including conductivity and charge transfer properties.

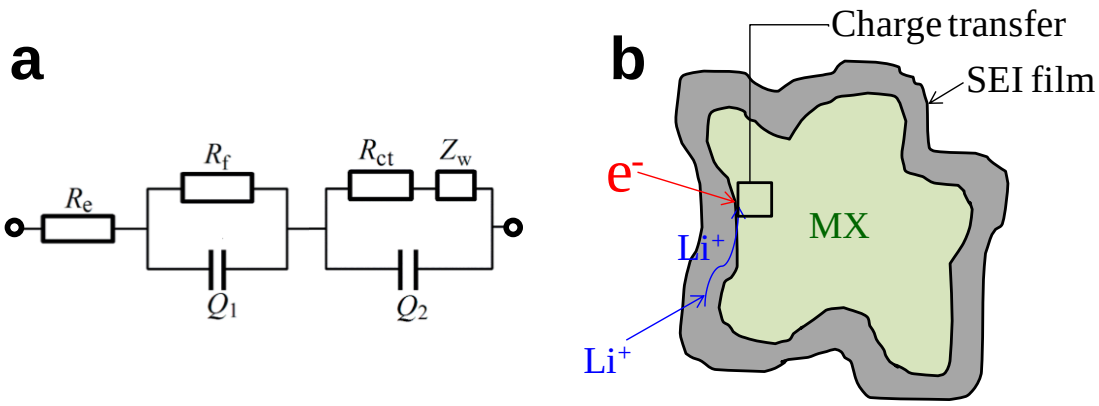

Figure 1-8: (a) equivalent circuit modeling conversion reaction electrode; (b) pictorial representation for charge transport in electrode materials based on conversion reaction

The most commonly used equivalent circuit model for conversion reaction and illustration of charge transport and charge transfer in conversion reaction are demonstrated in Figure 1-8a and Figure 1-8b, respectively.[81-83] In the equivalent circuit, R_e represents the overall internal resistance of the test cell, which is mainly electrical resistance of the electrolyte. In the conversion reaction, lithium ions need to

diffuse across the SEI layer from electrolyte to the active material interface, and electrons also transport from electronic conducting medium and cross the SEI layer to the active material to prepare for the conversion reaction. R_f is the resistance of SEI film and contacting resistance between active electrode materials. Q_1 indicates the double-layer capacitance of the electrode-electrolyte interface. After that, Charge transfer takes place at the interface and the conversion reaction proceeds. R_{ct} represents the charge transfer resistance at the interface, and Q_2 indicates the surface capacitance at the charge transfer interface. Z_w is the Warburg impedance corresponds to Li^+ diffusion process inside the active material.

2. Thesis Design

2.1 Research Gap and Hypothesis

2.1.1 Carbon coated hierarchical porous FeS nanosheets

With the increasing demand for higher-performance LIBs, exploration and synthesis of nanostructured electrode materials with controllable size, morphology and composition are attracting more research attention.[53, 58, 84] Nanostructured electrode materials are advantageous for LIBs for their better accommodation to structural strain, larger electrode/electrolyte interfacial area and shorter electronic/Li^+ transport length. Besides, the large surface area of nanomaterials leads to new lithium storage mechanism: interfacial lithium storage, in which excess Li^+ can be accommodated at the interfaces of the nanometer-sized particles resulting in an increase of total Li storage.[60]

Different nanostructures possess their unique surface and structural properties, and porosity introduced to various nanostructures can significantly enhance the effectiveness and durability of reversible lithium storage.[59] Hierarchical nanoporous anatase TiO_2 formed via a in-situ hydrolysis method has a high specific surface area, which is key to interfacial Li storage on the surface of TiO_2 nanoparticles, leading to its high lithium storage performance at high charge/discharge rates when used as anode in LIBs.[59] Porous Co_3O_4 nanosheets composed of nanoparticles obtained by a simple and scalable electrodeposition approach exhibit higher capacity, better rate performance and cyclic stability than Co_3O_4 nanowires and Co_3O_4 nanodisks.[85-88] The improved lithium storage properties of those hierarchical nanoporous structure can be attributed to (1) constitution of both small particles and pores, which can more

effectively buffer the volume change during Li insertion/extraction; (2) the porous structure can facilitate the electrolyte penetration and reduce the transport path for lithium ions; (3) the interconnected nanoparticles are beneficial to the electronic diffusion, and sustain the overall structural integrity during repeated Li insertion and extraction. Herein, hierarchical nanoporous nanosheets with larger surface area and more flexible distribution are ideal choice for lithium storage.

Iron sulfides, both FeS and FeS_2, have been widely used as electrode materials in lithium primary batteries and high-temperature batteries due to their cost effectiveness and abundance in nature.[89, 90] The Li storage process in the conversion-reaction metal sulfides generates polysulfides Li_2S_x ($2<x<8$),[91, 92] which can easily dissolve to the organic electrolyte and migrate to the cathode side. This results in its poor cyclability in rechargeable batteries. Previous studies on Li-S battery showed that fabricating S into thin wrapping layers could effectively reduce Li_2S_x dissolution into the electrolyte, which led to high reversible capacities and good rate capabilities.[93-95] Therefore, it is desirable to develop a simple process to wrap synthesized metal sulfide nanostructures with a thin layer of protective carbon to reduce polysulfides dissolution into the electrolyte, so that the cycling stability of metal sulfides electrode can be improved.

2.1.2 FeS/ZnS composite hierarchical nanosheets

Various metal sulfide nanostructures, such as SnS nanoflowers,[96] few-layer SnS_2 nanosheets,[97] FeS nanocrystals,[98] ZrS_2 nanodisks,[99] CoS nanoflowers,[100]

and nickel sulfide nanowires,[101] has been synthesized and demonstrated to possess improved lithium storage properties compared with their bulk counterparts. Metal sulfides having alloying reaction with lithium, such as SnS, SnS_2 and ZnS usually encounter large volume change during lithium insertion/extraction, which probably will lead to pulverization. Metal sulfides belonging to conversion reaction classification have voltage plateaus of higher than 1.0V vs. Li/Li+ during lithiation, which makes it inappropriate for anode materials for LIBs. Up to date, most researches on metal sulfide lithium storage concentrate on individual metal sulfides, which experience these two problems in lithium storage application.

Literature shows that some hybrid metal oxides nanostructures have advantageous lithium storage performance compared with individual metal oxides. Fan and coworkers demonstrate synthesis of Fe_3O_4 and MnO composites via co-precipitation technique, and the composite oxides demonstrate superior cycling performance compared with the individual Fe_3O_4 and MnO prepared under the same experimental conditions.[102] The co-existence of the heterogeneous metal oxides acts as dispersant to each other during repeated lithiation and de-lithiation.[102] Yan and coworkers shows enhanced lithium storage performance of SnO_2/Fe2O_3 hybrid nanostructure synthesized by hydrothermal method.[103] The Fe_2O_3 helps prevent the agglomeration of SnO_2 nanoparticles. Taking the advantages of these two components, the metal oxides hybrid exhibits high rate capability and excellent cycling performance.[103] Other examples, such as SnO_2/TiO_2 nanotube hybrids,[104] branched α-Fe_2O_3/SnO_2 nanoarchitectures,[105] NiO/ZnO hybrid nanofibres,[106] ZnO/CoO nanoflowers[107] and Fe_2O_3/CuO nanowires[108] all exhibit different

redox reaction voltage plateaus compared with the individual component. And, due to the synergistic effect and dispersing effect of two components to each other, those compositing nanostructures all demonstrate higher capacity and better cycling stability than the individual oxides.

Therefore, it is of great interest to synthesize and investigate lithium storage properties of hybrid metal sulfides nanostructures. Iron sulfide FeS has conversion reaction with Li, and it has a relatively redox reaction voltage for anode application. ZnS has both conversion and alloying reaction with Li expecting higher capacity, but alloying reaction usually cause large volume expansion. It is of great interest to synthesize uniform FeS/ZnS compositing nanostructures with controllable Fe/Zn ratios and investigate their lithium storage properties.

2.1.3 Amorphous FeOOH nanosheet and its lithium storage kinetics

With repeated lithium ion intake and removal, volume of active anode materials changes and induces structural stresses, which may lead to pulverization (particle cracking). The particle cracking creates new surfaces that consume lithium causing irreversibility in capacity. And, the pulverization may result in disconnections within the active materials and between the active materials and the current collectors, cutting off the charge transport path and thus causing device failure.

There are several approached to mitigate the volume change problem. Firstly, nanostructuring with decreased dimensional size can greatly enhance the tolerance to stress. And, this strategy has shown its great effectiveness in many examples;[34, 109,

110] Secondly, porous structure formation can also effectively absorb the structural stress caused by volume change[111]; Thirdly, compositing the active anode materials with coatings (e.g. carbon coating) or modifying binders can also buffer the internal stress induced.[112-115] But, compositing with buffering additives usually involved multiple complicated steps, and addition of low-capacity compositing component suppresses the total capacity; fourthly, limiting the lithiation level by narrowing the voltage window can avoid the happening of reactions causing large volume change.[116]

Besides of all the strategies listed above. Amorphization is another effective approach to enhance intrinsic stress tolerance capability of anode materials. It was demonstrated by Wang and coworkers that amorphous TiO_2 nanotubes possess higher capacities and better capacity retention than that of anatase-phased crystalline TiO_2 with identical morphology, and the amorphous nanotubes after cycling show little morphology change.[117] In addition, TiO_2 is an intercalation-type anode material showing flat voltage plateau during lithiation and de-lithiation, but the amorphous TiO_2 shows gradient sloping charge/discharge voltage profile, implying different lithium storage mechanism associated with the amorphous anode.[117] Yang and coworkers demonstrate the synthesis of amorphous hierarchical porous GeO_x with primary particle sizes of 3.7 nm, which exhibit stable capacity of 1250 $mAhg^{-1}$ for 600 cycles.[118] Coupling the amorphous GeO_x with $Li(NiCoMn)_{1/3}O_2$ cathode forming full-cell lithium ion battery also shows high performance.[118] Oh. S. M. and coworkers report that MoO_2 in amorphous form demonstrate excellent cycling stability and rate capability compared with its crystalline counterpart.[119] In the

lithiated amorphous MoO_2, both Mo metal and Li_2O are absent, indicating that the lithium storage process of amorphous MoO_2 does not follow the conversion reaction route.[119] The authors deduce that the amorphous MoO_2 stores lithium by inserting Li ions into structural defects from the sloping charge/discharge profile in a wide potential range. Besides, the structural defects provide an opened and effective lithium diffusion path contributing to a high lithium ion mobility.[119]

Amorphous material varies from its crystalline counterpart in its irregular atomic arrangements, loose structure and large quantity of structural defects. Its "irregularity" leads to difficulties in formation of amorphous material with well-defined nanostructures. Novel synthesis technique is desired in the synthesis of amorphous nanostructures. Furthermore, there is a demand for a more comprehensive explanation of lithium storage mechanism and kinetics of amorphous materials.

2.2 Scope

Based on the detailed literature review and hypothesis raised up, we set out the following research objectives and work scope.

Iron sulfide, which is of low-cost and wide availability, was selected to study its lithium storage properties as anode in lithium ion battery. As reviewed above, some nanostructures are advantageous over others in lithium storage. In order to investigate the morphological effect of FeS nanostructures on its electrochemical lithium storage properties, in chapter three different FeS nanostructures (hierarchical nanosheets, hierarchical nanoparticles and hexagonal-shaped nanoplates) have been synthesized with controlled reaction parameters in organic solution based synthesis. Besides, formation mechanism of varying FeS nanostructures was studied. In addition, detailed lithium storage properties, such as capacity, rate capability and cycling stability of three FeS Nanoarchitectures, are characterized and compared.

As demonstrated in chapter three, pure FeS has a relatively high redox reaction potential with Li storage, which will limit the output voltage and energy/powder densities of full cells when employed as anode in lithium ion batteries. The lithiation of ZnS involves both conversion reaction and alloying Zn with Li, the dual Li storage mechanism contribute to higher Li storage capacities and the alloying reaction brings down the voltage plateau of lithiation. Besides, the coexistence of the heterogeneous sulfides could behave as dispersants of each other. In the work demonstrated in chapter four, combining these factors with the merits of FeS and ZnS, hierarchical FeS/ZnS composite nanosheets with different compositional ratios (Fe/Zn ratios) are synthesized, followed by detailed phase, morphology and compositional

characterization. In addition, lithium storage of hierarchical FeS/ZnS composite nanosheets with different compositional concentrations is characterized and compared.

Besides of nanostructuring, amorphization is another effective approach to enhance the tolerance to stress induced by the volume change during conversion reactions. And, disordered and defected structure can facilitate Li ion transport. In order to investigate the combined effect of amorphization and nanostructuring on conversion-reaction type anodes' lithium storage properties, In the work demonstrated in chapter five, amorphous Iron Oxyhydroxide nanosheets are synthesized from self-synthesized hierarchical FeS nanosheets. The lithium storage properties of the amorphous FeOOH nanosheets were investigated as anode in LIBs. Besides, lithium storage mechanism and kinetics of the amorphous FeOOH nanosheets were studied through EIS analysis with newly-proposed equivalent circuit model.

3. Synthesis of FeS Nanostructures and Their Lithium Storage Properties

3.1 Overview

Inspired by exciting findings of new dimension-dependent properties of graphene, ultrathin two-dimensional (2D) graphene-like nanosheets of metal sulfides are attracting greater research interest.[120-125] For energy storage applications, such as electrode materials in LIBs, 2D nanostructures of metal sulfides are desired to (1) enhance effective interaction between electrode materials and electrolyte; (2) provide shorter charge transport path.

2D nanostructures of some layered-structured metal sulfides, such as ZrS_2,[126] MoS_2,[127, 128] and WS_2,[129] have been actively studied as electrode materials in LIBs due to their structural advantages in reversible Li storage process. Nanosheets of layered-structured metal sulfides can be easily obtained by mechanical or electrochemical exfoliation. Direct growth of nanosheets of metal sulfides with non-layered crystal structures is relatively less reported although some of them possess high energy/charge storage capacities. Some pioneer works (e.g. growth of single crystalline PbS nanosheets through 2D oriented attachments,[130] polycrystalline CdTe nanosheets formed through dipole-dipole interactions[131] and SnSe nanosheets with tuned thickness[132]) indicates the possibility of obtaining nanosheets of non-layered metal sulfides *via* controlled growth with effective templating.

Iron sulfides are commonly employed electrode materials in lithium primary batteries [89] and secondary batteries[90] due to their low-cost and abundance in nature. Iron sulfides store Li *via* conversion reaction. However, the Li storage process in the

conversion-reaction based metal sulfides generates polysulfides Li_2S_x ($2<x<8$),[91, 92] which can be easily dissolved into organic electrolyte, reducing the ionic conductivity of the electrolyte. This results in poor cyclability of LIBs. What's worse is that the polysulfides may migrate to and shuttle the reaction on the other electrode side, causing battery failure. Recently, studies in Li-S battery showed that fabricating sulfur with uniform coating layers (e.g. carbon coating) could effectively reduce polysulfides dissolution into liquid electrolyte, leading to improved reversibility and rate capability.[93-95] This could be a promising strategy for performance improvement of metal sulfide electrodes, where the sulfides could be wrapped with a thin layer of carbon to reduce polysulfides dissolution into the electrolyte.

In this work, we report a facile approach to prepare FeS nanosheets *via* a surfactant-assisted solution-based synthesis. The formed nanosheets are hierarchically constructed by FeS nanocrystal building blocks. In the synthesis, 1-dodecanethiol is used as both the sulfur source and the surfactant. By varying the concentration of 1-dodecanethiol, hierarchical FeS spheres and hexagonally-shaped FeS nanoplates can be obtained. In addition, the hydrocarbon part of the surfactant can be converted to amorphous carbon after annealing under Argon atmosphere. The carbon coated hierarchical FeS nanosheets display high capacities, high rate capabilities and stable cycling performance.

3.2 Experimental Details

3.2.1 Synthesis of carbon-coated FeS nanostructures for Lithium ion batteries

The solution-based synthesis was carried out in a 100 ml three-neck flask. In a typical synthesis, 0.2 mmol (70 mg) $Fe(acac)_3$ (Aldrich) was first dissolved to 10 ml Oleylamine (OLA)(Aldrich, 70%) under magnetic stirring, and then Argon gas was introduced to purge the solution. After about 30 minutes of purging, the solution was gradually heated up to 120^oC to have $Fe(acac)_3$ completely dissolved forming a red-wine transparent solution. 1 ml 1-dodecanethiol (Aldrich, 98%) was then injected into the solution at 120^oC, and the solution turned transparent light-yellow upon injection. The solution was then stirred at 120^oC for 30 minutes before the temperature was further increased to 220^oC, and the solution turned opaque black. The reaction mixture was maintained at 220^oC for 20 minutes before naturally cooled down to room temperature. The resultant solution was dripped into hexane and the precipitates were collected by centrifugation at 6000 rpm for 10 minutes. The final product was dried in a vacuum oven. For comparison, FeS nanocrystals without carbon coatings was also prepared by mixing 0.05 M Na_2S and 0.05 M $FeCl_2$ in DI water under vigorous stirring for 1 hr protected with Argon atmosphere.

3.2.2 Materials Characterization

Crystallographic information for the samples was collected using a powder X-ray Diffractometer (Shimadzu 6000) with Cu K_α source (λ = 0.15418 nm). Dried powder was directly used for XRD measurement, and the measurements were conducted with

a scan rate of 1^{o}/min. The determination of the phases was done using the Match! software. The sample morphology was examined under a field-emission scanning electron microscopy (FESEM; JEOL, JSM-7600F). The dried powder was re-dispersed in hexane, and drop casted on silicon wafer for SEM characterization. For TEM characterization, the solution was diluted and ultrasonicated for 2hrs before it was drop casted onto 200 mesh carbon coated copper grids. HRTEM was obtained by using a JEOL 2010 system operating at 200 kV. The oxidation states and surface composition of the product were characterized by X-ray photoelectron spectroscopy (XPS) equipped with an Omicron ESCA Probe with a monochromatic Al Kα source at 1486.6 eV. The positions of the XPS peaks were corrected using the C 1s core level taken at 285.0 eV as the binding energy (BE) reference. Raman spectra were obtained with a WITec CRM200 confocal Raman microscopy system with a laser wavelength of 488 nm and a spot size of 0.5 mm. To calibrate the wavenumber, the Si peak at 520 cm^{-1} was used as a reference. Nitrogen adsorption/desorption isotherms were measured on a Micromeritics Tristar 3000 porosimeter (mesoporous characterization) and Micromeritics ASAP 2020 (microporous characterization) at 77 K. Samples were degassed at 100 °C for 6 h under vacuum before measurement. The specific surface areas were calculated using Brunauer–Emmet–Teller (BET) method. The sample preparation for the low-angle XRD is as follows: The reaction mixture was heated to 120^{o}C for 15 minutes. Then, 1ml aliquot of the mixture was extracted and cooled to room temperature, which was dropped on a glass slide for the low-angle XRD measurement. CHNS elemental analysis was conducted on a CHNS elemental analyzer, which can simultaneously determine the amount of Carbon, Hydrogen,

Nitrogen and Sulfur contained in materials. And, CHNS stands for Carbon, Hydrogen, Nitrogen and Sulfur. Sample preparation for CHNS elemental analysis: Equal amount (3mg) of carbon black was soaked in the electrolyte from the dissembled coin cells, which were cycled for 50 cycles. The soaked carbon black was dried before CHNS elemental analysis.

3.2.3 Electrochemical Measurement

The as-synthesized samples were annealed in a tube furnace at 400 °C for 2 h under argon atmosphere. Then, 80 wt% active materials, 10 wt% super-P carbon black and 10 wt% polyvinylidene fluorides (PVDF) were mixed into *N*-methyl-2-pyrrolidinone (NMP). The obtained slurry was cast onto a copper foil and dried in vacuum at 50 °C for 12 h to remove excess solvent. Electrochemical measurements were carried out on coin-type cells with lithium foil as the counter/reference electrode, Celgard 2400 membrane as the separator, and the electrolyte solution obtained by dissolving 1 M $LiPF_6$ into a mixture of ethylene carbonate (EC) and dimethyl carbonate (DMC) (EC/DMC, 50: 50 w/w). The cells were tested on a NEWARE multichannel battery test system with galvanostatic charge and discharge (voltage window of 0.01–3.0 V). Cyclic voltammetry (0.01–3 V, scan rate of 0.5 mV s^{-1}) was carried out with an electrochemical workstation (Solartron). It should be noted that the specific capacity was calculated on the basis of the total mass of the carbon and FeS composites.

3.3 Results and Discussion

3.3.1 Phase and Morphology characterization

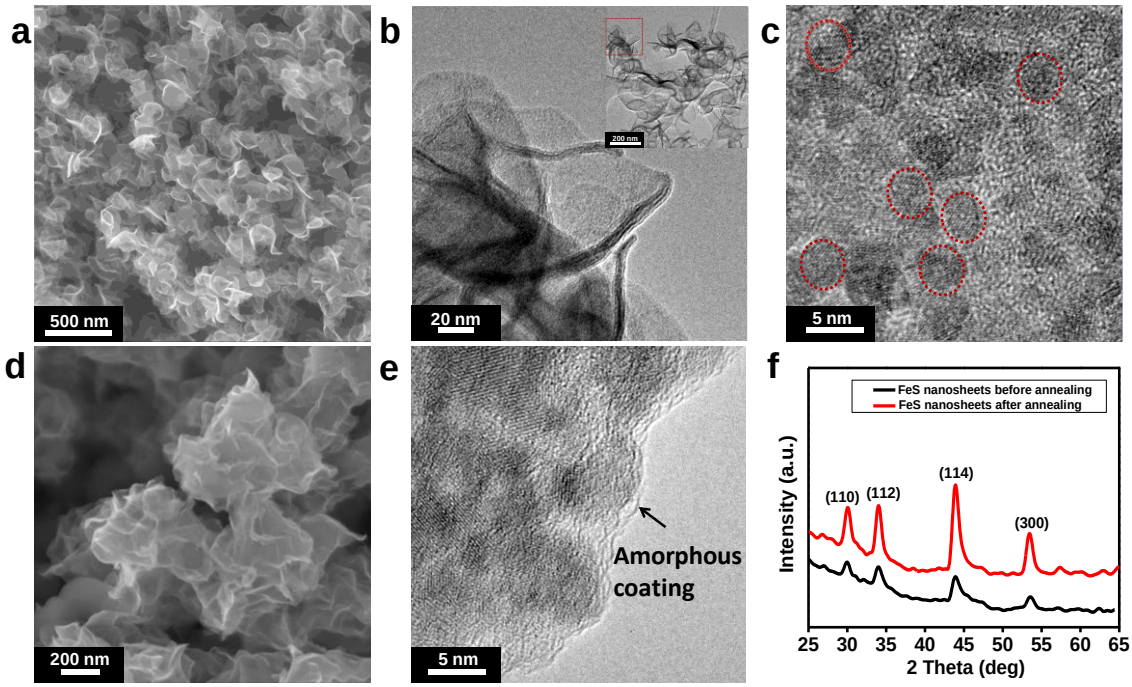

Figure 3-1: (a) SEM image and (b) TEM images of as-synthesized nanosheets; (c) HRTEM top-view image of the polycrystalline nanosheet; (d) SEM image showing nanosheet retention after annealing; (e) higher-magnification TEM image of the polycrystalline nanosheet edge after annealing; (f) XRD pattern of as-synthesized(black) and annealed(red) sample.

The SEM image (Figure 3-1a) and TEM image (Figure 3-1b) of as-synthesized product show formation of wave-like nanosheets, which have lateral lengths of 100-200 nm and average thickness of sub-10nm. The ultrathin and flexible nanosheets are interconnected forming a loose framework. A planar-view HRTEM image (Figure 3-1c) reveals the polycrystalline nature of each individual nanosheet, which is

constructed by nanocrystals smaller than 5 nm as highlighted by the red circles. In addition, the nanosheet morphology shows no obvious change (Figure 3-1d) and the nanocrystals on the nanosheets remain dispersed without significant coarsening after annealing the as-synthesized product at 400^{o}C under Ar atmosphere. During annealing, the capping organic component is expected to transform to amorphous carbon, as indicated by the HRTEM image of nanosheet edge after annealing (Figure 3-1e). The amorphous carbon does not only protect the thin nanosheets from stacking together but also prevents dispersed nanocrystals from agglomerating.

The XRD pattern (Figure 3-1f) shows that the as-synthesized product is pure Troilite phase FeS (JCPDF #037-0477) without other phases. The reflection peaks at 2θ = 29.95^{o}, 33.71^{o}, 43.18^{o} and 53.17^{o} correspond to the (110), (112), (114) and (300) planes of Troilite FeS, respectively. Besides, there is no predominant peak in the XRD pattern, indicating that there is no preferred crystalline orientation in the nanosheets. The phase and crystalline orientation were not changed after annealing. The diffraction peaks get more predominant due to the improved crystallinity after annealing.

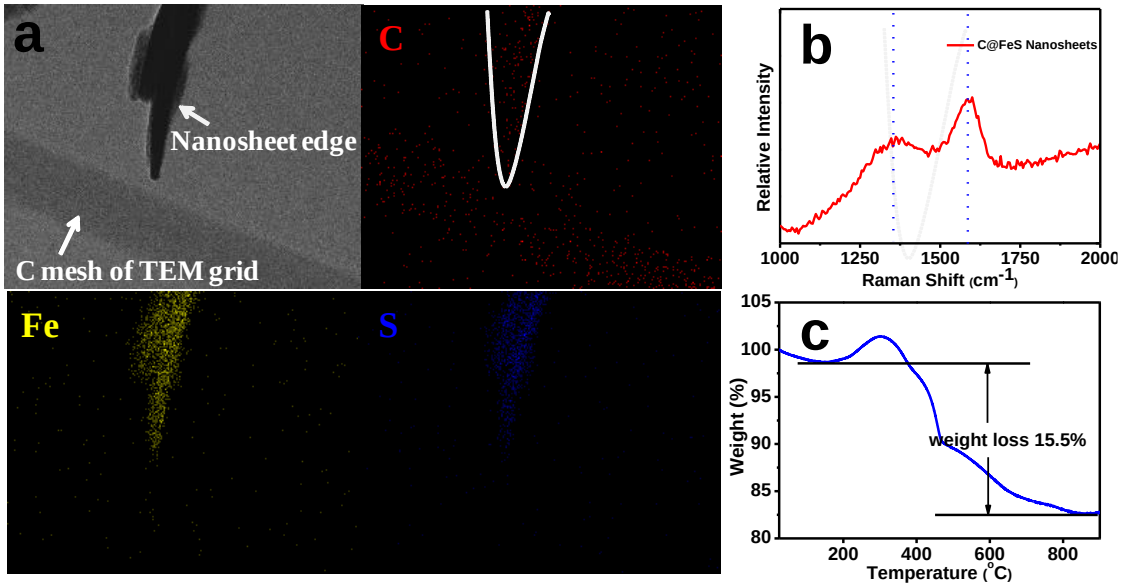

Figure 3-2: (a) STEM-EDX elemental mapping revealing the presence of C, Fe and S in the annealed FeS nanosheets; (b) Raman spectrum confirms the presence of carbon, and reveals the amorphous character of the carbon; (c) TGA profile of carbon coated nanosheets heated in air from room temperature up to 900ºC.

The elemental mapping (Figure 3-2a) clearly indicates that there is a uniform dispersion of the carbon element all over the FeS nanosheet. The carbon component was further studied using Raman Spectroscopy (Figure 3-2b). The Raman signatures of G band (~1580 cm^{-1}) and a D_1 band (~1340 cm^{-1}) confirm the existence of carbon, which is poorly crystallized. And, the features of G and D band are similar as carbon formed by carbonization of organic surfactants.[133, 134] At this stage, it can be concluded that carbon coated hierarchical FeS nanosheets are formed. Thermal gravimetric analysis (TGA) profile (Figure 3-2c) of the carbon coated FeS nanosheets

shows 15.5% weight loss by heating in air up to 900°C, implying that 7% of the mass is carbon.

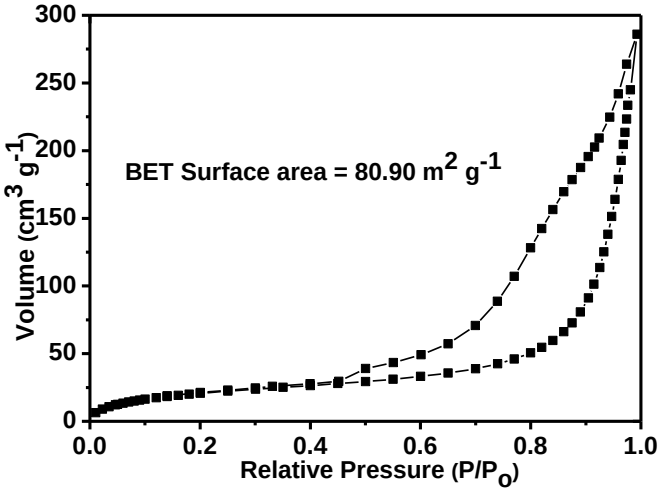

Figure 3-3: Nitrogen adsorption/desorption isotherm of the annealed hierarchical FeS nanosheet.

The specific surface area of the annealed C@FeS nanosheets is calculated to be 80.9 m^2 g^{-1} based on the Brunauer-Emmett-Teller (BET) analysis of the nitrogen absorption/desorption isotherm (Figure 3-3). The adsorption/desorption isotherm shows a type IV hysteresis and closure at p/p_o~0.4 indicates the presence of small mesopores. The mesoporous structure is favored in lithium storage as it has a high surface area and nanoscale porosity, thereby the electrolyte/electrode interaction area is maximized.

3.3.2 Reaction Mechanism

The polycrystalline nature of the as-prepared FeS nanosheets suggests that the ultrathin 2D shape is not directly related to the crystal structure of FeS, and the formation mechanism is different from that of single-crystalline ZrS_2, MoS_2, WS_2 and Fe_7S_8 2D structures.[126, 135-137] To investigate the growth details of the samples, control experiments were carried out under varying experimental conditions.

3.3.2.1 Effect of sulfur source

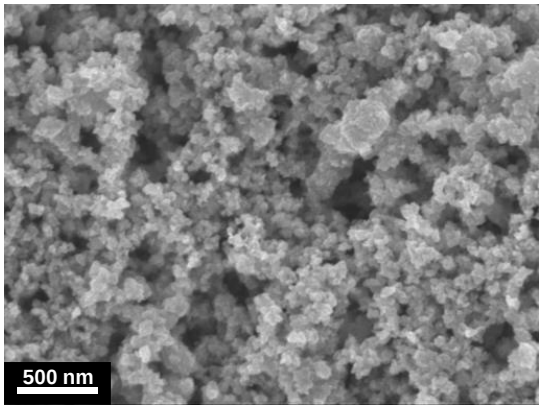

Figure 3-4: SEM image of the irregularly-shaped nanocrystals formed by using Oleylamine-S instead of 1-Dodecanethiol as the sulfur source in the solvothermal synthesis.

In a typical synthesis, 1-dodecanethiol (DDT) containing –SH functional group is considered as the only sulfur source. Replacing Dodecanethiol with S-OLA (prepared by dissolving sulfur powder in Oleylamine) while keeping other synthesis parameters identical resulted in the growth of irregularly-shaped nanocrystals (Figure 3-4). This

indicates that DDT does not only act as the sulfur source, but also influences the nanostructure morphology.

3.3.2.2 Effect of varying precursor ratios

In a typical FeS nanosheet synthesis reaction, the molar ratio between iron source and sulfur source ($I_{Fe:thiol}$) is 1:20.

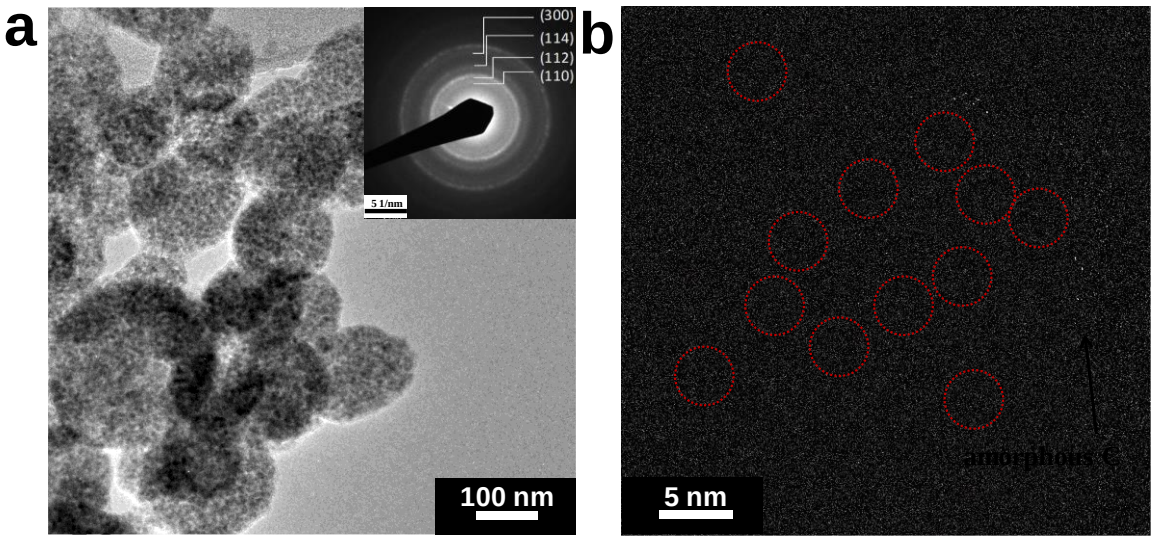

Figure 3-5: (a) TEM image of FeS hierarchical particles and corresponding SAED pattern (inset); (b) HRTEM image of the FeS hierarchical nanoparticles embedded in amorphous carbon matrix.

By decreasing the amount of DDT, the molar ratio of $I_{Fe:thiol}$ is increased. Increasing the molar ratio of $I_{Fe:thiol}$ to 1:4 leads to formation of spherical particles as shown in Figure 3-5a. Diameters of the spherical particles range from 30 to 100 nm. The HRTEM reveals that each particle is a cluster composed of nanograins of 2~3-nm in

diameter embedded in an amorphous carbon matrix. The SAED pattern (Figure 3-5a inset) confirms that the nanograins are Troilite-Phase FeS (JCPDF #037-0477).

Thereby, carbon coated hierarchical FeS spheres is formed with $I_{Fe:thiol}$ increase to 1:4. Nevertheless, further decreasing of $I_{Fe:thiol}$ molar ratio to values higher than 1:4 does not affect the hierarchical sphere morphology, but the throughput is lower with lower amount of DDT added.

3.3.2.3 Effect of reaction temperature

Apart from types of sulfur source and precursor concentration, reaction temperature also plays an important role in the morphology of forming nanostructures. Increasing the reaction temperature from 220^{o}C to 280 ^{o}C while keeping $I_{Fe:thiol}$ = 1:20 unchanged leads to evolution to a different morphology (Figure 3-6).

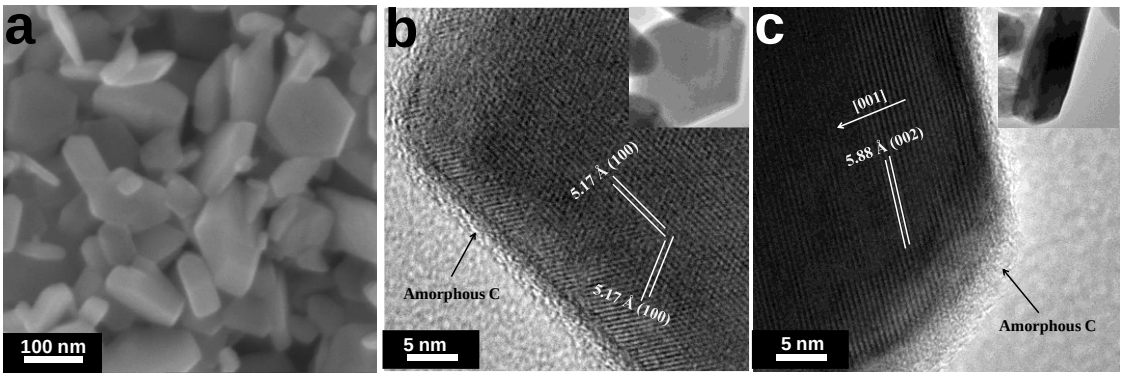

Figure 3-6: (a) SEM image of the hexagonal nanoplate obtained with increased reaction temperature; (b) and (c) HRTEM images of the nanoplate with planar-view and side-view, respectively. Insets in (b) and (c) are the corresponding low magnification TEM images where the HRTEM images were obtained.

With increased reaction temperature, flexible, thin and polycrystalline nanosheets reconstruct to more well-defined hexagonal-shaped thickened nanoplates. The

nanoplates have lateral lengths of 100-200 nm and thickness of around 50 nm. The HRTEM images of both planar view and side view of the after-annealing nanoplate (Figure 3-6b and 3-6c) show morphology retention and amorphous carbon coating around the plate surface. Besides, the nanoplates are single-crystalline. The lattice spacing of 5.17 Å and 5.88 Å correspond to the (100) and (002) planes of Troilite FeS (JCPDF #037-0477), and the normal of the planar plane is along the [001] direction. It is deduced that the sub-5nm building blocks of hierarchical nanosheet aggregate and recrystallize to thickened and more well-crystalline nanoplates at higher temperatures. And, the kinetic effect brought about by increasing temperature gradually exceeds the directing effect of surfactant when the reaction temperature increases from 220^{o}C.

3.3.2.4 Proposed reaction mechanism

The hierarchical FeS nanosheets obtained in this work is polycrystalline and those FeS nanocrystals exhibit no preferred orientation and facet exposure. Oriented attachments usually leads to single crystalline nanosheet with preferred orientation.[130] Thus, oriented attachment may be less involved here. Another possibility is that the growth of the nanosheets are directed by the electrostatic interaction between the nanocrystals as previously reported for CdTe nanosheets.[131]

Based on the discussion above, factors, such as types of precursors, precursor concentrations and reaction temperature, all affect the nanosheet formation. The absence of DDT leads to formation of irregular nanocrystals, and varying the amount of DDT leads to formation of hierarchical spheres. Therefore, it is deduced that DDT, in the formation of FeS nanosheets, does not only act as the sulfur source, but also as a

surfactant templating the growth of varying nanostructures. A soft-templating formation mechanism of varying FeS nanostructures (hierarchical sheet, hierarchical spheres and nanoplates) are proposed and illustrated in Figure 3-7.

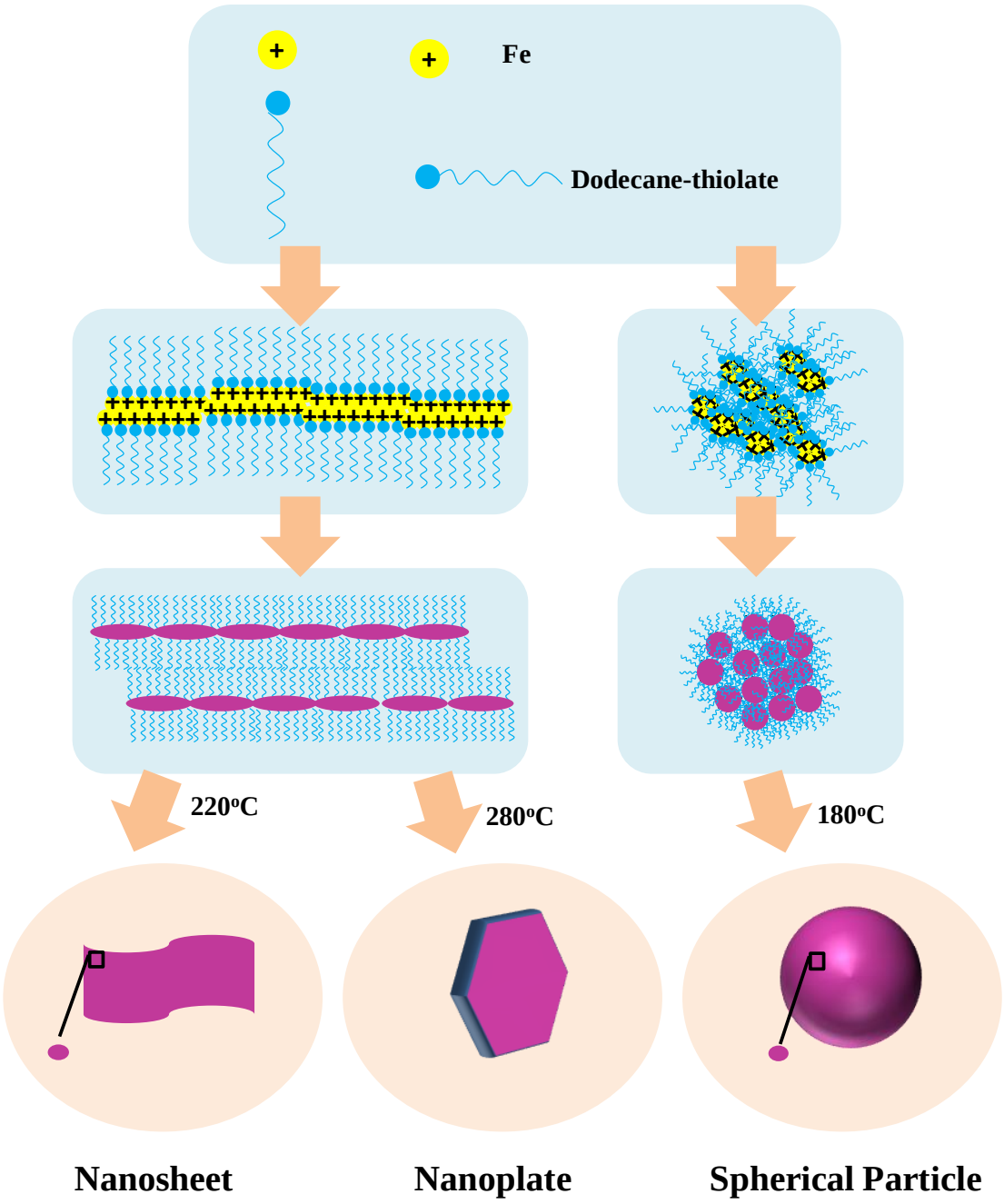

Figure 3-7: Proposed reaction mechanism for the carbon coated hierarchical FeS spherical particles, nanosheets and hexagonal-shaped nanoplates.

According to the scheme of the proposed reaction mechanism, the acidic DDT reacts with the basic OLA to form $OLAH^+$ and dodecane-thiolate anion,[138, 139] the latter of which binds strongly to Fe leading to a dipole unit containing Fe-S^- head and alkyl chain tail. The charged dipoles induce the dipole-dipole interaction between nanocrystals and direct the nanosheet formation. Above all, the shape of micelles directed by DDT under different synthesis conditions is considered to be the key influential factor to the final morphology. With a lower concentration of DDT ($I_{Fe:thiol}$=1:4), polycrystalline spherical particles are formed, while with a higher concentration of DDT ($I_{Fe:thiol}$ = 1:20), polycrystalline nanosheets are formed. Nevertheless, both the spherical particles and nanosheets are composed of nanocrystal building blocks with sizes of 2-3nm. If the dipole-dipole interaction is the determining factor in the FeS nanosheets formation, [140] we would expect to observe some FeS nanosheets at $I_{Fe:thiol}$ = 1:4 rather than the polycrystalline nanoparticles. Therefore, shape of the micelles could be an important driving force for morphology variation. As illustrated in Figure 3-7, we proposed that the Fe/DDT complexes with lamellar structure act as the soft template for the nucleation and growth of polycrystalline FeS nanosheets, while the spherical micelles lead to the formation of polycrystalline FeS spherical particles. During the annealing process, the $-C_{12}$ tails may evolve to the amorphous carbon layer and in the meanwhile prevent the agglomeration of FeS nanocrystals across the lamellas (in hierarchical nanosheets formation) or inside the spherical particles (in hierarchical particle formation). However, at a higher temperature of 280^oC, the rapid diffusion process of the atoms may take place across

the interfaces (*i.e.* the amorphous layers and grain boundaries), which allows agglomeration and recrystallization of nanograins leading to well-crystalline hexagonal FeS nanoplates. The hexagonal shape of the single-crystalline FeS nanoplates may be directly related to the hexagonal atomic arrangement of Troilite-phase FeS. Hexagonal-symmetry crystal lattice usually lead to the growth of plate-like shape mainly due to the confined growth within the (001) plane.[141, 142] The above observation also implies that the soft-templating effect of the Fe/DDT complexes is gradually overwhelmed by the rapid atomic diffusion at temperatures higher than 220ºC.

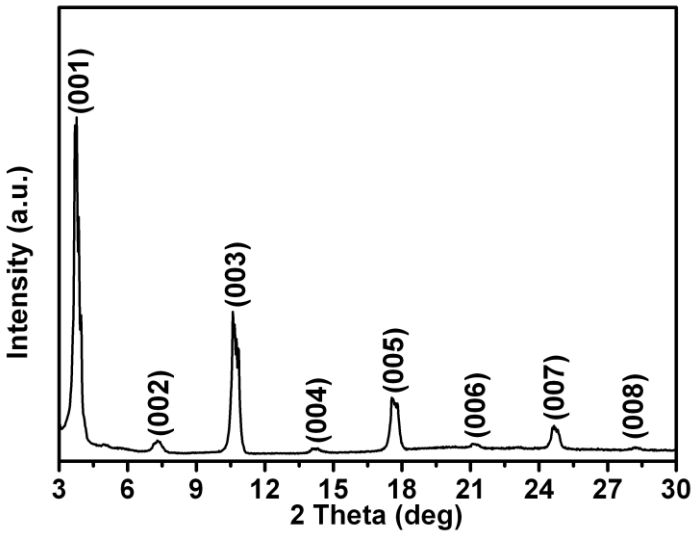

Figure 3-8: Low-angle XRD pattern of the viscous precursor solution containing $Fe(acac)_3$ and 1-dodecanethiol with IFe:thiol = 1:20 in 10 mL Oleylamine

To examine the discussion above, low-angle XRD pattern of the colloidal suspension was conducted for the solution reacting from $I_{Fe:thiol}$ = 1:20 in OLA (Figure SI13, supporting information). The XRD pattern shows a group of periodic reflection peaks at 2θ=3.77º, 7.3º, 10.6º, 14.2º, 17.7º, 21.22º, 24.68º with gradually decreased

intensities suggesting the formation of the lamellar structure. The 1st-order reflection of the strong peak at $2\theta=3.77^{o}$ corresponds to a d-spacing of 2.34 nm, and is larger than the 1-dodecanethiol molecular length (1.52nm),[143] which implies a double layer of the hydrocarbon tails in between the Fe-S layers. The low intensities for the (002), (004), (006) and (008) peaks also prove the bi-layer feature of the surfactants.[144] It should be noted that the small angle XRD measurement was performed at room temperature while the synthesis of the FeS nanostructures was carried out at temperatures > 200 °C. The shape of the micelles could be affected by the temperature.[145] However, the above observation partially supports that there are lamellar soft templates formed in the precursor solution. DDT has been previously used only as sulfur sources for the synthesis of metal sulfides, *e.g.* CdS nanowires, flower-like Cu_2S, ZnS and MnS nanocrystals,[146-152] but has not been demonstrated as a major controlling factor to morphologies of metal sulfides nanocrystals. More importantly, the alkyl chains capping on the FeS nanocrystals can be converted to carbon layers, which does not only prevent agglomeration of nanograins during reaction but also is important to achieve desired lithium storage performances of sulfides by reducing polysulfide dissolution into the electrolyte.

3.3.3 Electrochemical Characterization

Comparative electrochemical characterization was conducted to investigate the lithium storage performances of the hierarchical FeS nanosheets, hierarchical FeS

nanosheets and FeS nanoplates based on two-electrode coin-type cells with Li metal as the counter electrode.[153]

3.3.3.1 Cyclic Voltammetry and voltage profile

The cyclic voltammetry curve of the representative carbon coated FeS nanosheets based electrode is shown in Figure 3-9a. A small anodic peak at 1.65V is observed during the 1st cycle discharge but missing in the subsequent cycles. This peak is associated with lithium intercalation into the pseudo-layered structure of FeS. The capacity contributed by this reaction is low. With extensive intercalation of lithium, the structure will break down and conversion reaction starts to take over.[154] A sharp anodic peak at around 1.05V is related to the conversion reaction between FeS and Li with the formation of Li_2S and nano-Fe:[90, 92, 154, 155]

$$FeS + 2Li + 2e^- = Li_2S + Fe$$

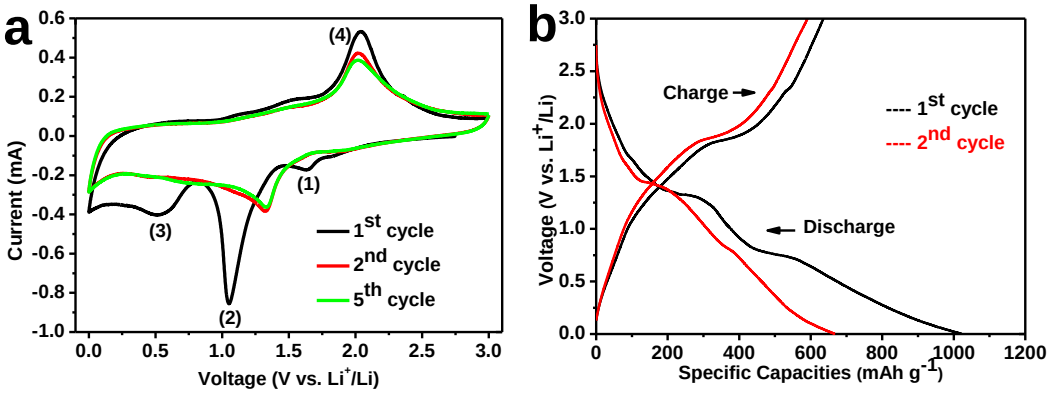

Figure 3-9: (a) Cyclic Voltammetry of the FeS nanosheets electrode between 0.01 V and 3 V at a scan rate of 0.5 mV s^{-1} for the 1st, 2nd and 5th cycle; (b) charge-discharge voltage profiles of the FeS nanosheets electrode at a current density of 0.1 A g^{-1} in the first two cycles.

This peak denotes the main reaction, and it is repeated at a more positive potential at 1.3V in the subsequent 2nd and 5th discharge.[90, 137] The formed elemental Fe is in the form of nanoparticles embedded in the amorphous matrix of Li_2S. The broad peak appearing from 0.75V to 0V, which is missing in the subsequent discharges, is attributed to the formation of solid electrolyte interlayer (SEI formation).[155] The large interfacial area between the Fe nanoparticles and Li_2S matrix enables reversed conversion reaction. The cathodic peak at around 2.0V in the 1st, 2nd and 5th cycles corresponds to the oxidation of nano-Fe by surrounding Li_2S to the reformation of FeS releasing lithium:[135, 137]

$$Fe + Li_2S \rightarrow FeS + 2Li + 2e^-$$

Nanostructuring of FeS makes the conversion reaction reversible, which enables the application of iron sulfide in rechargeable LIBs.

Charge/discharge voltage profiles of C@FeS nanosheets electrode at a current density of 0.1 A g^{-1} (0.16C) between 0.01V and 3.0 V are shown in Figure 3-9b. C@FeS nanosheets electrode delivers an initial discharge capacity of 1022 mAh g^{-1} and a subsequent charge capacity of 635 mAh g^{-1}, leading to a 1st-cycle Columbic efficiency of 62%. The large discharge capacity of C@FeS nanosheets electrode during the 1st cycle is attributed to the formation of SEI. As nanostructures usually provide a large electrode/electrolyte interaction area, the SEI formation consumes more lithium, leading to higher capacity irreversibility, especially during the initial cycles. During the 2nd cycle, the C@FeS nanosheets electrode delivers a discharge capacity of 668 mA g^{-1} and a charge capacity of 591 mAh g^{-1} with a much higher Columbic efficiency of 88.4%.

3.3.3.2 Rate capability

Sustention of high capacity at high rates is crucial to achieving high power densities in LIBs. The specific discharge capacities of different FeS nanostructure based electrodes at varying discharge rates are plotted in Figure 3-10a.

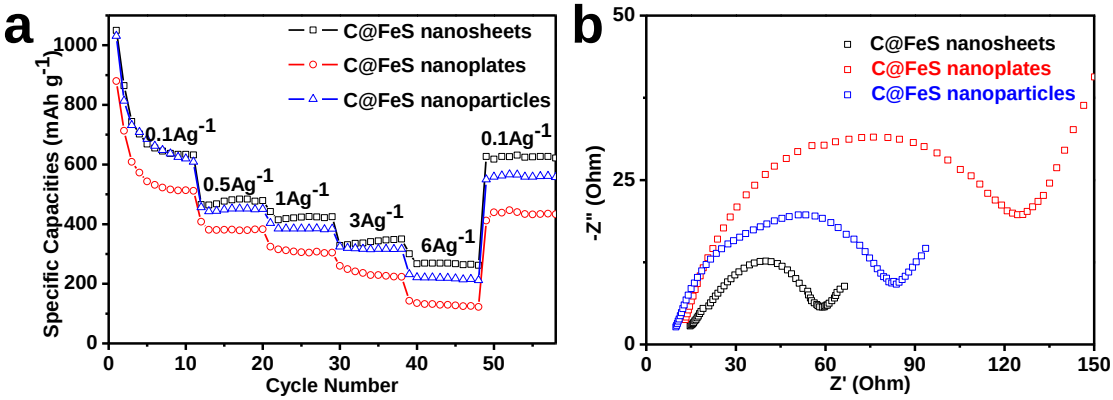

Figure 3-10: (a) Cycling performance of the carbon coatedFeS nanostructure based electrodes at various charge-discharge rates; (b) Nyquist plots of FeS hierarchical nanosheets-, nanoplates- and hierarchical particle-based electrodes after 5 galvanic discharge/charge cycles.

The hierarchical nanosheet electrode depicts 9th-cycle discharge capacities of around 630, 486, 425 and 349 mAh g^{-1} at current densities of 0.1 A g^{-1} (0.16C), 0.5 A g^{-1} (0.8C), 1 A g^{-1} (1.6C) and 3 A g^{-1} (5C), respectively. Even at a very high current density of 6 A g^{-1} (10C), the nanosheets can still deliver a 9th-cycle discharge capacity of 266 mAh g^{-1}, which is higher than those reported for some of the state-of-art anodes at 10C, *e.g.* 215 mAhg^{-1} for Fe_2O_3/graphene composite [156] and 150 mAh g^{-1} for ultrathin anatase TiO_2 nanosheets.[157] Moreover, the specific capacity of FeS nanosheets electrode can recover to 630 mAh g^{-1} when the current density is reverted

back to 0.1 A g^{-1} from 6 A g^{-1} (10C). Meanwhile, the hierarchical FeS particle electrode shows 9^{th}-cycle discharge capacities of 619 and 217 mAh g^{-1}at current densities of 0.1 A g^{-1} (0.16C) and 6 A g^{-1} (10C), respectively. The FeS nanoplates electrode displays lower 9^{th}-cycle discharge capacities of 530 and 133 mAh g^{-1} at current densities of 0.1 A g^{-1} (0.16C) and 6 A g^{-1} (10C), respectively. The superior rate capability of the hierarchical FeS nanosheet electrode over the other two nanostructures is mainly attributed to their thin thickness and tiny nanograins, which does not provide a large effective interaction area between electrode materials and electrolyte, but also shortens the Li diffusion path and facilitates charge transport kinetics. The charge transport kinetics is further examined by electrochemical impedance spectra (EIS). The Nyquist plots (Figure 3-10b) are obtained from tested cells after five discharge/charge cycles. The FeS nanosheet electrode exhibits smallest radius of the semicircles in the Nyquist plot, indicating lowest charge-transfer resistance than that of hierarchical FeS particle and nanoplates electrode.

3.3.3.3 Cycling Stability and effect of carbon coating

Stable cyclic performance of electrode material is also important for practical appilcation. The cycling performance of the hierarchical FeS nanosheets, hierarchical FeS nanosheets and FeS nanoplates based electrodes were examined at a current density of 0.1 A g^{-1} between 0.01V and 3.0V for up to 100 cycles (Figure 3-11).

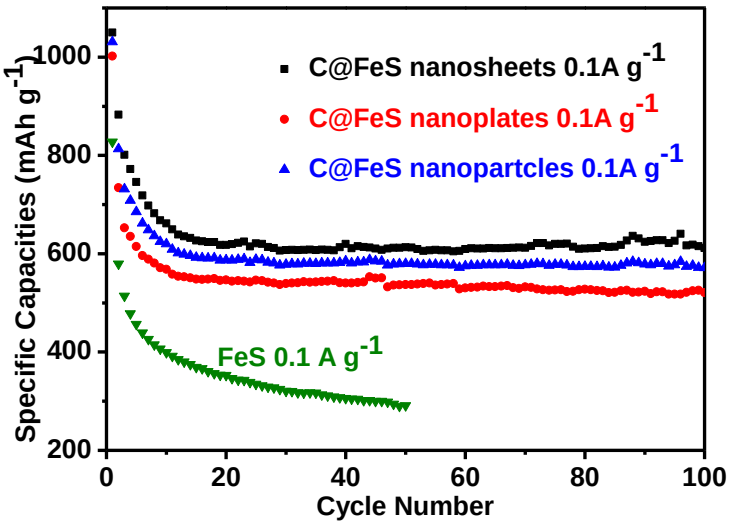

Figure 3-11: Comparison of the cycling performance of the hierarchical FeS nanoparticles, hierarchical FeS nanosheets, FeS nanoplates and bare FeS crystals based electrode at a current density of 0.1 A g^{-1}

At a current density of 0.1 A g^{-1}, the discharge capacity of the hierarchical FeS nanosheet electrode is 623 mAh g^{-1} during the 20th cycle and remains to be 615 mAh g^{-1} in the 100th cycle, which indicates 98.7% capacity retention from the 20th cycle to the 100th cycle. The hierarchical FeS nanoparticles also exhibits good cyclability with discharge capacities of 592 mAh g^{-1} during the 20th cycle and 580 mAh g^{-1} during the 100th cycle. Although the FeS nanoplates electrode has a lower specific capacity, it still exhibits an acceptable cycling performance of 550 mAh g^{-1} during the 20th cycle, and maintains at 525 mAh g^{-1} during the 100th cycle.

Nanostructuring is one of the factors contributing to the stable cycling performance of conversion reaction electrodes. The conversion reaction between FeS and Li with the formation of Li_2S and Fe can produce volume change of up to 200%. Nanostructuring

is expected to be an effective strategy to accommodate the structural stress induced by the huge volume change. In the cases of sulfur and sulfides as electrode materials, formation and dissolution of lithium polysulfides into electrolyte is detrimental to the continuous cycling of these materials.[158, 159] Coating or compositing with carbonaceous materials has been proven an effective approach to minimize lithium polysulfides dissolution and facilitate cycling performance of Li-Sulfur batteries and LIBs with sulfides electrode.[158-161] It is believed that the good cycling stability of these FeS architectures is the double contribution from nanostructuring and carbon coating.

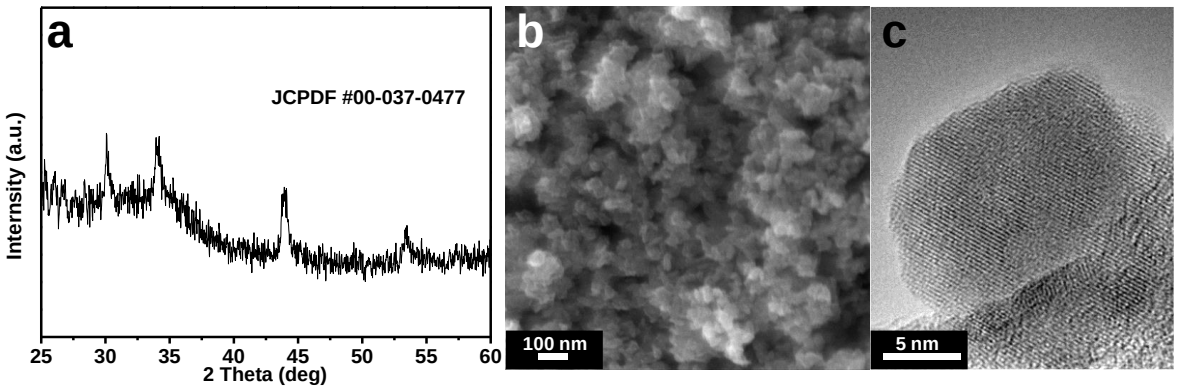

Figure 3-12: (a) SEM image of bare FeS nanoparticles synthesized in H_2O; (b) XRD pattern of the FeS nanoparticles; (c) HRTEM image of bare FeS nanoparticles showing no noticeable carbon layers.

To verify the effect of carbon coating, FeS nanocrystals without carbon coating was prepared for comparison. The XRD pattern (Figure 3-12a) confirms that nanocrystals prepared through this approach is of the same phase: Troilite-phase FeS. The SEM image (Figure 3-12b) of the non-carbon coated FeS shows nanocrystals of ~30 nm. The HRTEM image (Figure 3-12c) shows that there is no trace of amorphous carbon

layer on these FeS nanoparticles after annealing. The cycling performance of the bare FeS nanoparticles is also plotted in Figure 3-11, showing a poor cyclability. At a current density of 0.1 A g^{-1}, the specific capacity of the bare FeS nanoparticles is 404 mAh g^{-1} during the 10^{th}-cycle, which quickly decays to 292 mAh g^{-1} during the 50^{th} cycle with only 72.3% capacity retention. The improved cycling stability of carbon coated FeS nanostructures–based electrode than bare FeS nanocrystals-based electrode may be due to the dissolution of polysulfides for the bare FeS nanocrystals.[91, 92]

Table 3-1: CHNS elemental analysis of electrolytes from de-assembled coin cells after 50 cycles.

	Elemental Weight (%)	
Sample ID	**C**	**S**
C@FeS	97.1	<0.5
FeS	95.5	2

CHNS elemental analysis (Table 3-1) shows that electrode based on carbon coated FeS nanosheets has less polysulfide dissolved in the electrolyte than bare FeS nanocrystals, which further confirm the carbon effect on preventing polysulfide dissolution and sustaining cycling stability.

3.4 Conclusion

In summary, carbon coated FeS nanostructures (hierarchical FeS nanosheets, hierarchical nanoparticles and hexagonal-shaped nanoplates) have been prepared via a solution-based synthesis. In the formation of FeS nanosheets, 1-dodecahtnil does not only act as the sulfur source but also as a surfactant templating the growth of hierarchical structure. The resultant FeS nanosheets are polycrystalline, implying that the growth of nanosheets is not related to the crystal structure of the Troilite FeS, and this synthetic approach may be extendable to synthesis of other transition metal sulfides.

The hierarchical FeS nanosheet delivers promising Li storage properties with high specific capacities, stable cyclability and good rate performances. It depicts a specific capacity of 233 mAh g^{-1} during the 100^{th} cycle at a 10-C discharge rate, which is attractive for the development of LIBs with high power densities and high energy densities. The excellent Li storage performance of the FeS nanosheets is mainly attributed to: (1) the open networks of thin nanosheet morphology that can effectively accommodate large volume changes induced during the charge/discharge process; (2) the ultrathin thickness of nanosheets shortens the diffusion paths of charge carriers and allows faster charge transfer; (3) the carbon layers can absorb and trap the polysulfides generated during the conversion reaction of sulfides, which reduces the dissolution of polysulfides and improves the cycling stability of the electrode.

However, FeS has a high redox reaction potential, which will limit the output voltage and energy densities of full cells when applied as anode for LIBs. Besides, FeS has a

limited theoretical capacity of 609 mAh g^{-1}, which is still lower than demanding capacities for lithium ion battery anodes. These considerations lead us to the next work studying the lithium storage properties of FeS-ZnS compositing nanosheets.

4. Synthesis and Characterization of FeS-ZnS Composite Nanosheets

4.1 Overview

Metal sulfides have been intensively investigated as electrode materials of lithium batteries. In practical applications as electrode materials for LIBs, metal sulfides also encounter some problems such as poor cycling performance resulting from large volume change and severe aggregation during repeated lithiation/de-lithiation. Several measures have been demonstrated to mitigate the volume change and aggregation:(1) nanostructuring: various metal sulfide nanostructures, such as FeS nanocrystals,[98] ZrS_2 nanodisks,[99] CoS nanoflowers,[100], has exhibited improved lithium storage performance from their bulk counterparts; (2) forming hollow or porous structures: hollow spheres of CoS_2 and CuS deliver good cycling stability; [162, 163] (3) coating or compositing with carbonaceous material: FeS-embedded carbon microsphere show high specific capacity and excellent high-rate performance.[164]

Up to date, most research concentrate on lithium storage performance improvement of individual metal sulfides, there is no report on composite metal sulfides with defined nanostructures, although some research attempts on composite metal oxides have proved success in lithium storage performance improvement. Literature shows that composite Fe_2O_3/SnO_2 nanostructure have advantageous lithium storage performance, both in specific capacities and cycling performance, compared with individual Fe_2O_3 or SnO_2.[102, 103] Besides, some composite metal oxides, such as SnO_2/TiO_2 nanotube hybrids,[104] branched α-Fe_2O_3/SnO_2 nanoarchitectures,[105] NiO/ZnO hybrid nanofibres,[106] ZnO/CoO nanoflowers[107] and Fe_2O_3/CuO nanowires[108]

all exhibit different redox reaction voltage plateaus from their constituent individual component.

Among various transition metal sulfides, iron sulfides have been intensively investigated as electrode materials in lithium primary batteries due to its good lithium storage properties, natural abundance, low cost and environmental friendliness. However, both FeS and FeS_2 exhibit voltage plateaus of around 1.0V vs. Li/Li^+ during lithiation, which makes it inappropriate as anode materials in LIBs. The lithiation of ZnS involves both conversion reaction and alloying reaction, and the dual Li storage mechanism contributes to higher Li storage capacities but also brings about large volume change.

Combining the merits and disadvantageous of FeS and ZnS, in this work, uniform FeS/ZnS composite nanostructures of various Fe/Zn molar ratios were prepared by a simple and scalable solution based synthesis. The lithium storage properties of the hybrid sulfides, including the lithiation/delithiation potentials, specific capacities and rate capabilities, are shown to be greatly related to Fe/Zn ratio. The composite sulfide with molar ratio Fe/Zn=7.29 exhibits a higher and stable capacity of 805, 705, 567, 381 and 245 mAh g^{-1} at current densities of 0.1 A g^{-1}, 0.5 A g^{-1}, 1 A g^{-1}, 2 A g^{-1} and 5 A g^{-1}, respectively. The electrochemical performance is superior to single component ZnS and FeS prepared under similar reaction conditions. The coexistence of the heterogeneous sulfides could behave as dispersants of each other. During the lithiation reaction, heterogeneous metals reduced from the composite sulfides are not liable to aggregate, nor are the heterogeneous sulfides formed during delihtiation. The enhanced lithium storage performance of the composite FeS/ZnS nanosheets can be

ascribed to the mutual segregation of the heterogeneous sulfides, sustaining a high capacity upon cycling.

4.2 Experimental Procedure

4.2.1 Chemical Synthesis

Synthesis of FeS-ZnS composite nanosheets: Iron (III) acetylacetonate/$Fe(acac)_3$ (Aldrich, ≥99.9%) and zinc acetylacetonate/$Zn(acac)_2$ (Strem Chemicals, 98%) of total 0.2 mmol were first weighed with different Fe/Zn molar ratios according to Table 4-1.

Table 4-1: Weight amounts of $Fe(acac)_3$ and $Zn(acac)_2$ in different samples

Metal Precursors / **Molar Ratio (Fe/Zn)**	**$Fe(acac)_3$ (mg) (MW = 353.17 g/mol)**	**$Zn(acac)_2$ (mg) (MW = 263.59 g/mol)**
Pure FeS	70.634	-
7:1	61.805	6.590
3:1	52.976	13.180
1:1	35.317	26.359
Pure ZnS	-	52.718

Mixed $Fe(acac)_3$ and $Zn(acac)_2$powderwere dissolved in 10 mL Oleylamine(OLA, Aldrich, 70%) in a three-neck flask. The solution was heated to 120°C under

continuous magnetic stirring and purged with Ar gas for 30 min. Then, 1 mL of 1-dodecanethiol (Aldrich, ≥98%) was injected into the solution. After that, the reaction mixture was heated to 220°C and maintained at 220°C for 20 minute before naturally cooled down to room temperature. The resultant solution was dripped into hexane and the precipitates were collected by centrifugation at 7000 rpm for 10 min. The final product was dried in a vacuum oven.

Synthesis of Pure ZnS Control Sample: 1 mmol $ZnCl_2$ (Fluka), 0.1 mmol octadecylamine (Aldrich, 97%) and 0.2 mL ethylenediamine (Sigma-Aldrich) were first added to 12 mL ethylene glycol (Alfa Aesar, 99%). The solution was then heated to 120°C under strring and Ar purge.[165] After that, 12 mL ethylene glycol containing 1 mmol Thiourea was injected. The reaction mixture was then heated to 150°C and maintained at 150°C for 2 hours before naturally cooled down to room temperature. The resultant solution turned milky white. The product was precipitated with ethanol followed by repeated centrifugation. The final product was dried in a vacuum oven.

All the synthesized samples were annealed in a tube furnace at 450^{o}C for 1 hour under continuous Ar flow to have residual organic components transformed to amorphous carbon.[166, 167]

4.2.2 Materials Characterization

Powder X-Ray Diffractometer (Shimadzu Standard) with Cu K_{α} source (λ = 0.15418 nm) was used to determine the phases with a scan rate of 1^{o}/min. Sample morphology was examined by both the Field Emission Scanning Electron Microscope/FESEM

(JEOL JSM-7600F) and the Transmission Electron Microscope/TEM (JEOL 2100F) operating at 200 kV. Compositional concentration (in wt%) of Fe and Zn in the final product was obtained by utilizing Inductively Coupled Plasma Mass Spectrometry (ICP-MS).

4.2.3 Electrochemical Characterization

The working electrode for the coin cell battery was prepared by first mixing the active material, super-P carbon (Aldrich) and polymer binder (PVDF, Aldrich) with an 8:1:1 ratio (w/w/w) in *N*-methyl-2-pyrrolidinone (NMP). Next, the mixture was stirred for several days to a slurry state, which was then casted onto a 14-mm diameter copper foil and dried in a vacuum oven at 50°C for 12 hours.

The assembly of coin cell batteries was carried out in an Ar-filled glovebox with moisture and oxygen concentrations of <1.0 ppm.[167] Lithium metal, Celgard 2400 membrane and solution mixture of 1M lithium hexafluorophosphate ($LiPF_6$) dissolved in ethylene and dimethyl carbonate (EC/DMC, 50:50 w/w) were used as counter/reference electrode, separator and electrolyte, respectively.[166, 167] To study and evaluate the Li-storage properties of the nanocomposites, a series of electrochemical measurements were conducted based on the half-cell configuration.[166, 168, 169] Firstly, cyclic voltammetry (0.01–3 V, scan rate of 0.5 mV s^{-1}) was carried out using an electrochemical workstation (Solartron) to give the Cyclic Voltammogram (CV). After that, a NEWARE multichannel battery test system with galvanostatic charge and discharge (voltage window of 0.01–3.0 V) was engaged to characterize the rate capability of the assembled cells.

4.3 Results and Discussion

4.3.1 Crystallographic characterization and morphology characterization

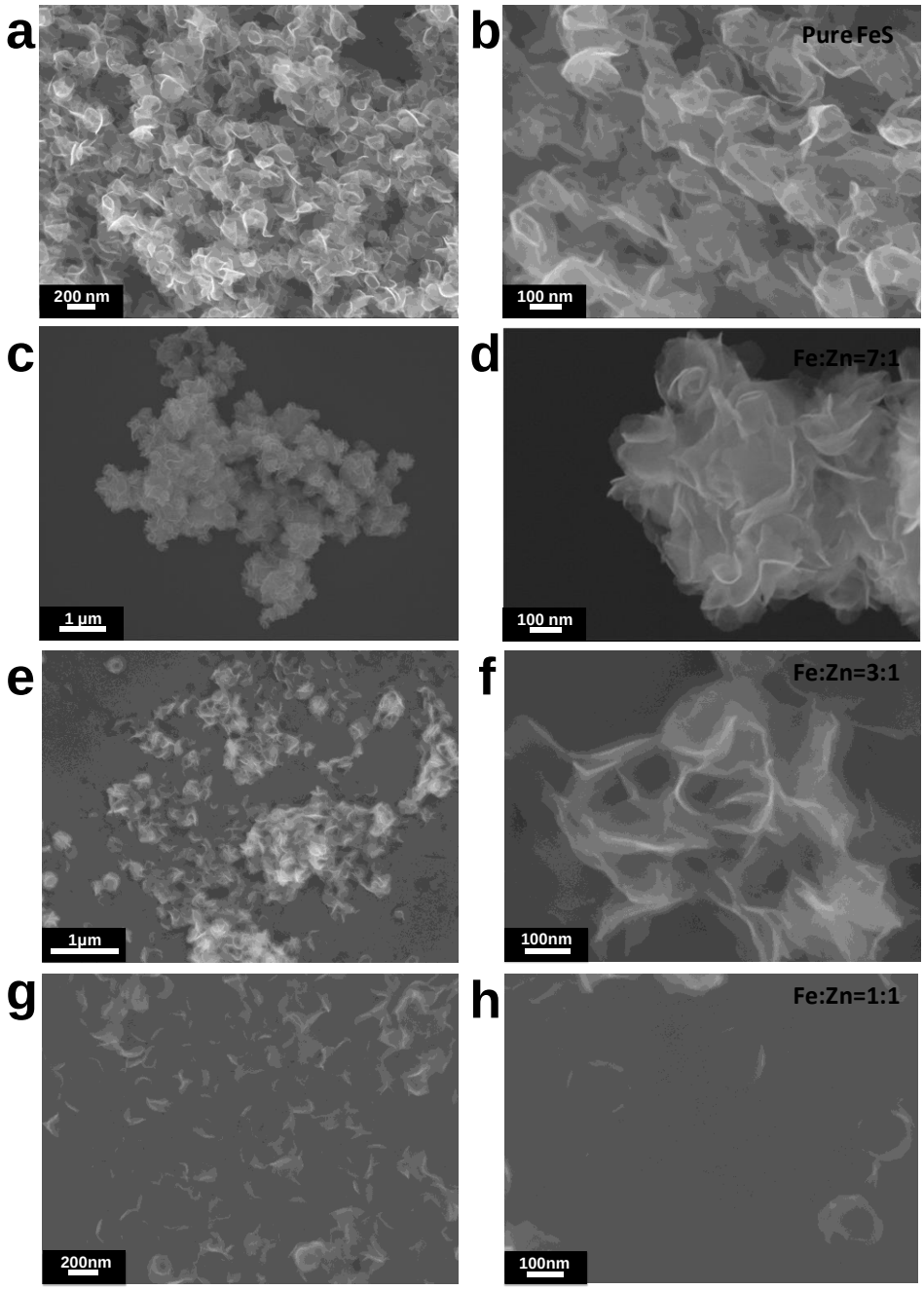

Figure 4-1: SEM images of as-synthesized product with different Fe/Zn precursor ratios: (a) and (b) pure FeS; (c) and (d) Fe/Zn=7:1; (e) and (f) Fe/Zn=3:1; (g) and (h) Fe/Zn=1:1. In the subsequent discussion, pure FeS, Fe/Zn=7:1, Fe/Zn=3:1 and Fe/Zn=1:1 are denoted as S-1, S-2, S-3 and S-4, respectively.

The morphological information of the as-synthesized products with different Fe/Zn ratios is presented in Figure 4-1. The SEM images reveal formation of nanosheets regardless of varying precursor ratios. Those nanosheets have lateral lengths of approximately 100–200nm and ultrathin thickness observed with significant flexibility. Thin nanosheet offers larger active surface for electrolyte-electrode interaction and shorter path for charge transport. Besides, the flexibility of nanosheet enhances its stress tolerance. However, the construction of those nanosheets evolves from S-1 to S-4. As observed from Figure 4-1a, pure FeS nanosheets are interconnected forming a porous network. With increasing ratio of Zn in the precursor from Figure 4-1c to Figure 4-1h, the nanosheet dimension gets smaller. In S-4 with Fe/Zn=1, the nanosheets are free-standing instead of forming interconnected network. Controlled experiment with $Zn(acac)_2$ as the only metal precursor was also conducted, but result in no product. It is not confirmed yet whether $Zn(acac)_2$ participate in the reaction forming ZnS. If $Zn(acac)_2$ is involved, it is possible that Zn-Fe-S ternary sulfide compound or FeS/ZnS hybrid sulfide is formed. Further investigation on the phases and compositions is required.

The XRD pattern in Figure 4-2 shows pure FeS formation with $Fe(acac)_3$ as the only precursor. Only Troilite-phase FeS is present with diffraction peaks at 2θ = 29.95°, 33.71°, 43.18° and 53.17°, corresponding to the the (110), (112), (114) and (300) planes, respectively. With the addition of zinc source, composites of wurtzite ZnS (JCPDS #00-036-1450) and troilite FeS (JCPDS #00-037-0477) are formed. In the XRD pattern of S-2, diffraction peaks from (110), (112), (114) and (300) planes of troilite FeS remains pre-dominant. And, small peaks of wurtzite ZnS can be observed

at 2θ=56.36° and 65.97° corresponding to the (112) and (104) planes, respectively. As the ratio of Zn increases to Fe/Zn=3:1 in S-3, diffraction peaks from (112) and (104) planes of wurtzite ZnS becomes more obvious.

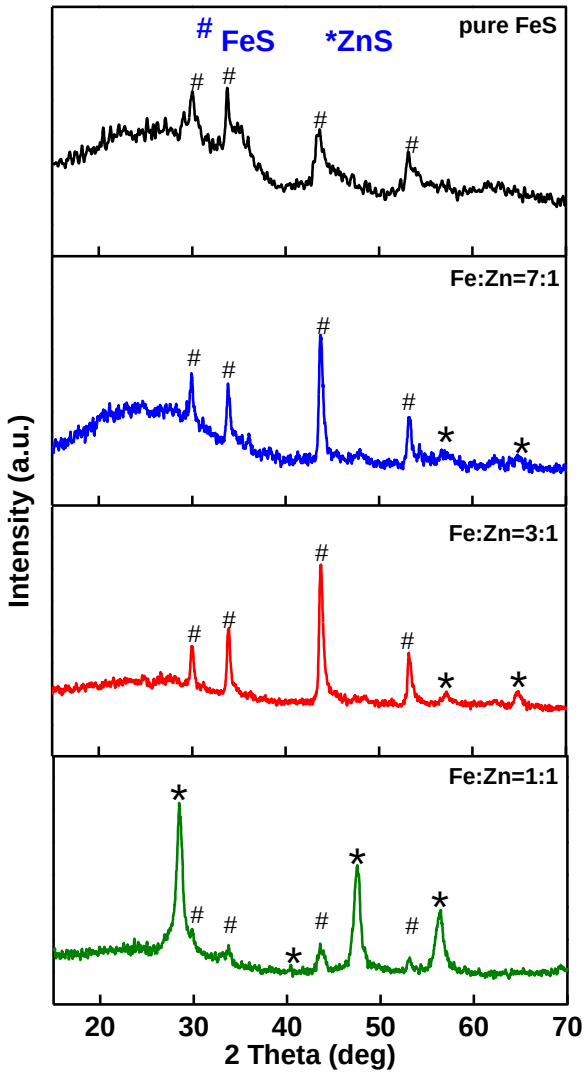

Figure 4-2: XRD pattern of as-synthesized product with different Fe/Zn precursor ratios.

With the Zn ratio increase to Fe/Zn=1:1 in S-4, the diffraction peaks of wurtzite ZnS becomes more pre-dominant than that of FeS. Four well-resolved diffraction peaks at 2θ = 28.49°, 39.50°, 47.50° and 57.40° were observed, corresponding to the (002),

(102), (110) and (201) planes of wurtzite ZnS, respectively. At the same time, the diffraction peaks of Troilite FeS at 2θ = 29.95°, 33.71°, 43.18° and 53.17° still can be identified but with significant reduced intensity. It signifies that better-crystalline and larger amount of ZnS forms with the increasing Zn ratio in precursor.

According to the phase and crystallographic characterization, it can be concluded that FeS/ZnS hybrid metal sulfides have formed instead of Fe-Zn-S ternary sulfide compound.

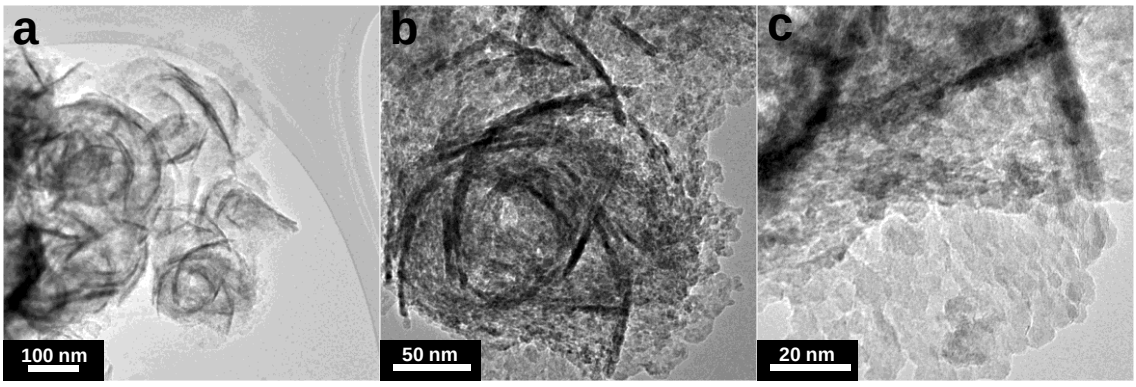

Figure 4-3: (a) TEM image of the FeS/ZnS composite nanosheet S-3; (b) and (c) higher-magnification TEM images of S-3.

Figure 4-3a to Figure 4-3c show TEM images of the FeS/ZnS composite nanosheet synthesized from precursor ratio of Fe/Zn=3:1 with increasing magnification. It can be observed from Figure 4-3a that the nanosheets are flexibly curled forming a flower-like structure. Each individual nanosheet is hierarchical and composed of interconnected nanocrystals (Figure 4-3b). The sizes of the nanocrystals are estimated to be smaller than5nm (Figure 4-3c). The nanosheet morphology and hierarchical feature of the composite sulfides are similar to that of pure FeS. The ultrafine

nanocrystal building blocks provide larger electrolyte-electrode interaction area and shorter diffusion path for lithium ions. The flexible nanosheet holding the ultrafine nanocrystals together help sustain a continuous electronic transport and structural integrity during cycling.

However, it is still not affirmable whether direct hybriding of individual FeS nanosheet and ZnS nanosheet is formed or FeS and ZnS coexist on one nanosheet. The distribution of FeS and ZnS needs to be investigated.

4.3.2 Compositional Analysis

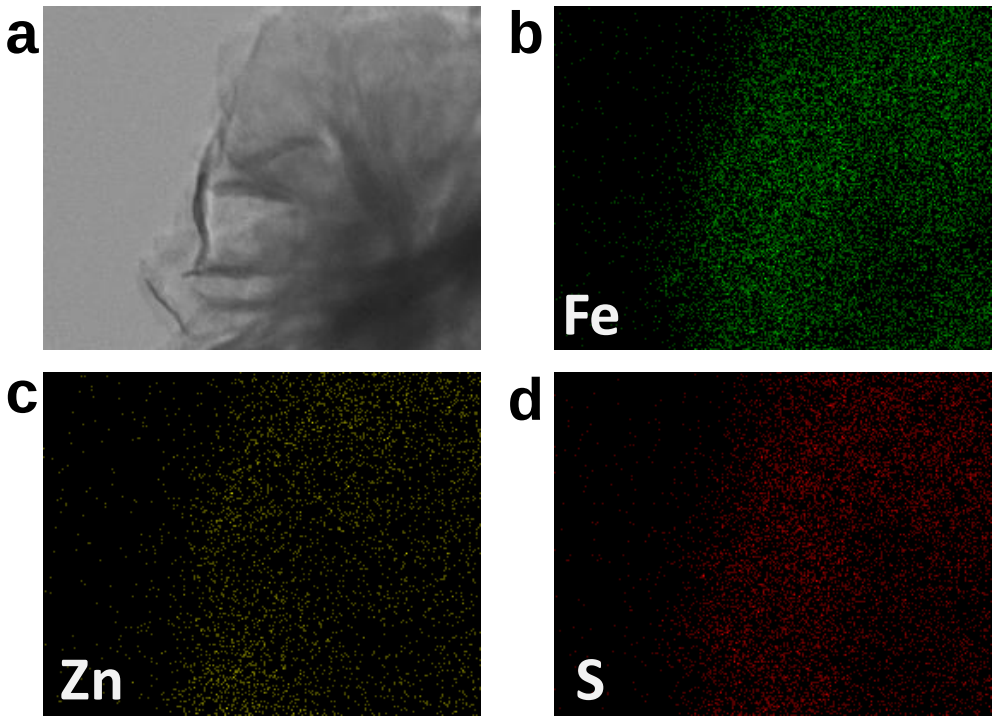

Figure 4-4: (a) STEM image of the FeS/ZnS composite nanosheet S-3; (b), (c) and (d) the corresponding elemental mapping of the Fe, Zn and S, respectively.

STEM-EDX elemental mapping was carried out to determine the spatial distribution of constitute elements of the composite nanosheets shown in Figure 4-4. S-3 was selected as a representative sample. Elemental mappings of Fe, Zn and S show identical distribution, indicating that each compositing nanosheet is composed of randomly-distributed both FeS and ZnS nanocrystals rather than forming separate FeS nanosheet and ZnS nanosheet.

Therefore, a single nanosheet consists of both trolite FeS and wurtzite ZnS nanocrystals instead of separated FeS nanosheet and ZnS nanosheet. This opposes the initial understanding that ZnS and FeS might form nanosheets of only its own compound but not co-exist on a single nanosheet.

Table 4-2: ICP-MS test results of synthesized samples with different Fe/Zn molar ratios

Molar ratio of Fe/Zn in precursors	Weight ratio of Fe/Zn	Fe in product (at %)	Zn in product (at %)	Molar ratio of Fe/Zn in product
Pure FeS	N/A	100	0	N/A
7:1	6.22:1	87.94	12.06	7.29:1
3:1	2.93:1	77.44	22.56	3.43:1
1:1	1.05:1	55.08	44.92	1.23:1
Pure ZnS*				

*Synthesis of pure ZnS was attempted with $Zn(acac)_2$ added as the only metal precursor, but there was no precipitates.

Inductively Coupled Plasma Mass Spectrometry (ICP-MS) was performed to confirm the ratios of Fe and Zn in the final product. Table 4-2 summarizes the quantitative information from ICP-MS test. Pure $Fe(acac)_3$ leads to formation of pure FeS nanosheets. For products with precursor ratios of Fe/Zn= 7:1, 3:1 and 1:1, the Fe/Zn weight ratios in the resultant products are 6.22:1, 4.96:1, 2.93:1 and 1.05:1, corresponding to atomic ratios of 7.29:1, 3.43:1 and 1.23:1, respectively.

It follows the institution that amount of ZnS formed increases with the increasing amount of $Zn(acac)_2$ precursor added. In addition, it is worth noting that the molar ratios of Fe/Zn in products are slightly higher than that in reactants, and the ratio difference between product and reactant decreases with increasing Zn proportion. The slightly higher Fe/Zn molar ratios in the final product suggest the preferential formation of FeS over ZnS. Without $Fe(acac)_3$ in precursor, ZnS is not formed either. Therefore, it is concluded that the nucleation and growth of ZnS is facilitated by FeS. And, with the increasing Zn proportion in precursor, larger proportion of ZnS is nucleated and grown. According to Han and co-worker, preferential reaction between a particular cation and its counterbalance anion can be attributed to several factors, notably the electron affinity of the reacting species.[170] Since Fe has a more positive electron affinity value than Zn ($E_{ea\ (Fe)}$ = 15.7 kJ/mol; $E_{ea\ (Zn)}$ = 0 kJ/mol), this means that Fe is more readily to donate its electrons in order to form a stable compound with S ($E_{ea\ (S)}$ = -200 kJ/mol), thus explaining the reason behind preferred FeS formation over ZnS in this case.

4.3.3 Reaction Mechanism

Proposed formation process of the hierarchical composite nanosheets is illustrated in Figure 4-5. In literature, most 2D nanostructures are forming from layer-structured materials, in which the in-plane bonds are covalent, whereas weak Van Der Waals force presents between the layers. As a result, the surface energy of the planar layer as terminating surface is lower, and construction to 2D nanostructures are preferred. Both Troilite FeS and Wurtzite ZnS have layered atomic arrangement of alternating sulfur and metal layer, but covalent bonds present both within the layers and between the adjacent layers. In addition, the hierarchical feature further indicates that the nanosheet formation does not directly relate to the crystal structure of FeS or ZnS. What's more, the similarity in crystal structure may facilitate the co-growth of FeS and ZnS nanocrystals on each individual nanosheet. It is proposed that during the reaction FeS nanocrystals forms first and self-arrange to 2D distribution with the micelles formed by dodecane-thiolate acting as the soft template, and the formed FeS nanocrystals subsequently facilitate the nucleation and growth of ZnS nanocrystals adjacent to them.

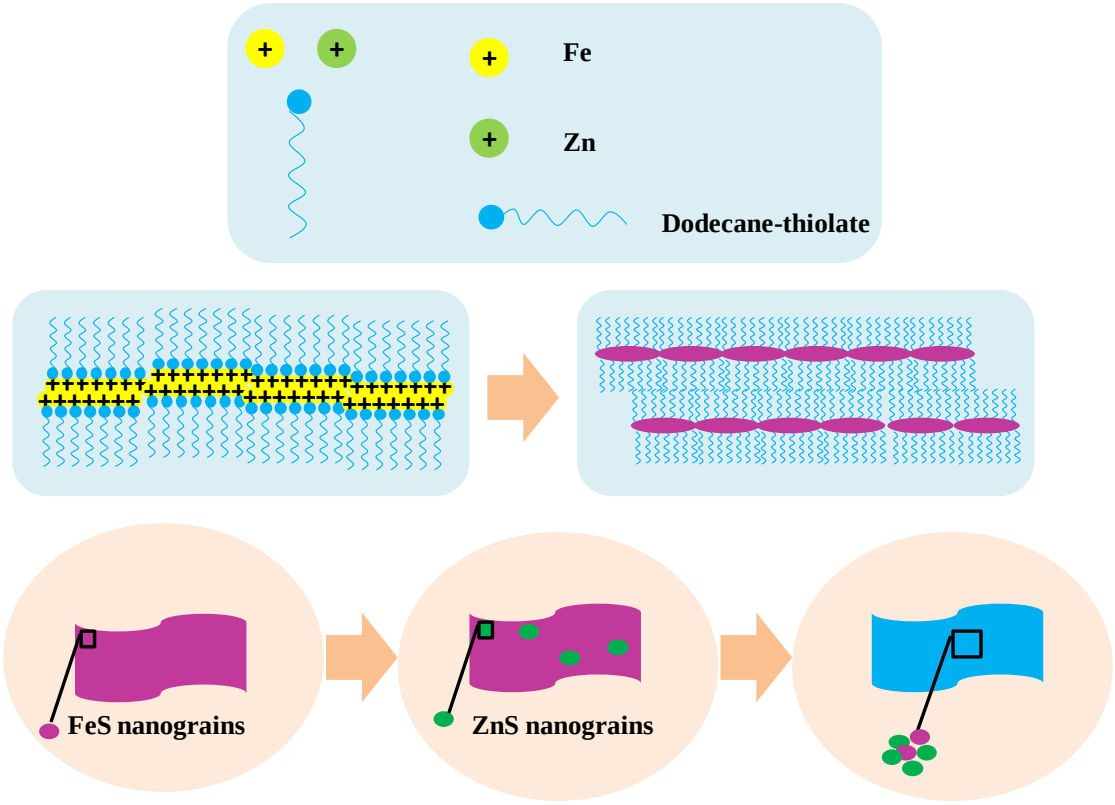

Figure 4-5: Proposed reaction mechanism for the formation of composite FeS/ZnS hierarchical nanosheets

4.3.4 Electrochemical Characterization

4.3.4.1 Cyclic Voltammetry

To evaluate the composite effect of metal sulfides and the effect of composite ratios on lithium storage, a series of comparative electrochemical properties, including cyclic voltammetry, rate capability and cycling performance were conduced based on coin cells with Li foil as both the counter and the reference electrode.

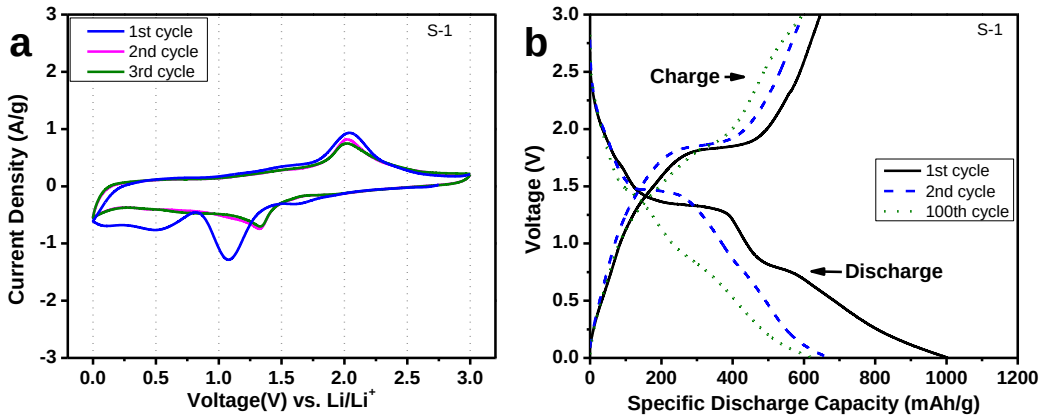

Figure 4-6: (a) CV curves of electrodes based on S-1 for the 1st, 2nd and 3rd cycles. (b) Discharge/charge voltage profiles of S-1 at a current density of 0.1A g^{-1} for the 1st, 2nd and 100th cycle.

The CV curves for initial three cycles and discharge/charge voltage profiles for the 1st, 2nd and 100th cycle of S-1, S-2, S-3 and S-4 based electrodes are shown in Figure 4-6 to Figure 4-9. Figure 4-6a shows the CV curve for pure FeS nanosheets based electrode. As discussed previously in Section 3.3.3.1, the small anodic peak at 1.65V corresponds to lithium intercalation into the pseudo-layered structure of Troilite-phase FeS, and the sharp anodic peak at ~ 1.05V is attributed to the main conversion reaction between FeS and Li with the formation of Li_2S and nano-Fe. Anodic peaks denoting the main conversion reaction are shifted to a more positive potential at 1.3V in the subsequent 2nd and 3rd cycle during discharge.[90, 137] The broad peak appearing from 0.75V to 0V, which is missing in the subsequent discharges, is totally attributed to SEI formation.[155] The cathodic peak at around 2.05V in the 1st, 2nd and 3rd cycles corresponds to the oxidation of nano-Fe by surrounding Li_2S to the reformation of FeS and release lithium. [135, 137]

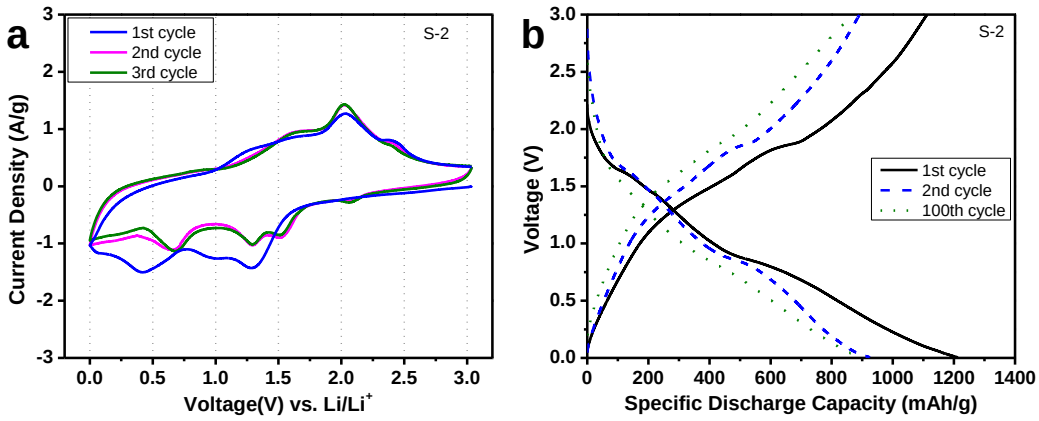

Figure 4-7: (a) CV curves of electrodes based on S-2 for the 1st, 2nd and 3rd cycles. (b) Discharge/charge voltage profiles of S-2 at a current density of 0.1A g^{-1} for the 1st, 2nd and 100th cycle.

CV curve (Figure 4-7b) for S-2 (Fe/Zn=7.29:1 in at%) based electrode shows additional anodic and cathodic peaks compared with that for S-1 (Figure 4-6a). In the 1st cycle discharge, the anodic scanning profile dropping from 1.5V indicates the starting of FeS reduction. The anodic peak at 1.25V results from the conversion reaction between FeS and Li. And, a shallow peak appearing at around 0.75V is ascribed to the deposition of ZnS to Zn embedding in Li_2S matrix. Since the quantity of FeS is about 8 times of ZnS, the conversion reaction peaks of FeS dominates. The broad reduction peak from 0.5V to 0V in the 1st cycle CV profile corresponds to the lithium-zinc alloying reaction with the formation of Li_xZn (the x value can reach ~1.5). The Li-Zn alloying reaction may proceed stepwise, showing several phases with lithium content increase. In the 2nd and 3rd cycle discharge, only two anodic peaks present at 1.25V and 0.75V corresponding to the conversion reaction of FeS and ZnS, respectively. In addition, the shallow dropping of the profile from 0.5V to 0V is

ascribed to the Li-Zn alloying. During the cathodic scan of the 1st cycle, the current increases gradually from 1.0V indicating the starting of oxidation of Zn and Fe. The cathodic peak at 1.6V corresponds to the oxidation of Zn back to ZnS, and the more predominant peak at 2.0V is attributed to the regeneration of FeS. These two cathodic peaks sustains in the subsequent two cycles, while the cathodic peak at 2.4V starts diminishing since the 2nd cycle and disappears in the 3rd cycle.

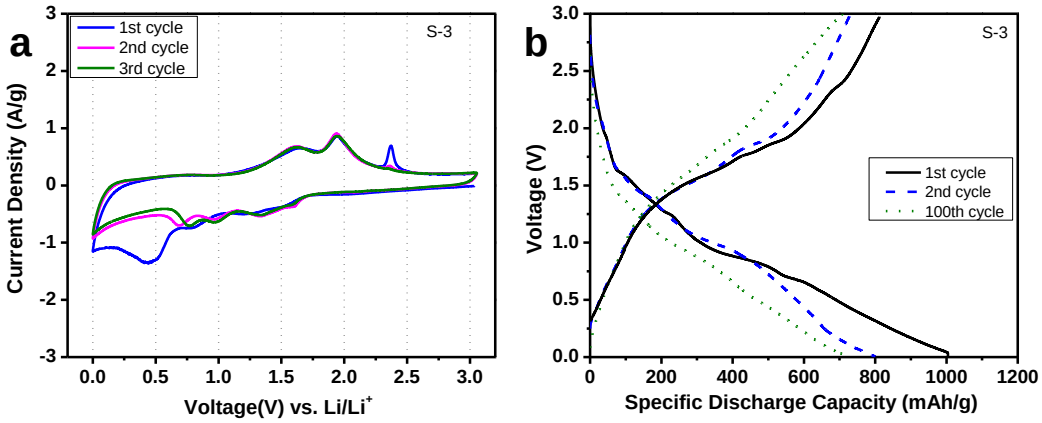

Figure 4-8: (a) CV curves of electrodes based on S-3 for the 1st, 2nd and 3rd cycles. (b)Discharge/charge voltage profiles of S-3 at a current density of 0.1A g^{-1} for the 1st, 2nd and 100th cycle.

In the 1st cycle discharge of S-3 based electrode (Figure 4-8c), shallow anodic peaks at 1.1V and 0.75V correspond to the conversion reaction of FeS and ZnS with lithium, respectively. Anodic peaks denoting the main conversion reaction are shifted to more positive potential at 1.3V and 0.75V in the subsequent 2nd and 3rd cycle during discharge. In the voltage range of 0.55V to 0V, the broad peak is attributed to the Li-Zn alloying and SEI formation. The peak disappears during the 2nd and 3rd cycle discharge, signifying that the Li-Zn alloying reaction is much inefficient than the 1st

cycle. Three cathodic peaks at 1.6V, 1.9V and 2.4V correspond to the oxidation of Zn and Fe back to ZnS and FeS, respectively. The intensities of cathodic peaks sustains during the 1st, 2nd and 3rd cycle.

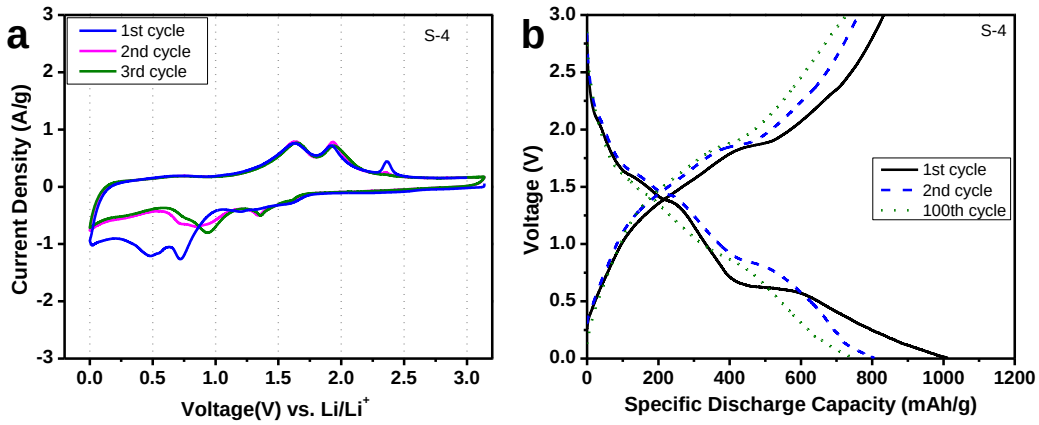

Figure 4-9: (a) CV curves of electrodes based on S-4 for the 1st, 2nd and 3rd cycles. (b)Discharge/charge voltage profiles of S-4 at a current density of 0.1A g^{-1} for the 1st, 2nd and 100th cycle.

In the 1st cycle discharge of S-4 based electrode (Figure 4-9d), the reaction peaks for ZnS becomes more dominant. The anodic peaks at 0.75V and 0.5V correspond to the conversion reaction of ZnS and Li-Zn alloying, respectively. During the 2nd and 3rd cycle discharge, the conversion reaction FeS and ZnS at 1.3V and 0.8V are observed, respectively. Three cathodic peaks at 1.6V, 1.9V and 2.4V correspond to the oxidation of Zn and Fe back to ZnS and FeS, respectively. The intensities of cathodic peaks sustains during the 1st, 2nd and 3rd cycle.

Based on our observation, the composite nanosheets S-2, S-3 and S-4 based electrode has the same cathodic and anodic reactions at similar potentials regardless of the

compositional difference, but with slight variation in peak width and intensity during the 1st, 2nd and 3rd cycles.. This leads to a conclusion that the constituent components of the composite sulfides react separately with lithium. However, as the content of Zn increases, the peaks associated with ZnS become progressively significant. For example, the oxidation peak for ZnS at 1.6V gets higher in intensity from S-2 to S-4. Besides, for S-4 based electrode, which has equivalent amount of Zn and Fe, the oxidation peak for Zn at 1.6V is close in intensity compared with the oxidation peak for Fe at 1.9V.

Table 4-3: The 1st discharge (C_{1D}), first charge (C_{1C}), irreversible discharge capacity from beginning to 100th cycle (C_{IR}) and percentage of irreversible discharge capacity of S-1, S-2, S-3 and S-4.

Sample	**C_{1D} (mAh g^{-1})**	**C_{1C} (mAh g^{-1})**	**C_{IR} (mAh g^{-1})**	**Percentage of C_{IR} (%)**
S-1	1002	644	379	37.8
S-2	1211	1111	321	26.5
S-3	1004	812	294	29.3
S-4	1008	830	296	29.4

The discharge and charge capacity of the 1st cycle as well as the irreversible capacity cycling up to 100th cycle obtained from the discharge/charge profiles (Figure 4-6b to Figure 4-9b) are summarized in Table 4-3. S-2 (Fe/Zn=7:1) results in significant enhancement of the 1st cycle capacity during both discharge and charge. The irreversible capacity is greatly reduced for nanosheets with composite compositions, and the improvement can be ascribed to the mutual dispersing effect of two components that prevent particle aggregation upon cycling.

4.3.4.2 Rate Capability

Cycling performance at various current densities was characterized to determine electrodes' rate capability (Figure 4-10). Electrodes based on hybrid sulfides different Fe/Zn compositional ratios were cycled at various current densities. As discussed in the previous work, pure FeS nanosheet based electrode shows a 9th-cycle discharge capacities of around 630, 486, 425, 372 and 266 mAh g^{-1} at current densities of 0.1 A g^{-1}, 0.5 A g^{-1}, 1 A g^{-1}, 2 A g^{-1} and 5 A g^{-1}, respectively.

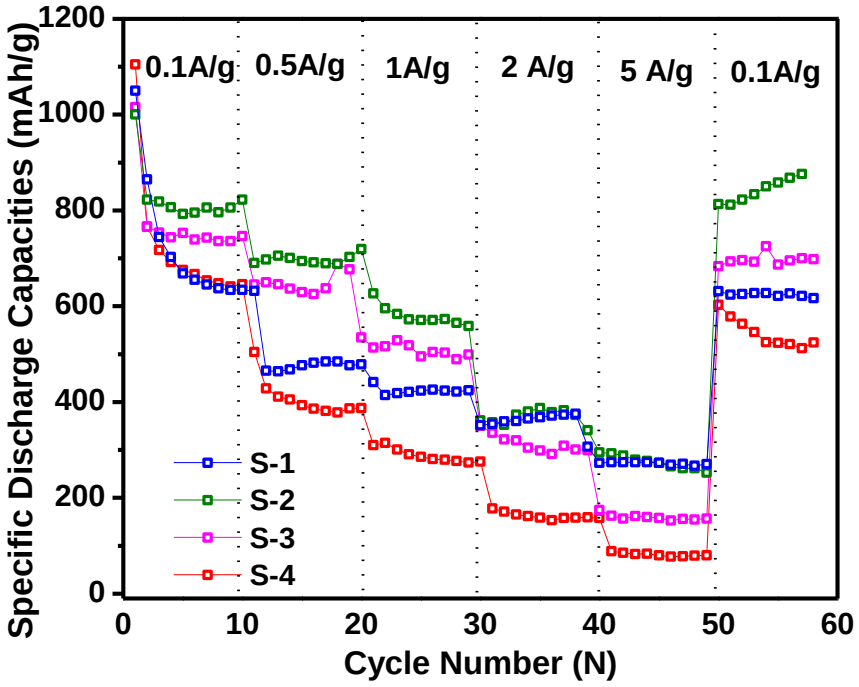

Figure 4-10: Cycling performance of (a) S-1; (b) S-2; (c) S-3; (d) S-4 at various current densities: 0.1 A g^{-1}, 0.5 A g^{-1}, 1 A g^{-1}, 2 A g^{-1} and 5 A g^{-1}.

It can be observed that, S-2 with Fe/Zn=7.29 outperform samples of other ratios, depicting 9th-cycle specific discharge capacities of 805, 705, 567, 381 and 245 mAh g^{-}

^{1} at current densities of 0.1 A g^{-1}, 0.5 A g^{-1}, 1 A g^{-1}, 2 A g^{-1} and, respectively. Moreover, upon current density reverting back from 5 A g^{-1} to 0.1 A g^{-1}, the specific discharge capacity of S-2 increases to 864 mAh g^{-1} from the initial 805 mAh g^{-1}. The gradual increase of capacity during cycling can be attributed to the activation process upon repeated lithiation and de-lithiation, which is commonly observed in many iron-based electrode materials. Compositing a small amount of ZnS to FeS in the hierarchical nanosheet form, the composite sulfides shows 20%-35% increase in specific discharge capacity compared with pure FeS nanosheets at lower current densities from 0.1A g^{-1} to 1A g^{-1}. However, at higher current densities of 2A g^{-1} and 5A g^{-1}, the discharge capacities of FeS/ZnS(Fe/Zn=7:1) composite sulfides are close to that of pure FeS.

In addition, S-3 with Fe/Zn=3:1 depicts 9th-cycle specific discharge capacity of 739, 637, 491, 302 and 151 mAh g^{-1} at current densities of 0.1 A g^{-1}, 0.5 A g^{-1}, 1 A g^{-1}, 2 A g^{-1} and 5 A g^{-1}, respectively. S-4 with equivalent amount of Fe and Zn shows 9th-cycle specific discharge capacity of 647, 389, 276, 161 and 74 mAh g^{-1} at current densities of 0.1 A g^{-1}, 0.5 A g^{-1}, 1 A g^{-1}, 2 A g^{-1} and 5 A g^{-1}, respectively. Although ZnS has both conversion and alloying reaction with lithium, and is expected to contribute higher capacity, with the ratio of ZnS increases, capacity fades more seriously upon cycling, and capacity experience greater drops at higher current densities (*i.e.* 2 A g^{-1} and 5 A g^{-1}).

In summary, S-2 with Fe/Zn=7.29:1 possesses best cycling performance and rate capability. As discussed in the previous work, the superior rate capability of carbon coated FeS nanosheets is attributed to its advantageous hierarchical nano-construction

enabling more effective electrode/lithium interaction and faster charge transport. With the compositing of ZnS to FeS, there is great increase in capacity at lower rates due to higher capacity of ZnS and the synergistic effect of compositing FeS and ZnS, while the capacity almost levels with that of pure FeS at high rates. In addition, with the increasing amount of ZnS formation, the disadvantageous of ZnS, such as poor reversibility and poor rate performance become more evident, causing the deterioration of lithium storage performance of S-3 and S-4 compared with S-2.

4.3.5 Effect of uniform hybriding

For comparison, mixture of FeS nanosheets and ZnS nanoparticles are prepared by physically mixing these two components of 7.29:1 in weight ratio during slurry preparation process. CV curve and rate capability of the FeS/ZnS mixture were shown in Figure 4-11.

The CV curve shows distinctive discharge and charge peak for FeS and ZnS. The mixture depicts 9^{th} cycle specific discharge capacity of 406, 392, 272, 225 and 162 mAh g^{-1} at current densities of 0.1 A g^{-1}, 0.5 A g^{-1}, 1 A g^{-1}, 2 A g^{-1} and 5 A g^{-1}, respectively (Figure 4-11b). The specific discharge capacity of the mixture is lower than FeS/ZnS composite nanosheet at all current densities. In addition, the discharge capacity experience gradual fading at initial cycles even at a low current density of 0.1 A g^{-1}.

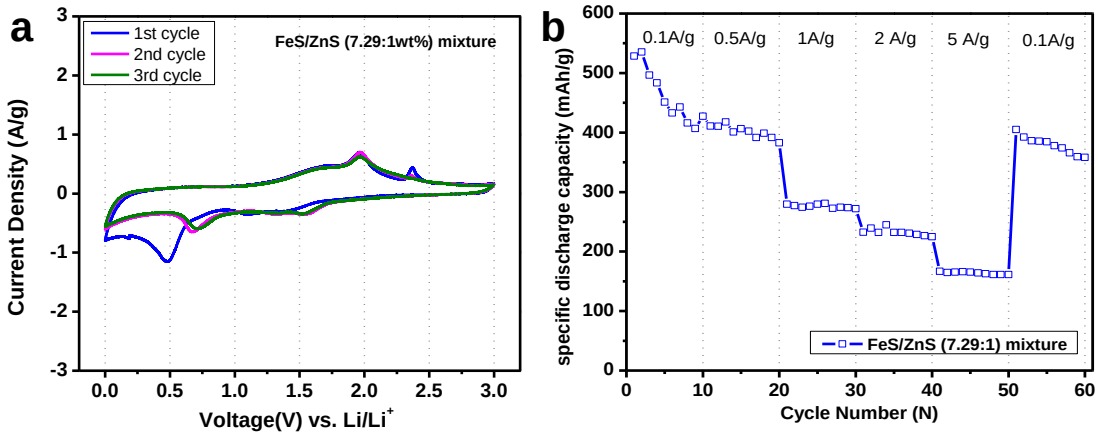

Figure 4-11: (a) CV curves for the 1st, 2nd and 3rd cycles, and (b) cycling performance at various current densities of electrode based on FeS/ZnS mixture 7.29:1 in weight ratio.

The worse performance of the physical mixture might be due to the non-uniform nanostructure, resulting in disrupted charge transport. While in the uniform composite hierarchical nanosheets, the nanocrystal building blocks are held together enabling continuous charge transport. In addition, the coexistence of the heterogeneous sulfides could behave as dispersants of each other.

4.4 Conclusion

In summary, carbon coated composite nanosheets composed of troilite FeS and wurzite ZnS nanocrystals have been synthesized via a organic solution-based synthesis. The compositional ratio of FeS and ZnS can be varied by varying the compositional ratio in precursor. The Fe/Zn weight ratios in final products are slightly higher than that in precursors, and ZnS cannot be formed without FeS formation . Therefore, it is proposed that, in the formation of the composite nanosheets, firstly the dodecane-thiolate templates the growth of FeS nanocrystals to polycrystalline nanosheets, which further provides active sites for ZnS nucleation and growth.Among the synthesized samples with varying ratios, S-2 (Fe/Zn=7:1) shows better lithium storage properties over other ratios and pure FeS nanosheets in terms of capacity and rate capability. It depicts 9^{th}-cycle specific discharge capacities of 805, 705, 567, 381 and 245 mAh g^{-1} at current densities of 0.1 A g^{-1}, 0.5 A g^{-1}, 1 A g^{-1}, 2 A g^{-1} and 5 A g^{-1}, respectively. The improved lithium storage performance of S-2 can be attributed to: (1) the advantageous hierarchical nanosheets structure provides better stress tolerance for both conversion reaction and alloying reaction upon cycling; (2) each nanosheet are composed of tiny building blocks of FeS and ZnS nanocrystals, which offers shorter diffusion path for charge transport; (3) The coexistence of the heterogeneous sulfides could behave as dispersants of each other. During repeated reversible electrochemical reactions, the heterogeneous metals reduced from the composite sulfides during lithiation are not liable to aggregate, nor are the heterogeneous sulfides formed during delithiation.

5. Novel synthesis of Amorphous FeOOH Nanosheets and Investigation on Its Lithium Storage Kinetics via EIS

5.1 Overview

Recently, nanostructuring has proven to be effective in improving lithium storage capacity, cycling stability and rate capability of electrode materials in LIBs,[171-173] for nanostructuring leads to larger electrode/electrolyte interaction areas, shortened charge transport path, permitting batteries to operate at a higher power density.

Besides of nanostructuring, other approaches, such as forming loosely porous network[174] and compositing with a buffering media (e.g. graphene),[174] are effective in enhancing stress tolerance and in turn improve cycling stability. Amorphization is another effective approach to enhance stress tolerance induced by lithium insertion and extraction. Besides, amorphous materials demonstrate higher capacities because of large quantities of lithium storage at structural defects. In addition, disordered and defected structure can facilitate Li ion transport.[118, 175, 176]

Fe_2O_3, Fe_3O_4 and FeOOH have attracted great interest in various applications because of their eco-friendliness and natural abundance.[177-179] Controlled synthesis of Fe_2O_3 and Fe_3O_4 nanostructures and their applications in LIBs have been intensively investigated.[56, 180, 181] Although the theoretical specific capacity of FeOOH is as high as 903 mAh g^{-1}, there are few reports on FeOOH as LIB anode material. Moreover, lithium storage mechanism and charge transfer kinetics in FeOOH is not fully clear and worth detailed study.

In this work, the combined effects of amorphization and nanostructuring on the lithium storage performance of FeOOH are investigated. Amorphous FeOOH nanosheets are prepared by surfactant-assisted oxidation of self-synthesized FeS nanosheets. The resultant amorphous FeOOH nanosheets are highly porous with a BET surface area of 223 m^2 g^{-1}. And, the amorphous FeOOH based electrode demonstrates excellent rate capabilities. EIS are carried out to further examine the process kinetics of conversion reaction of the amorphous FeOOH as Li storage electrode material. A new equivalent circuit model is proposed capturing the discharging/charging capacitance and resistive components governed by the conversion reaction process. Moreover, a connection has been found between the characteristic frequency of conversion reaction and the inherent hysteresis of discharge/charge voltage profiles.

5.2 Experimental Procedure

5.2.1 Chemical Synthesis

The amorphous FeOOH with porous nanosheets structure was synthesized by oxidation of hierarchical FeS nanosheets by H_2O_2/H_2O solution at room temperature. Synthesis of hierarchical FeS nanosheet has been demonstrated in Section 3.2. In a typical reaction, 44 mg FeS powder is uniformly dispersed in 20 ml toluene. 1 mmol CTAB is dissolved into 20 ml to prepare 50 mM CTAB/H_2O solution, which is then added to the FeS/toluene solution. The mixed solution is vigorously stirred and slightly heated at 40^oC until toluene is completely evaporated. After that, the solution is repeatedly washed by water until complete removal of CTAB. Then, 2 mmol H_2O_2 is added, and stirring is continued at room temperature for 12 hrs. During oxidation, the solution gradually turns from black to orange. The products were then washed with ethanol and dried at 150^oC for 24 hours.

5.2.2 Phase and Morphology Characterization

Morphologies were observed by a FESEM (JEOL JSM-7600F). The HRTEM images were observed using a transmission electron microscope (TEM, JEOL 2010) operating at 200 kV. The crystallinity was examined with a scan speed of 0.5^o/min using X-ray diffractometer (Shimadzu) with Cu Kα irradiation. Fourier Transform Infrared Spectroscopy (FTIR) (Perkin-Elmer) was utilized to identify the types of bonding in the samples. Probe X-ray Photoelectron Spectroscopy (XPS, ESCALab 250iXL and Thetaprobe A1333) was used to verify the valence state of iron and oxygen. Nitrogen

adsorption/desorption isotherms were measured on a Micromeritics Tristar 3000 porosimeter (mesoporous characterization) and Micromeritics ASAP 2020 (microporous characterization) at 77 K. Samples were degassed at 100 °C for 6 h under vacuum before measurement. The specific surface areas were calculated using Brunauer-Emmet-Teller (BET) method.

5.2.3 Battery Assembly and Electrochemical Characterization

70 wt% active materials, 20 wt% single-walled CNT (SWCNT) and 10 wt% Polyacrylonitrile (PAN) were mixed into NMP. The obtained slurry was cast onto a copper foil (diameter: 12mm) and dried in vacuum at 50 °C for 12 h. Electrochemical measurements were carried out on coin-type cells with lithium metal as both counter and reference electrode, Celgard 2400 membrane as the separator, and the electrolyte solution obtained by dissolving 1 M $LiPF_6$ into a mixture of ethylene carbonate (EC) and dimethyl carbonate (DMC) (EC/DMC, 50:50 w/w). The cells were tested on a NEWARE multichannel battery test system with galvanostatic charge and discharge (voltage window of 0.05-3.0V). The EIS measurement is based on a two-electrode coin cell configuration with lithium foil as both the counter electrode and reference electrode. The lithium foil can take in and extract sufficient amount of lithium during charging and discharging process, respectively. Therefore, the influence of changes in the counter electrode, lithium foil, is negligible. The EIS measurements were performed at the OCV at varying states of discharge and charge, with amplitude of 5mV in the frequency range of 10^5 Hz to 0.01Hz.

5.3 Results and Discussion

5.3.1 Phase and Morphology Characterization

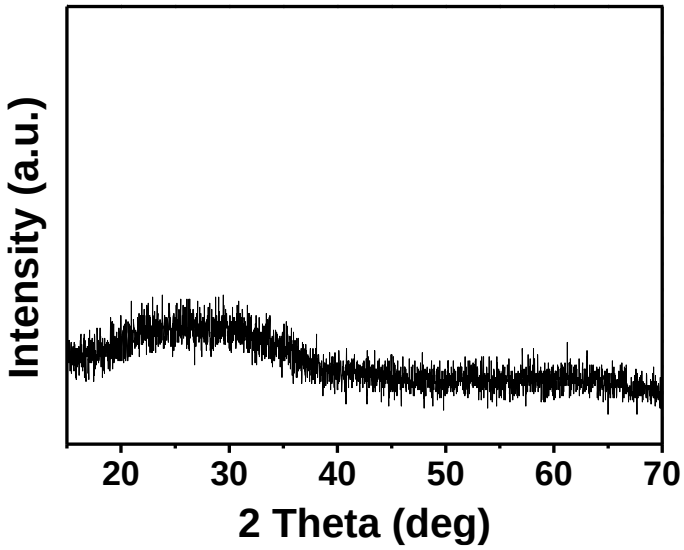

Figure 5-1: XRD pattern of the dried product after oxidation in powder form

After the oxidation process, the powder turns orange in color. The amorphous nature of the synthesized product is revealed by the X-ray diffraction (XRD) pattern (Figure 5-1), which shows a broad hump in the 2θ range of 20^{o}-35^{o} without any characteristic diffraction peaks. In order to know the chemical composition and ensure the completeness of the oxidation process, X-ray photoelectron spectroscopy (XPS) was carried out to find out the oxidation state of Fe and O. The XPS scan profile (Figure 5-2a) of the full range (0-1300eV) reveals the presence of mainly Fe, O and C, indicating the formation of iron oxides or iron Oxyhydroxide.

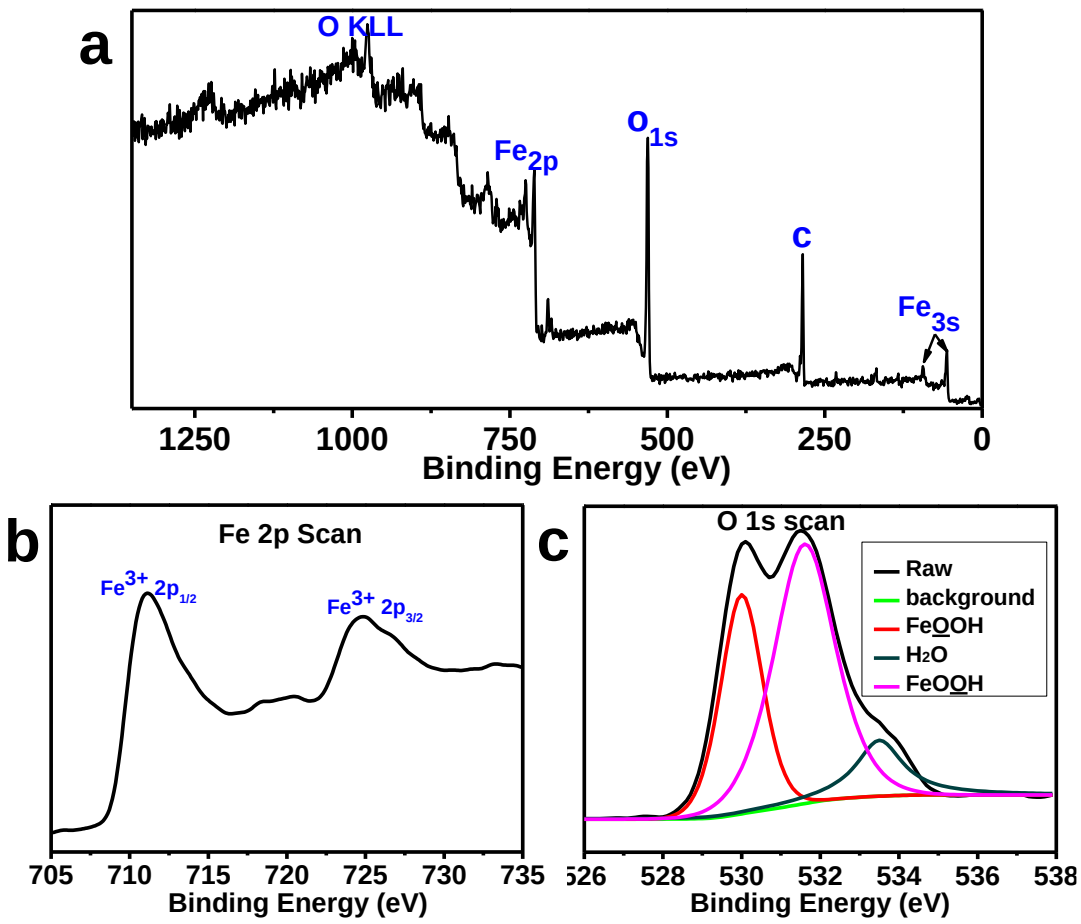

Figure 5-2: (a) XPS spectrum from the amorphous product over the full scan range (BE=0-1300eV). (b) XPS spectrum in the Fe 2p region; (c) XPS spectrum in the O 1s region.

The $2p_{1/2}$ and $2p_{3/2}$ photoelectrons at 711 and 724 eV of the Fe 2p XPS data (Figure 5-2b) correspond to the reported values for Fe^{3+} in Fe_2O_3 or FeOOH,[182, 183] which confirms complete oxidation from Fe^{2+} to Fe^{3+}. The XPS spectrum of oxygen (Figure 5-2c) can be convoluted to three distinct peaks, implying that oxygen presents in three different states. The two convoluted peaks at 530.10 eV and 531.50 eV can be assigned to O^{2-} and OH^- in FeOOH, respectively.[182, 183] The other peak at 533.4eV may be attributed to O in surface-adsorbed water.[183]

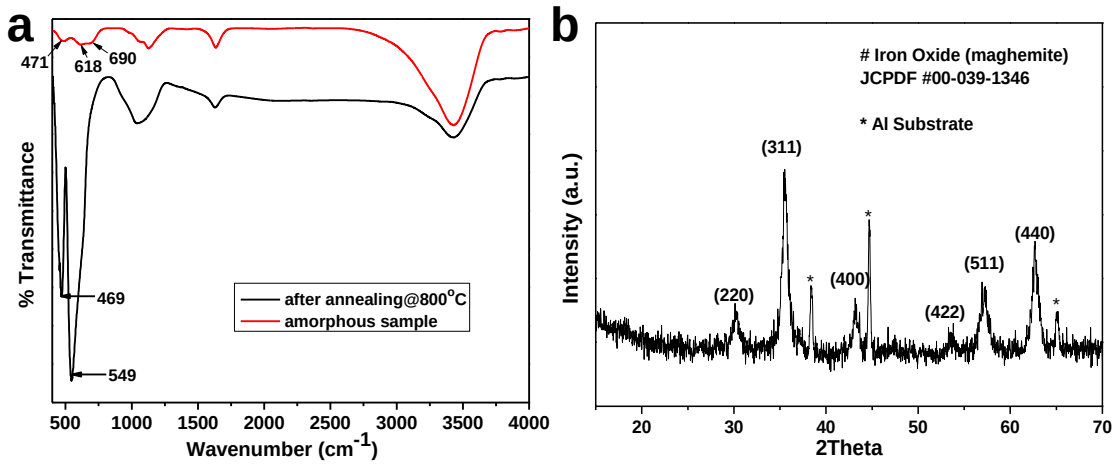

Figure 5-3: (a) FTIR spectrum of the amorphous sample and comparison with its crystalline counterparts. (b) The XRD pattern of the crystalline iron oxide after annealing.

To characterize chemical bonding in this amorphous compound, FTIR was conducted in the wavenumber range of 400-4000 cm^{-1}. Figure 5-3a displays the FTIR spectrum of the amorphous sample and its crystalline counterpart, which is obtained by annealing the amorphous sample at 800°C. The annealed sample is identified to be α-Fe_2O_3 (JCPDF #00-039-1346) by XRD pattern in Figure 5-3b. For both samples, the broad adsorption bands at 3400 cm^{-1} and 1640 cm^{-1} can be ascribed to the stretching vibration of O-H and vibrations of surface-adsorbed H_2O molecules, respectively.[184] The crystalline α-Fe_2O_3 shows evident adsorption bands at 465 cm^{-1} and 549 cm^{-1}, which can be attributed to the bending and stretching of Fe-O bond, respectively,[185] while the amorphous FeOOH shows only weak adsorption band in the characteristic adsorption range of Fe-O bond. The absorption peaks at 471 and 686 cm^{-1} can be assigned to the Fe-O vibrational modes in FeOOH. The Fe-O stretching vibration is responsible for adsorption at ~618 cm^{-1} in FeOOH.[183, 184] Based on the XRD, XPS

and FTIR results above, the synthesized product is identified to be amorphous iron (Fe^{3+}) oxyhydroxide.

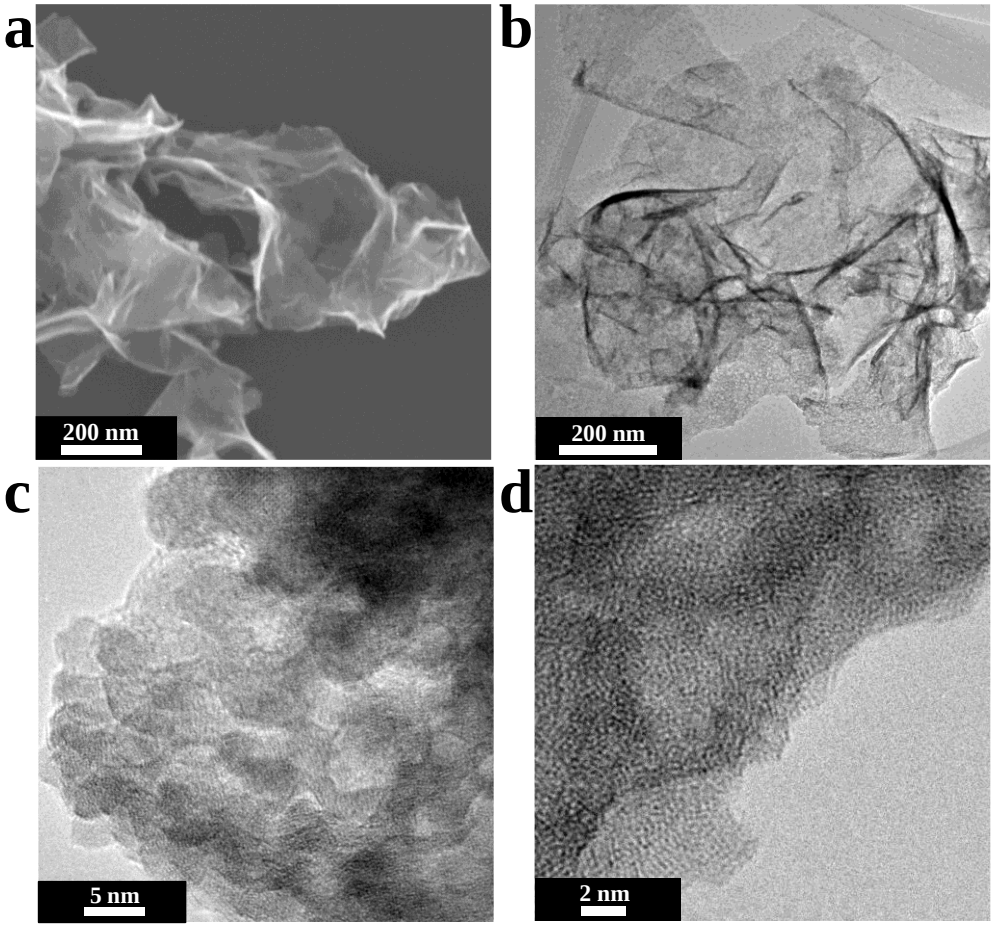

Figure 5-4: (a) SEM image; (b) TEM image; (c) and (d) HRTEM image of the amorphous FeOOH nanosheet.

SEM image (Figure 5-4a) and low-magnification TEM image (Figure 5-4b) of the amorphous product reveals loose and corrugated graphene-like 2D nanosheet structure, indicating no morphology and dimension change from its predecessor, FeS nanosheets.[183]

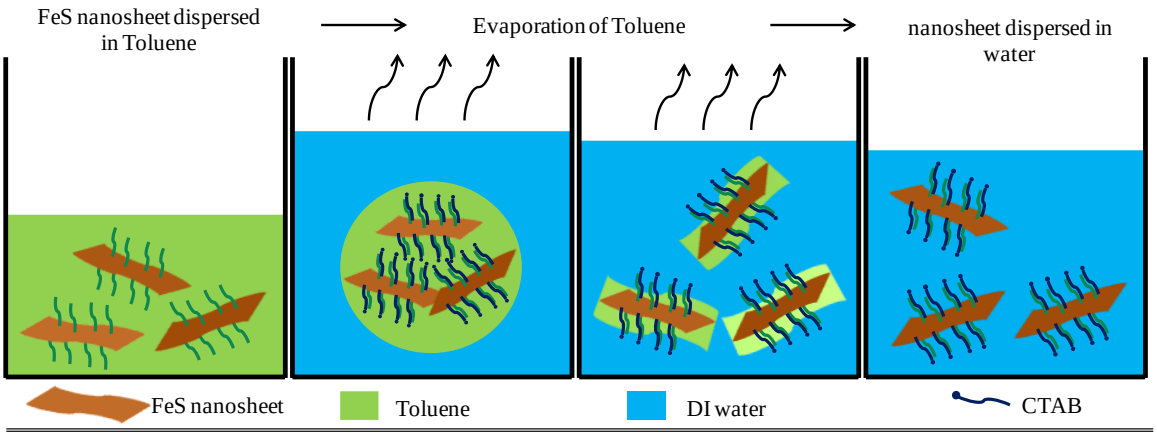

Figure 5-5: Schematic diagram showing how the surfactant, CTAB, facilitate uniform dispersion of FeS nanosheet in water

The sulfide-to-oxide conversion process was conducted in a DI water/Toluene mixture with the assistance of CTAB. The hierarchical FeS nanosheet was previously synthesized in OLA with both OLA and DDT as active surfactants directing the designed nanostructuring. Besides, the FeS nanosheets can be dispersed in Toluene. CTAB is a cationic surfactant with a cationic and hydrophilic "head" and a hydrophobic "tail" referring to the hydrocarbon chain. And, in the DI water/Toluene mixture, with the hydrophobic chain contacting with the surfactant-capped FeS nanosheets while the hydrophilic end directing to water, CTAB facilitate uniform dispersion of toluene droplets wrapping FeS nanosheets in water. After gradual evaporation of toluene, CTAB further enables uniform dispersion of FeS nanosheets in water, and prevents nanosheets' agglomeration during oxidation as illustrated in the schematic diagram (Figure 5-5). As observed from the HRTEM image (Figure 5-4c), individual nanosheet is composed of nanoparticles aggregated in porous form.

Diameters of the fine nanoparticles are smaller than 5 nm. As depicted by the HRTEM image (Figure 5-4d), the atomic lattice on the surface of nanosheets lacks regular periodicity, which further confirms the amorphous nature of the synthesized product.

Nitrogen absorption/desorption measurements of the porous product determined a Brunauer-Emmett-Teller (BET) surface area of 233 m^2 g^{-1} (Figure 5-6), and an average pore size of 3.5 nm The adsorption hysteresis does not show any limiting adsorption at high p/p^o (>0.7), which also implies the presence of slit-shaped pores given by the aggregates of loosely coherent very fine nanoparticles.[186] The highly porous nanostructure and high surface area are attractive for electrochemical applications.

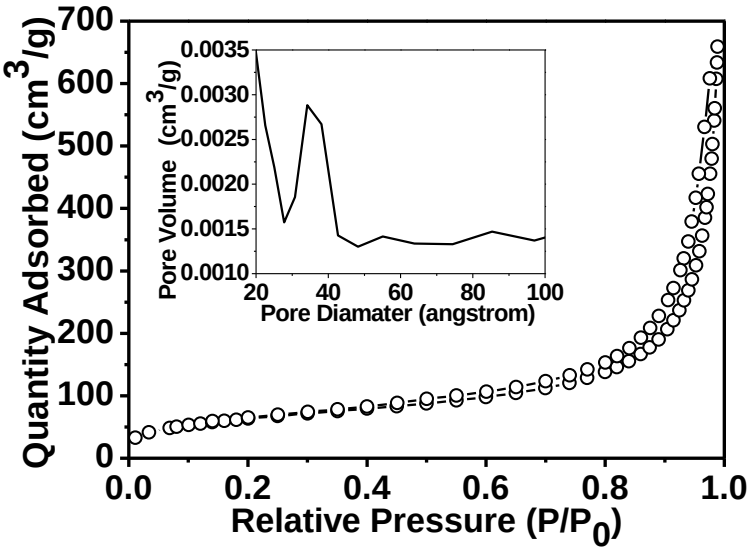

Figure 5-6: N_2 adsorption/desorption isotherm profile and BET pore size distribution plot of the amorphous FeOOH nanosheet

5.3.2 Electrochemical Characterization

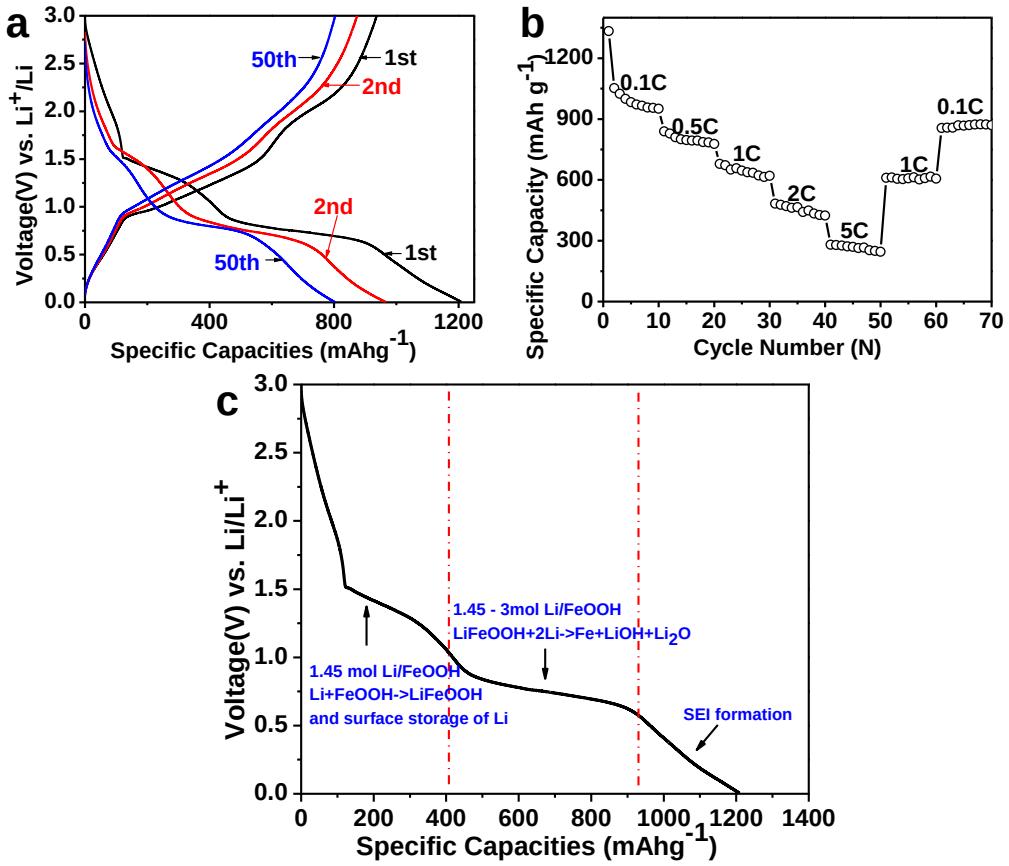

Figure 5-7: (a) Discharge/charge voltage profiles of the 1st, 2nd and 50th cycle; (b) cycling performance at different C-rates; (c) The chemical reactions taking place in different state of discharge.

Figure 5-7a shows the voltage profile of the amorphous FeOOH nanosheet electrode at a current density of 100 mA g^{-1} between 0.05 V and 3.0 V (vs. Li^+/Li) for the 1st, 2nd and 50th discharge/charge cycle. In the 1st cycle discharge, intake of Li^+ involves three distinguishable stages: a shallow slope between 2.8 V and 1.5 V and two voltage plateaus at ~ 1.4 V and 0.75 V, respectively. The specific discharge capacity amounts to 437 mAh g^{-1} when the Amorphous FeOOH electrode is discharged to 0.95V,

corresponding to incorporation of approximately 1.45 mol Li per mol of FeOOH (Figure 5-7c).

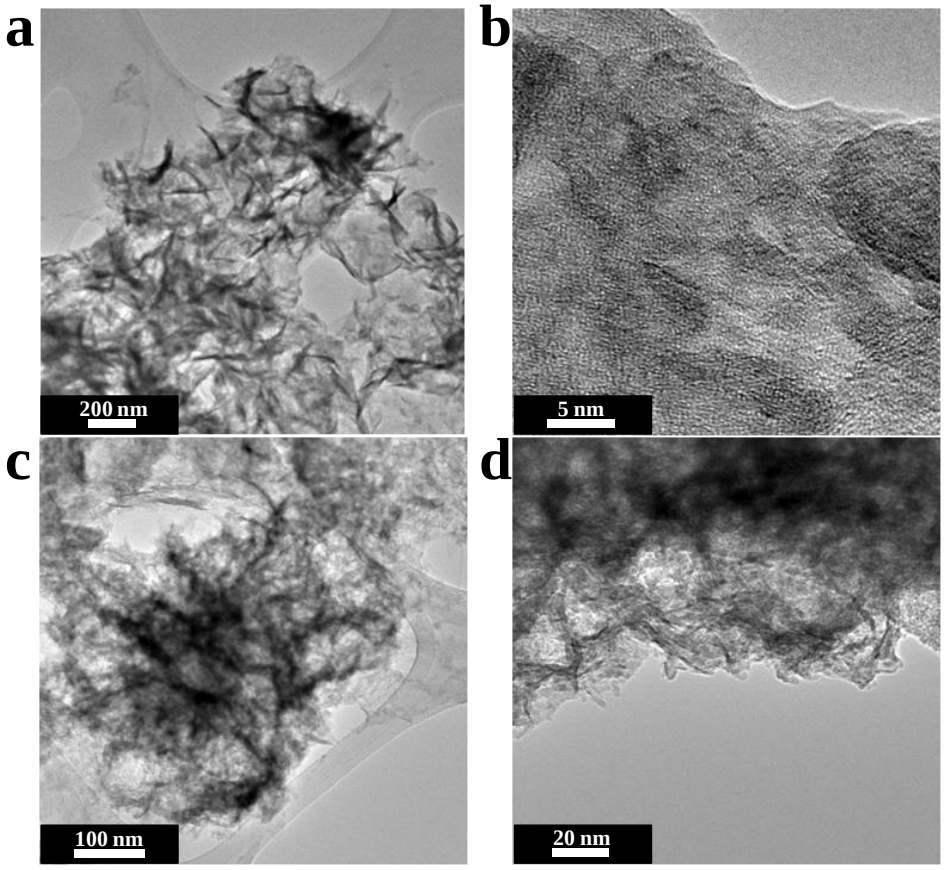

Figure 5-8: (a) TEM and (b)HRTEM images of the discharged active material to 0.95 V; (c) TEM and (d)HRTEM images of the discharged active material to 0.5 V.

Ex-situ examination of the partially lithiated electrode was carried out, and the results are shown in Figure 5-8. The FeOOH electrode sustains its nanosheet morphology and amorphous nature when discharged to 0.95V (Figure 5-8a and 5-8b). It is assumed that the initial two stages of lithiation only involves surface Li storage and insertion of

Li into the loosely-packed amorphous structure.[187] The specific capacity of 914 $mAhg^{-1}$ corresponds to the insertion of approximately 3 mol Li per mol of FeOOH at the discharge potential of 0.5 V, implying complete conversion reaction between Li and FeOOH with the formation of elemental Fe, Li_2O and LiOH.[184, 187]

$$FeOOH + 3Li^+ + 3e^- \rightarrow Fe + Li_2O + LiOH$$

Theoretical discharge capacity of FeOOH is calculated to be 903 mAh g^{-1} according to the conversion reaction shown above. Ex-situ TEM image (Figure 5-8) of the active material at this stage of lithiation shows that the nanosheet network has been partially destroyed. High-magnification TEM observation (Figure 5-8d) reveals formation of fine rod-like nanoparticles. The 1st cycle discharge shows a total specific capacity of 1210 mAh g^{-1}, in which the extra capacity over theoretical capacity can be attributed to SEI formation.[188] The cycling performance of the FeOOH based electrode at varying current densities is plotted in Figure 5-7b, which depicts 5th cycle discharge capacities of 985, 797, 642, 465, and 270 mAh g^{-1} at current densities of 0.1C, 0.5C, 1C, 2C and 5C, respectively (1C = 903 mA g^{-1}). When the current density reverts back to 1C and 0.1C after cycling at 5C, the electrode exhibits discharge capacity of 607 and 870 mAh g^{-1}, respectively. The high porosity and large active surface area contributes to the high capacity of the amorphous FeOOH electrode, but also results in more surface side reactions.[189, 190] The amorphous FeOOH electrode demonstrates higher capacities than crystalline FeOOH at the same current densities.[184, 187, 191, 192] Some research reports proposed that the improved rate capability of amorphous electrode material results from more effective Li^+ transport facilitated by large quantities of structural defects.[176, 193] However, for conversion-reaction type

electrode materials, both conversion reaction kinetics and diffusion kinetics of Li^+ play important roles in electrode rate capabilities. Therefore, it is crucial to include the conversion reaction kinetics in discussing the rate capability of conversion reaction type lithium storage electrode materials.

5.3.3 EIS Analysis

Nyquist plots derived from impedance measurement combining proposed equivalent circuits are usually employed in analyzing process kinetics of electrodes in LIBs.[194] Nyquist plots of the EIS measurement of amorphous FeOOH nanosheet electrode at different states of discharge (SOD) and states of charge (SOC) during its 5^{th} cycle are shown in Figure 5-9a and 5-9b, respectively. The initial few cycles of conversion reaction is highly irreversible and involves a lot of surface side reactions, so the 5^{th} cycle is selected for analysis because the conversion reaction are expected to be reversible afterwards.

In recent research, EIS has been rigorously applied in explaining intercalation reactions to estimate charge transfer resistance and the diffusion coefficient of Li^+ in intercalation-type electrode materials.[195, 196] The model used to explain conversion reaction in literature is based on a well-known two-state model that has been often used in describing intercalation systems, and it is rather crude for the present system with phase segregations.

In the following discussion, a new equivalent circuit modeling the conversion reaction mechanism will be derived. First of all, let us simplify the conversion reaction as:

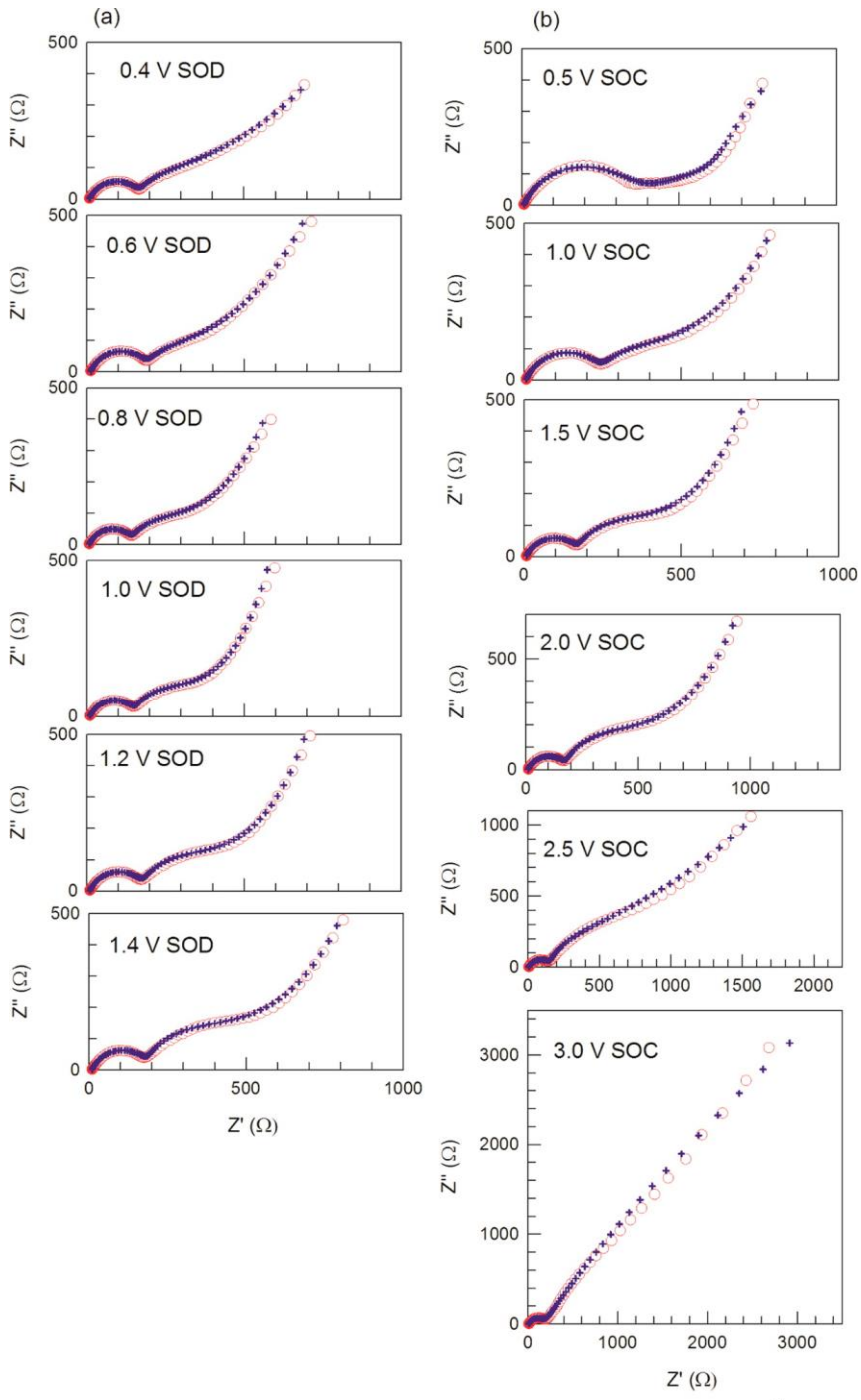

Figure 5-9: Nyquist plots obtained from EIS measurement at different voltage (vs. Li^+/Li) corresponding either to (a) different state of discharge (SOD) or (b) different state of charge (SOC). Experimental data (dot) and fits (cross) are displayed for comparison.

$$Li^+ + MX + e^- \rightarrow M + LiX$$

(M denotes transition metal, and X= X = O, S, F, OH, etc. The stoichiometry is neglected for simplicity.)

Conversion reaction usually proceeds in mainly two stages. [197, 198] During the 1st stage, Li^+ insert into the MX lattice with a marked step of the voltage. Thereafter the real conversion reaction proceeds producing phase segregation.

In order to obtain a physical interpretation for the results of the EIS results in Figure 5-9, we outline here a simple model incorporating two stages.[199-202] As inferred by the fitted Nyquist plots in Figure 5-9, the kinetics of the charge/discharge process is dominated by the resistive contribution arising from the medium frequency spectrum. For intercalation compounds, the rate-limiting step is the diffusion of Li^+ in the active material and the medium-frequency resistance arises from Li^+ transport before reaching their stable sites within the matrix. Diffusion of ions gives rise to distinctive impedance patterns characterized by Warburg-like responses as $Z \propto (i\omega)^{-1/2}$ (where ω is the angular frequency, and $i = \sqrt{-1}$). However, the amorphous FeOOH electrodes studied in this work function by conversion reactions that entail an overall material rearrangement in both chemical and structural nature. These factors lead us to consider extra capacitance and resistance caused by new phase and new interface formation during the conversion reaction. The corresponding resistive element is then labeled as conversion-reaction resistance R_{cr} , and is connected in series with

introduced chemical capacitance C_μ^c which informs on the varying concentration c of reacted Li^+ upon application of change in the chemical potential μ.[203]

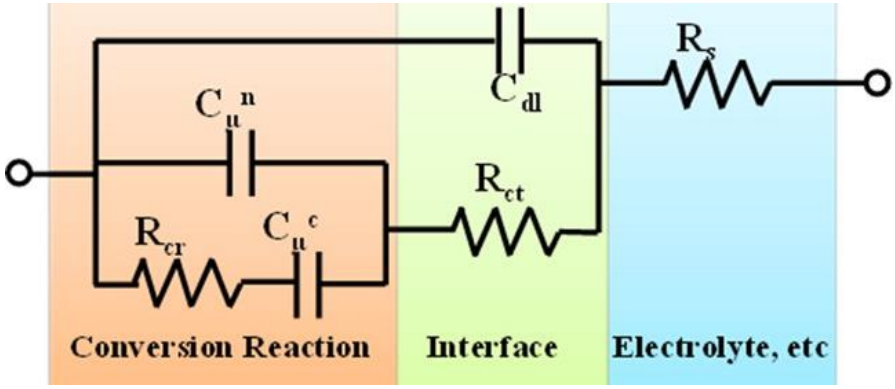

Figure 5-10: the proposed equivalent circuit modeling the conversion reaction

An equivalent circuit model accounting for the impedance of conversion reaction is shown in Figure 5-10. This equivalent circuit produces an excellent fit for the Nyquist plots in Figure 5-9, for both the discharge and charge polarization regimes.

According to the new equivalent circuit model, the circuit impedance can be divided into three parts: the series resistanceR_s, interface impedance (including charge transfer resistance R_{ct} and double-layer capacitance C_{dl} at the interface) and conversion reaction impedance (including conversion reaction capacitance C_μ^c, conversion reaction R_{cr} and chemical capacitance corresponding to the inserted but non-reacted Li^+ C_μ^n).

At high frequencies, a rather constant arc corresponds to the parallel connection between the double layer capacitance $C_{dl} \approx 45\mu F$ and surface charge transfer resistance $R_{ct} \approx 200\Omega$.

As explained in details in Appendix, the conversion reaction during the discharge and charge process can be modeled as a series RC circuit. The combination of C_{μ}^{c}, R_{cr}, and C_{μ}^{n} forms a sort of relaxation subcircuit which is interpreted here in terms of the conversion reaction mechanism. [204]

The conversion-reaction time scale can be calculated by $C_{\mu}^{c}\ R_{cr}$. The larger the time constant, the longer time is required for discharging or charging to the target voltage. And, the reciprocal corresponds to the response frequency

$$\omega_{cr} = \frac{1}{R_{cr} C_{\mu}^{c}}$$

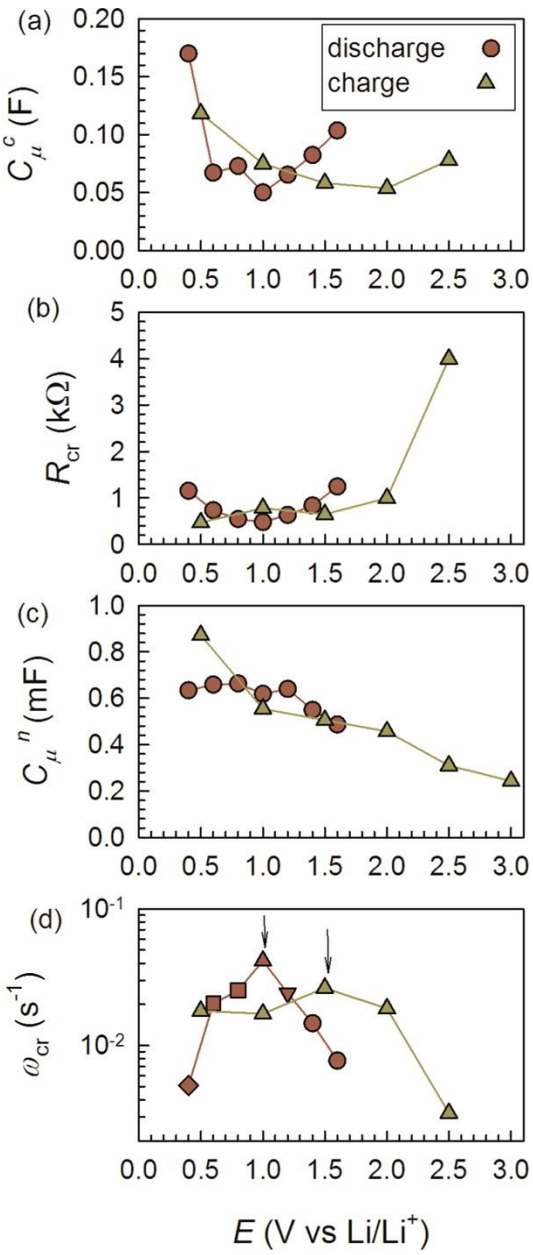

Figure 5-11: Parameters at different SOD and SOC extracted from fitting using the equivalent circuit in Figure 5-10. (a) Chemical capacitance; (b) Conversion-reaction resistance; and (c) Chemical capacitance corresponding to extent of lithium insertion/extraction; (d) Conversion-reaction response frequency.

The electrical parameters at different SOD and SOC have also been calculated from fitting and displayed in Figure 5-11. It is observed that C_μ^c exhibits a high value in the order of 0.1 F (Figure 5-11a). During the discharge process, C_μ^c shows slight variations between 0.05 F and 0.1 F, and exhibits a small peak at ~ 0.7 V, which is in good correlation with the discharge plateau of voltage profile in Figure 5-7a. This observation confirms that the proposed conversion reaction subcircuit (series RC) can reproduce the hysteresis in the voltage profile and is viable for modeling the conversion reaction. The conversion reaction resistance R_{cr} demonstrates similar trends as C_μ^c (Figure 5-11b), but R_{cr} exhibits a rather high value for higher voltages (> 2.0V), which entailing that the conversion reaction is hindered at high states of charge. An averaged value $R_{cr} \approx 500\Omega$ is encountered, which is greater than R_{ct},. The high reaction resistance indicates that the conversion reaction rate primarily limits the overall discharge/charge process kinetics. From Figure 5-11c, it is observed that the chemical capacitance C_μ^n directly relating to concentration of intercalated but non-reacted Li^+ have values two orders smaller than that of C_μ^c.

The conversion reaction kinetics can be alternatively accessed by examining the response frequency. Values of ω_{cr} below 0.04 s^{-1} are found. One can observe that ω_{cr} exhibits a maximum locating within the potential interval of the major conversion reaction ($FeOOH + 3Li^+ + 3e^- \rightarrow Fe + Li_2O + LiOH$) according to the discharge voltage profile (Figure 5-7a). We notice that a voltage shift of ~0.5 V in ω_{cr} occurs between discharge and charge regimes, which pointing to the hysteretic behavior of

the conversion reaction.[35, 205] Here, we highlight that EIS analysis reproduces the hysteresis observed between charge and discharge profiles (Figure 5-7a) and CV curves (Figure 5-7c). The series RC subcircuit in parallel with the chemical capacitance is valid in modeling this conversion reaction, and the parameters extracted implies that the conversion reaction rate limits overall process kinetics.

5.4 Conclusions

In summary, amorphous FeOOH nanosheet has been synthesized via surfactant-assistant oxidation of hierarchical FeS nanosheet. The surfactant, CTAB, does not only aids in transferring the FeS nanosheet from organic solvent to water, but also prevents nanosheet from agglomerating in the multi-step operations. The high surface area, porous nanostructure and loose amorphous nature of the FeOOH nanosheet are attractive for electrochemical energy storage applications. In the lithium storage application, it has conversion reaction with Li^+ and demonstrates improved specific capacity and rate capability (e.g. discharge capacity as high as 465 $mAhg^{-1}$ at a current density of 2C) compared to its crystalline counterparts.

A new and detailed equivalent circuit including a series series RC subcircuit in parallel with the chemical capacitance directly modeling conversion reaction is proposed to model the overall electrode lithiation and de-lithiation process. The proposed model can be perfectly fitted with the Nyquist plots from experimental EIS measurement and can reproduce the hysteresis in the discharge/charge voltage profile, indicating the validity of this new equivalent circuit in analyzing the lithiation/de-lithiation process kinetics of conversion reaction electrodes. The parameters extracted after Nyquist plot fitting also implies that the process kinetics of lithiation/de-lithiation of conversion reaction electrode is limited by reaction itself with a thermodynamic origin rather than being limited by Li transport.

6. Conclusion and Recommendations for Future Work

6.1 Conclusions

In this thesis, this work has focuses on rational design and development of facile and scalable solution based approaches for synthesis of advanced two-dimensional nanostructured iron-based compounds with varying morphology architecture, compositions and crystallinity. And, detailed investigation of the effects of nanostructuring architectures, compositing and amorphization on lithium storage performance of those iron-based compound electrodes was carried out.

Hierarchical FeS nanosheet, Hierarchical FeS/ZnS compositing nanosheets and amorphous FeOOH nanosheet has been synthesized and their lithium storage performance has been intensively investigated. The following conclusions can be drawn from these works:

Firstly, with the templating effect of dodecane-thiolate, hierarchical carbon coated FeS nanosheets can be fabricated in solution. The resultant nanosheets are constructed by FeS nanocrystals of smaller than 5 nm, implying that the formation of nanosheet is not related to the crystal structure of Troilite-phase FeS and is more related to the templating effect, which also implies that this synthesis approach towards nanosheet formation may be extendable to other transition metal sulfides. The carbon coated hierarchical FeS nanosheets deliver promising lithium storage capacity, cycling stability and rate capabilities, and the good lithium storage property can be attributed to: (1) the hierarchical construction can effectively accommodate large volume change

induced during repeated charge/discharge; (2) the fine building blocks of the hierarchical structure offers shorter charge transport paths and allows faster charge transfer, and the interconnected nano-building blocks helps sustain structural integrity and provide continuous path for electronic transport; (3) the in-situ formed amorphous carbon coating can prevent the polysulfides generated during conversion reaction of sulfides from dissolving in to the electrolyte, and thus sustaining the ionic conductivity of the electrolyte.

Next, carbon coated FeS/ZnS compositing hierarchical nanosheets have been prepared follow the same synthesis steps. The compositional ratio of FeS and ZnS can be varied by manipulating the compositional ratios in precursor, and FeS is more preferably formed than ZnS. It is concluded that FeS nanocrystals grow with template to nanosheet, which further provides active sites for nucleation and growth of ZnS nanocrystals. Among samples with varying compositional ratios, S-2 ((Fe/Zn=7:1) shows best lithium storage properties over other ratios and pure FeS nanosheets in terms of capacity and rate capability. The improved lithium storage performance of the compositing hierarchical nanosheet can be ascribed to: (1) advantageous hierarchical construction offers better stress tolerance of involving conversion and alloying reaction; (2) interconnected and fine nano-building blocks of FeS and ZnS nanocrystals facilitate faster and continuous charge transport; (3) the coexistence of the heterogeneous sulfides could behave as dispersants of each other, so that neither the heterogeneous metals reduced from the composite sulfides during lithiation nor the heterogeneous sulfides formed during delihtiation are liable to aggregate.

Finally, amorphous FeOOH nanosheet has been synthesized via surfactant-assisted oxidation of self-synthesized FeS nanosheet. The obtained amorphous FeOOH nanosheet possesses high surface area, porous nanostructure and is structurally loose in nature, which are attractive for lithium storage application. The amorphous FeOOH has conversion reaction with lithium ions and demonstrate high lithium storage capacity and superior rate capability. A new equivalent circuit modeling the complete conversion reaction process was proposed and can be perfectly fitting with the Nyquist plots from EIS analysis. A series RC sub-circuit is used to directly model the conversion reaction. Further investigations on the parameters (eg. the time constant of conversion reaction) generated from the fitting of the Nyquist plots found that the trend of parameters reproduces the hysteresis in the discharge/charge voltage profile, indicating that the conversion reaction between FeOOH and lithium ions has a thermodynamic origin.

The findings summarized above highlight new routes for synthesis of hierarchical nanostructure, compositing nanostructure and amorphous nanostructure, and enhance the understanding of hierarchical construction, compositing and amorphization effects of nanostructures on their lithium storage performance.

6.2 Future Works

6.2.1 Synthesis of hierarchical nanostructured composite with two or more components

It has been concluded that formation of hierarchical FeS nanosheet is more relevant to the colloidal soft templating effect but less relevant to the crystal lattice nature of material itself. Therefore, it is possible to extend this synthesis strategy to other metal sulfides, especially transition metal monosulfide, such as CuS, CdS, MnS, NiS and CoS. And energy conversion and energy storage performance of these metal sulfides with hierarchical nanostructuring are interesting and worth further investigation.

It has been demonstrated in Section 4 that hierarchical composite nanosheet of two active components with uniform dispersion can be obtained. Thus, it might be possible to extend this synthesis strategy to composite metal sulfides with two active components or more. For example, ZnS/CuS/CdS composite is attractive for hydrogen production in solar water splitting. In order to optimize the synergistic effect, each component is expected to keep their own phase with optimized CuS and CdS contents. [206] By extending this synthetic strategy, ZnS/CuS/CdS nanoparticle-constituent hierarchical structure can be synthesized with controllable CuS and CdS contents, which are expected to demonstrate improved photocatalytic effects than single component in hydrogen evolution process.

6.2.2 Amorphous lithium storage electrode materials

Amorphous materials are seldom investigated as lithium storage electrode materials until researchers found amorphous materials usually demonstrate higher capacity than their crystalline counterparts in intercalation reactions. It is proposed that the disordered state of amorphous material facilitates faster Li^+ diffusion inside the electrode framework, which entails higher capacity even at higher current densities.

However, for conversion reaction electrode materials, the disordered structure may retard decomposition and thus the rate of conversion reaction. Therefore, it is desired to synthesis both amorphous and crystalline electrode materials with identical nanostructure and composition in order to exclude the varying effect of morphology and composition on overall lithiation kinetics. Through complete electrochemical characterization, including CV curve, rate capability, EIS analysis and ex-situ observation after cycling to investigate the effect of amorphization on conversion reaction rate, charge transfer rate and charge transport rate in the overall lithiation/de-lithiation process.

In addition, amorphous materials have more open lattice, so they are expected to intercalate Li^+ over a wider voltage range. It might be an interesting attempt to test some amorphous anode materials in the voltage range of cathode materials. For example, amorphous FeOOH nanosheet based electrode synthesized in this work shows capacity when tested in the voltage window of 3 V~4.5 V (vs. Li^+/Li).

7. References

1. *Energy Storage Program Planning Document* S.E.I.A.B.o.U. DOE, Editor 2011.

2. David Linden, T.B.R., *Handbook of Batteries* 2001, McGraw Hill Professional.

3. Yoo, H.D., et al., *On the challenge of developing advanced technologies for electrochemical energy storage and conversion.* Materials Today, 2014. 17(3): p. 110-121.

4. Tarascon, J.-M. and M. Armand, *Issues and challenges facing rechargeable lithium batteries.* Nature, 2001. 414(6861).

5. Besenhard, J.O. and R. Schöllhorn, *The discharge reaction mechanism of the MoO3 electrode in organic electrolytes.* Journal of Power Sources, 1976. 1(3): p. 267-276.

6. Besenhard, J.O., *The electrochemical preparation and properties of ionic alkali metal-and NR4-graphite intercalation compounds in organic electrolytes.* Carbon, 1976. 14(2): p. 111-115.

7. AKIRA, Y., *Secondary battery* 1985, Asahi Kasei: Japan.

8. Scrosati, B., *Nanomaterials: Paper powers battery breakthrough.* Nat Nano, 2007. 2(10).

9. Yoshio, M., T. Tsumura, and N. Dimov, *Electrochemical behaviors of silicon based anode material.* Journal of Power Sources, 2005. 146(1–2): p. 10-14.

10. Kasavajjula, U., C. Wang, and A.J. Appleby, *Nano- and bulk-silicon-based insertion anodes for lithium-ion secondary cells.* Journal of Power Sources, 2007. 163(2): p. 1003-1039.

11. Laubach, S., et al., *Changes in the crystal and electronic structure of LiCoO2 and LiNiO2 upon Li intercalation and de-intercalation.* Physical Chemistry Chemical Physics, 2009. 11(17): p. 3278-3289.

12. Liu, F., et al., *Selective crystallization with preferred lithium-ion storage capability of inorganic materials.* Nanoscale Research Letters, 2012. 7(1): p. 149.

13. Wang, Y., et al., *Nanostructured Vanadium Oxide Electrodes for Enhanced Lithium-Ion Intercalation.* Advanced Functional Materials, 2006. 16(9): p. 1133-1144.

14. Lee, S.-Y., et al., *Performance and thermal stability of LiCoO2 cathode modified with ionic liquid.* Journal of Power Sources, 2005. 146(1–2): p. 732-735.

15. Ellis, B.L., et al., *A multifunctional 3.5[thinsp]V iron-based phosphate cathode for rechargeable batteries.* Nat Mater, 2007. 6(10).

16. Bak, S.-M., et al., *Spinel LiMn2O4/reduced graphene oxide hybrid for high rate lithium ion batteries.* Journal of Materials Chemistry, 2011. 21(43): p. 17309-17315.

17. Wu, Y., et al., *Hollow Porous LiMn2O4 Microcubes as Rechargeable Lithium Battery Cathode with High Electrochemical Performance.* Small, 2012. 8(6): p. 858-862.

18. Talyosef, Y., et al., *Comparing the Behavior of Nano- and Microsized Particles of LiMn1.5Ni0.5O4 Spinel as Cathode Materials for Li-Ion Batteries.* Journal of The Electrochemical Society, 2007. 154(7): p. A682-A691.

19. Sun, Y., et al., *Synthesis of high power type LiMn1.5Ni0.5O4 by optimizing its preparation conditions.* Journal of Power Sources, 2010. 195(13): p. 4322-4326.

20. Amalraj, F., et al., *Synthesis of Integrated Cathode Materials* $xLi2MnO3\cdot(1-x)LiMn1/3Ni1/3Co1/3O2$ $(x=0.3,\ 0.5,\ 0.7)$ *and Studies of Their Electrochemical Behavior.* Journal of The Electrochemical Society, 2010. 157(10): p. A1121-A1130.

21. Lim, J.-H., et al., *Electrochemical characterization of Li2MnO3–Li[Ni1/3Co1/3Mn1/3]O2–LiNiO2 cathode synthesized via co-precipitation for lithium secondary batteries.* Journal of Power Sources, 2009. 189(1): p. 571-575.

22. Thackeray, M.M., et al., *Advances in manganese-oxide 'composite' electrodes for lithium-ion batteries.* Journal of Materials Chemistry, 2005. 15(23): p. 2257-2267.

23. Yuan, L.-X., et al., *Development and challenges of LiFePO4 cathode material for lithium-ion batteries.* Energy & Environmental Science, 2011. 4(2): p. 269-284.

24. Park, M., et al., *A review of conduction phenomena in Li-ion batteries.* Journal of Power Sources, 2010. 195(24): p. 7904-7929.

25. Doan, T.N.L. and I. Taniguchi, *Preparation of LiCoPO4/C nanocomposite cathode of lithium batteries with high rate performance.* Journal of Power Sources, 2011. 196(13): p. 5679-5684.

26. Bramnik, N.N. and H. Ehrenberg, *Precursor-based synthesis and electrochemical performance of LiMnPO4.* Journal of Alloys and Compounds, 2008. 464(1–2): p. 259-264.

27. Liu, H., et al., *An ordered mesoporous WS2 anode material with superior electrochemical performance for lithium ion batteries.* Journal of Materials Chemistry, 2012. 22(34): p. 17437-17440.

28. Xu, X., et al., *Fabrication of MoS2 nanosheet@TiO2 nanotube hybrid nanostructures for lithium storage.* Nanoscale, 2014. 6(10): p. 5245-5250.

29. Chiu, H.-c. and G.P. Demopoulos, *A Novel Green Approach to Synthesis of Nanostructured Li4Ti5O12 Anode Material.* ECS Transactions, 2013. 50(26): p. 119-126.

30. Persson, K., et al., *Lithium Diffusion in Graphitic Carbon.* The Journal of Physical Chemistry Letters, 2010. 1(8): p. 1176-1180.

31. Dey, A.N., J. Electrochem. Soc., 1971. 118: p. 1547.

32. Grugeon, S., Solid State Sci., 2003. 5: p. 895.

33. Timmons, A., J. Electrochem. Soc., 2006. 153: p. A1206.

34. Shao, J., et al., *Low-Cost Synthesis of Hierarchical V2O5 Microspheres as High-Performance Cathode for Lithium-Ion Batteries.* ACS Applied Materials & Interfaces, 2013. 5(16): p. 7671-7675.

35. Cabana, J., et al., *Beyond Intercalation-Based Li-Ion Batteries: The State of the Art and Challenges of Electrode Materials Reacting Through Conversion Reactions.* Advanced Materials, 2010. 22(35): p. E170-E192.

36. Poizot, P., et al., *Nano-sized transition-metal oxides as negative-electrode materials for lithium-ion batteries.* Nature, 2000. 407(6803).

37. Débart, A., et al., *A Transmission Electron Microscopy Study of the Reactivity Mechanism of Tailor-Made CuO Particles toward Lithium.* Journal of The Electrochemical Society, 2001. 148(11): p. A1266-A1274.

38. Alcántara, R., et al., *Changes in oxidation state and magnetic order of iron atoms during the electrochemical reaction of lithium with NiFe2O4.* Electrochemistry Communications, 2003. 5(1): p. 16-21.

39. Larcher, D., et al., *Combined XRD, EXAFS, and Mössbauer Studies of the Reduction by Lithium of α-Fe2O3 with Various Particle Sizes.* Journal of The Electrochemical Society, 2003. 150(12): p. A1643-A1650.

40. Delmer, O., et al., *Enhanced Potential of Amorphous Electrode Materials: Case Study of RuO2.* Advanced Materials, 2008. 20(3): p. 501-505.

41. Grugeon, S., et al., *An update on the reactivity of nanoparticles Co-based compounds towards Li.* Solid State Sciences, 2003. 5(6): p. 895-904.

42. Balaya, P., et al., *Fully Reversible Homogeneous and Heterogeneous Li Storage in RuO2 with High Capacity.* Advanced Functional Materials, 2003. 13(8): p. 621-625.

43. Bekaert, E., et al., *6Li MAS NMR Investigation of Electrochemical Lithiation of RuO2: Evidence for an Interfacial Storage Mechanism.* Chemistry of Materials, 2009. 21(5): p. 856-861.

44. Bruce, P.G., B. Scrosati, and J.-M. Tarascon, *Nanomaterials for Rechargeable Lithium Batteries.* Angewandte Chemie International Edition, 2008. 47(16): p. 2930-2946.

45. Cheng, F., et al., *Functional Materials for Rechargeable Batteries.* Advanced Materials, 2011. 23(15): p. 1695-1715.

46. Zhang, L., H.B. Wu, and X.W. Lou, *Iron-Oxide-Based Advanced Anode Materials for Lithium-Ion Batteries.* Advanced Energy Materials, 2014. 4(4): p. n/a-n/a.

47. Poizot, P., et al., *Nano-sized transition-metal oxides as negative-electrode materials for lithium-ion batteries.* Nature, 2000. 407(6803).

48. Henriksen;, G.L. and A.N. Jansen, *Handbook of batteries*, ed. T.B.R. D.Linden2002, New York McGraw-Hill.

49. Kaun, T.D., et al., *High temperature lithium/sulfide batteries.* Electrochimica Acta, 1993. 38(9): p. 1269-1287.

50. Yamin, H. and E. Peled, *Electrochemistry of a nonaqueous lithium/sulfur cell.* Journal of Power Sources, 1983. 9(3): p. 281-287.

51. Mikhaylik, Y.V. and J.R. Akridge, *Polysulfide Shuttle Study in the Li/S Battery System.* Journal of The Electrochemical Society, 2004. 151(11): p. A1969-A1976.

52. Masset, P.J. and R.A. Guidotti, *Thermal activated ("thermal") battery technology: Part IIIa: FeS2 cathode material.* Journal of Power Sources, 2008. 177(2): p. 595-609.

53. Guo, Y.-G., J.-S. Hu, and L.-J. Wan, *Nanostructured Materials for Electrochemical Energy Conversion and Storage Devices.* Advanced Materials, 2008. 20(15): p. 2878-2887.

54. Cabana, J., et al., *Beyond Intercalation-Based Li-Ion Batteries: The State of the Art and Challenges of Electrode Materials Reacting Through Conversion Reactions.* Advanced Materials, 2010. 22(35): p. 170-192.

55. Lowe, M.A., J. Gao, and H.D. Abruna, *In operando X-ray studies of the conversion reaction in Mn3O4 lithium battery anodes.* Journal of Materials Chemistry A, 2013. 1(6): p. 2094-2103.

56. Reddy, M.V., et al., *α-Fe2O3 Nanoflakes as an Anode Material for Li-Ion Batteries.* Advanced Functional Materials, 2007. 17(15): p. 2792-2799.

57. Ji, L., et al., *Recent developments in nanostructured anode materials for rechargeable lithium-ion batteries.* Energy & Environmental Science, 2011. 4(8): p. 2682-2699.

58. Arico, A.S., et al., *Nanostructured materials for advanced energy conversion and storage devices.* Nat Mater, 2005. 4(5).

59. Liu, J. and X.-W. Liu, *Two-Dimensional Nanoarchitectures for Lithium Storage.* Advanced Materials, 2012. 24(30): p. 4097-4111.

60. Shin, J.-Y., D. Samuelis, and J. Maier, *Sustained Lithium-Storage Performance of Hierarchical, Nanoporous Anatase TiO2 at High Rates: Emphasis on Interfacial Storage Phenomena.* Advanced Functional Materials, 2011. 21(18): p. 3464-3472.

61. Choi, M., et al., *Stable single-unit-cell nanosheets of zeolite MFI as active and long-lived catalysts.* Nature, 2009. 461(7261).

62. Geim, A.K., *Graphene: Status and Prospects.* Science, 2009. 324(5934): p. 1530-1534.

63. Wang, G., et al., *Sn/graphene nanocomposite with 3D architecture for enhanced reversible lithium storage in lithium ion batteries.* Journal of Materials Chemistry, 2009. 19(44): p. 8378-8384.

64. Liu, D., et al., *Ultrathin nanoporous Fe3O4-carbon nanosheets with enhanced supercapacitor performance.* Journal of Materials Chemistry A, 2013. 1(6): p. 1952-1955.

65. Wang, Q.H., et al., *Electronics and optoelectronics of two-dimensional transition metal dichalcogenides.* Nat Nano, 2012. 7(11).

66. Liu, K.-K., et al., *Growth of Large-Area and Highly Crystalline MoS2 Thin Layers on Insulating Substrates.* Nano Letters, 2012. 12(3): p. 1538-1544.

67. Lee, Y.-H., et al., *Synthesis of Large-Area MoS2 Atomic Layers with Chemical Vapor Deposition.* Advanced Materials, 2012. 24(17): p. 2320-2325.

68. Zhan, Y., et al., *Large-Area Vapor-Phase Growth and Characterization of MoS2 Atomic Layers on a SiO2 Substrate.* Small, 2012. 8(7): p. 966-971.

69. Cunningham, G., et al., *Solvent Exfoliation of Transition Metal Dichalcogenides: Dispersibility of Exfoliated Nanosheets Varies Only Weakly between Compounds.* ACS Nano, 2012. 6(4): p. 3468-3480.

70. Benavente, E., et al., *Intercalation chemistry of molybdenum disulfide.* Coordination Chemistry Reviews, 2002. 224(1–2): p. 87-109.

71. Joensen, P., R.F. Frindt, and S.R. Morrison, *Single-layer MoS2.* Materials Research Bulletin, 1986. 21(4): p. 457-461.

72. Eda, G., et al., *Photoluminescence from Chemically Exfoliated MoS2.* Nano Letters, 2011. 11(12): p. 5111-5116.

73. Eda, G., et al., *Coherent Atomic and Electronic Heterostructures of Single-Layer MoS2.* ACS Nano, 2012. 6(8): p. 7311-7317.

74. Zeng, Z., et al., *Single-Layer Semiconducting Nanosheets: High-Yield Preparation and Device Fabrication.* Angewandte Chemie International Edition, 2011. 50(47): p. 11093-11097.

75. Lukowski, M.A., et al., *Enhanced Hydrogen Evolution Catalysis from Chemically Exfoliated Metallic MoS2 Nanosheets.* Journal of the American Chemical Society, 2013. 135(28): p. 10274-10277.

76. Rui, X., et al., *Ultrathin V2O5 nanosheet cathodes: realizing ultrafast reversible lithium storage.* Nanoscale, 2013. 5(2): p. 556-560.

77. Geim, A.K. and I.V. Grigorieva, *Van der Waals heterostructures.* Nature, 2013. 499(7459).

78. Liang, H., et al., *Controlled synthesis of Co3O4 nanopolyhedrons and nanosheets at low temperature.* Chemical Communications, 2009(48): p. 7569-7571.

79. Du, Y., et al., *A general method for the large-scale synthesis of uniform ultrathin metal sulphide nanocrystals.* Nat Commun, 2012. 3.

80. Zhuang;, Q.-C., et al., eds. *Lithium Ion Batteries - New Developments*. Diagnosis of Electrochemical Impedance Spectroscopy in Lithium-Ion Batteries, ed. D.I. Belharouak2012, InTech.

81. Wang, X., et al., *TiO2 modified FeS Nanostructures with Enhanced Electrochemical Performance for Lithium-Ion Batteries.* Sci. Rep., 2013. 3.

82. Xie, J., et al., *One-pot synthesis of ultrafine ZnFe2O4 nanocrystals anchored on graphene for high-performance Li and Li-ion batteries.* RSC Advances, 2014. 4(15): p. 7703-7709.

83. Zhuang;, Q.-C., et al., *Lithium Ion Batteries - New Developments*, in *Diagnosis of Electrochemical Impedance Spectroscopy in Lithium-Ion Batteries*, I. Belharouak, Editor 2012.

84. Su, X., et al., *Silicon-Based Nanomaterials for Lithium-Ion Batteries: A Review.* Advanced Energy Materials, 2014. 4(1): p. n/a-n/a.

85. Cheng, C., et al., *Hierarchical porous Co3O4 nanosheet arrays directly grown on carbon cloth by an electrochemical route for high performance Li-ion batteries.* New Journal of Chemistry, 2014.

86. Hwang, S.W., et al., *Low-temperature growth of well-crystalline Co3O4 hexagonal nanodisks as anode material for lithium-ion batteries.* Electrochimica Acta, 2011. 56(24): p. 8534.

87. Li, C.C., et al., *Topochemical synthesis of cobalt oxide nanowire arrays for high performance binderless lithium ion batteries.* Journal of Materials Chemistry, 2011. 21(32): p. 11867-11872.

88. Li, C.C., et al., *High capacity and excellent cycling stability of branched cobalt oxide nanowires as Li-insertion materials.* Applied Physics Letters, 2010. 97(4): p. -.

89. Whittingham, M.S., *Lithium Batteries and Cathode Materials.* Chemical Reviews, 2004. 104(10): p. 4271-4302.

90. Wu, B., et al., *Iron sulfide-embedded carbon microsphere anode material with high-rate performance for lithium-ion batteries.* Chemical Communications. 47(30): p. 8653-8655.

91. Chung, J.S. and H.J. Sohn, *Electrochemical behaviors of CuS as a cathode material for lithium secondary batteries.* Journal of Power Sources, 2002. 108(1-2): p. 226-231.

92. Kim, Y. and J.B. Goodenough, *Lithium Insertion into Transition-Metal Monosulfides: Tuning the Position of the Metal 4s Band.* The Journal of Physical Chemistry C, 2008. 112(38): p. 15060-15064.

93. Ji, X.L., K.T. Lee, and L.F. Nazar, *A highly ordered nanostructured carbon-sulphur cathode for lithium-sulphur batteries.* Nature Materials, 2009. 8(6): p. 500-506.

94. Yang, Y., et al., *Improving the Performance of Lithium–Sulfur Batteries by Conductive Polymer Coating.* ACS Nano, 2011. 5(11): p. 9187-9193.

95. Ji, X., K.T. Lee, and L.F. Nazar, *A highly ordered nanostructured carbon-sulphur cathode for lithium-sulphur batteries.* Nat Mater, 2009. 8(6): p. 500-506.

96. Vaughn, D.D., et al., *Formation of SnS nanoflowers for lithium ion batteries.* Chemical Communications, 2012. 48(45): p. 5608-5610.

97. Chang, K., et al., *Few-layer SnS2/graphene hybrid with exceptional electrochemical performance as lithium-ion battery anode.* Journal of Power Sources, 2012. 201(0): p. 259-266.

98. Fei, L., et al., *Reduced Graphene Oxide Wrapped FeS Nanocomposite for Lithium-Ion Battery Anode with Improved Performance.* ACS Applied Materials & Interfaces, 2013. 5(11): p. 5330-5335.

99. Jang, J.-t., et al., *Ultrathin Zirconium Disulfide Nanodiscs.* Journal of the American Chemical Society, 2011. 133(20): p. 7636-7639.

100. Shi, W., et al., *Controlled Synthesis of Carbon-Coated Cobalt Sulfide Nanostructures in Oil Phase with Enhanced Li Storage Performances.* ACS Applied Materials & Interfaces, 2012. 4(6): p. 2999-3006.

101. Lai, C.-H., et al., *Oriented growth of large-scale nickel sulfide nanowire arrays via a general solution route for lithium-ion battery cathode applications.* Journal of Materials Chemistry, 2009. 19(39): p. 7277-7283.

102. Li, T., et al., *Carbon-Coated Fe–Mn–O Composites as Promising Anode Materials for Lithium-Ion Batteries.* ACS Applied Materials & Interfaces, 2013. 5(19): p. 9470-9477.

103. Zhu, J., et al., *Synergetic approach to achieve enhanced lithium ion storage performance in ternary phased SnO2-Fe2O3/rGO composite nanostructures.* Journal of Materials Chemistry, 2011. 21(34): p. 12770-12776.

104. Wu, X., et al., *Coaxial SnO2@TiO2 nanotube hybrids: from robust assembly strategies to potential application in Li+ storage.* Journal of Materials Chemistry, 2012. 22(22): p. 11151-11158.

105. Zhou, W., et al., *Epitaxial Growth of Branched α-Fe2O3/SnO2 Nano-Heterostructures with Improved Lithium-Ion Battery Performance.* Advanced Functional Materials, 2011. 21(13): p. 2439-2445.

106. Qiao, L., et al., *Single electrospun porous NiO-ZnO hybrid nanofibers as anode materials for advanced lithium-ion batteries.* Nanoscale, 2013. 5(7): p. 3037-3042.

107. Wu, Z., L. Qin, and Q. Pan, *Fabrication and electrochemical behavior of flower-like ZnO–CoO–C nanowall arrays as anodes for lithium-ion batteries.* Journal of Alloys and Compounds, 2011. 509(37): p. 9207-9213.

108. Saadat, S., et al., *Coaxial Fe3O4/CuO hybrid nanowires as ultra fast charge/discharge lithium-ion battery anodes.* Journal of Materials Chemistry A, 2013. 1(30): p. 8672-8678.

109. Bogart, T.D., et al., *Lithium Ion Battery Peformance of Silicon Nanowires with Carbon Skin.* ACS Nano, 2013. 8(1): p. 915-922.

110. Mei, L., et al., *Superior electrochemical performance of ultrasmall SnS2 nanocrystals decorated on flexible RGO in lithium-ion batteries.* Journal of Materials Chemistry A, 2013. 1(30): p. 8658-8664.

111. Magasinski, A., et al., *High-performance lithium-ion anodes using a hierarchical bottom-up approach.* Nat Mater, 2010. 9(4).

112. Guo, J., X. Chen, and C. Wang, *Carbon scaffold structured silicon anodes for lithium-ion batteries.* Journal of Materials Chemistry, 2010. 20(24): p. 5035-5040.

113. Xing, W., et al., *Pyrolyzed Polysiloxanes for Use as Anode Materials in Lithium-Ion Batteries.* Journal of The Electrochemical Society, 1997. 144(7): p. 2410-2416.

114. Kepler, K.D., J.T. Vaughey, and M.M. Thackeray, *Li x Cu6Sn5 (0 < x < 13) : An Intermetallic Insertion Electrode for Rechargeable Lithium Batteries.* Electrochemical and Solid-State Letters, 1999. 2(7): p. 307-309.

115. Wang, X.-L., et al., *Nanospheres of a New Intermetallic FeSn5 Phase: Synthesis, Magnetic Properties and Anode Performance in Li-ion Batteries.* Journal of the American Chemical Society, 2011. 133(29): p. 11213-11219.

116. Besenhard, J.O., J. Yang, and M. Winter, *Will advanced lithium-alloy anodes have a chance in lithium-ion batteries?* Journal of Power Sources, 1997. 68(1): p. 87-90.

117. Guan, D., C. Cai, and Y. Wang, *Amorphous and crystalline TiO 2 nanotube arrays for enhanced Li-ion intercalation properties.* Journal of nanoscience and nanotechnology, 2011. 11(4): p. 3641-3650.

118. Wang, X.-L., et al., *Amorphous Hierarchical Porous GeOx as High-Capacity Anodes for Li Ion Batteries with Very Long Cycling Life.* Journal of the American Chemical Society, 2011. 133(51): p. 20692-20695.

119. Ku, J.H., et al., *Reversible Lithium Storage with High Mobility at Structural Defects in Amorphous Molybdenum Dioxide Electrode.* Advanced Functional Materials, 2012. 22(17): p. 3658-3664.

120. Avouris, P., *Graphene: Electronic and Photonic Properties and Devices.* Nano Letters, 2010. 10(11): p. 4285-4294.

121. Inagaki, M., Y.A. Kim, and M. Endo, *Graphene: preparation and structural perfection.* Journal of Materials Chemistry, 2011. 21(10): p. 3280-3294.

122. Yoo, E., et al., *Large Reversible Li Storage of Graphene Nanosheet Families for Use in Rechargeable Lithium Ion Batteries.* Nano Letters, 2008. 8(8): p. 2277-2282.

123. Novoselov, K.S., et al., *Two-dimensional gas of massless Dirac fermions in graphene.* Nature, 2005. 438(7065): p. 197-200.

124. Reddy, A.L.M., et al., *Synthesis Of Nitrogen-Doped Graphene Films For Lithium Battery Application.* ACS Nano, 2010. 4(11): p. 6337-6342.

125. Zhu, J., et al., *Facile synthesis of metal oxide/reduced graphene oxide hybrids with high lithium storage capacity and stable cyclability.* Nanoscale, 2011. 3(3): p. 1084-1089.

126. Jang, J., et al., *Ultrathin Zirconium Disulfide Nanodiscs.* Journal of the American Chemical Society, 2011. 133(20): p. 7636-7639.

127. Feng, C., et al., *Synthesis of molybdenum disulfide (MoS2) for lithium ion battery applications.* Materials Research Bulletin, 2009. 44(9): p. 1811-1815.

128. Chang, K. and W. Chen, *l-Cysteine-Assisted Synthesis of Layered MoS2/Graphene Composites with Excellent Electrochemical Performances for Lithium Ion Batteries.* ACS Nano, 2011. 5(6): p. 4720-4728.

129. Ramakrishna Matte, H.S.S., et al., *MoS2 and WS2 Analogues of Graphene.* Angewandte Chemie International Edition, 2010. 49(24): p. 4059-4062.

130. Schliehe, C., et al., *Ultrathin PbS Sheets by Two-Dimensional Oriented Attachment.* Science, 2010. 329(5991): p. 550-553.

131. Tang, Z., et al., *Self-Assembly of CdTe Nanocrystals into Free-Floating Sheets.* Science, 2006. 314(5797): p. 274-278.

132. Vaughn, D.D., S.-I. In, and R.E. Schaak, *A Precursor-Limited Nanoparticle Coalescence Pathway for Tuning the Thickness of Laterally-Uniform Colloidal Nanosheets: The Case of SnSe.* ACS Nano, 2011. 5(11): p. 8852-8860.

133. Cheng, F., et al., *Surfactant carbonization to synthesize pseudocubic α-Fe2O3/C nanocomposite and its electrochemical performance in lithium-ion batteries.* Electrochimica Acta, 2011. 56(16): p. 5593-5598.

134. Hassan, M.F., et al., *Solvent-assisted molten salt process: A new route to synthesise α-Fe2O3/C nanocomposite and its electrochemical performance in lithium-ion batteries.* Electrochimica Acta, 2010. 55(17): p. 5006-5013.

135. Seo, J., et al., *Two-Dimensional Nanosheet Crystals.* Angewandte Chemie International Edition, 2007. 46(46): p. 8828-8831.

136. Choi, J., et al., *SnSe2 nanoplate-graphene composites as anode materials for lithium ion batteries.* Chemical Communications, 2011. 47(18): p. 5241-5243.

137. Kim, B.-C., et al., *All solid state Li-ion secondary battery with FeS anode.* Solid State Ionics, 2005. 176(31-34): p. 2383-2387.

138. Tian, L., et al., *Synthesis of NiS and MnS Nanocrystals from the Molecular Precursors (TMEDA)M(SC{O}C6H5)2 (M = Ni, Mn).* Crystal Growth & Design, 2008. 9(1): p. 352-357.

139. Xu, Z., et al., *Oleylamine as Both Reducing Agent and Stabilizer in a Facile Synthesis of Magnetite Nanoparticles.* Chemistry of Materials, 2009. 21(9): p. 1778-1780.

140. Tang, Z. and N.A. Kotov, *One-Dimensional Assemblies of Nanoparticles: Preparation, Properties, and Promise.* Advanced Materials, 2005. 17(8): p. 951-962.

141. Wang, W.Z., et al., *High-yield synthesis of single-crystalline antimony telluride hexagonal nanoplates using a solvothermal approach.* Journal of the American Chemical Society, 2005. 127(40): p. 13792-13793.

142. Saadat, S., et al., *Template-Free Electrochemical Deposition of Interconnected ZnSb Nanoflakes for Li-Ion Battery Anodes.* Chemistry of Materials, 2011. 23(4): p. 1032-1038.

143. Kühnle, A., et al., *Adsorption of Dodecanethiol on Cu(110): Structural Ordering upon Thiolate Formation.* Langmuir, 2002. 18(14): p. 5558-5565.

144. O'Dwyer, C., et al., *Low-Dimensional, Hinged Bar-code Metal Oxide Layers and Free-Standing, Ordered Organic Nanostructures from Turbostratic Vanadium Oxide.* Small, 2008. 4(7): p. 990-1000.

145. Raman, N.K., M.T. Anderson, and C.J. Brinker, *Template-based approaches to the preparation of amorphous, nanoporous silicas.* Chemistry of Materials, 1996. 8(8): p. 1682-1701.

146. Xu, D., et al., *Solvothermal Synthesis of CdS Nanowires in a Mixed Solvent of Ethylenediamine and Dodecanethiol.* The Journal of Physical Chemistry B, 2005. 109(30): p. 14344-14349.

147. Choi, S., et al., *Simple and Generalized Synthesis of Semiconducting Metal Sulfide Nanocrystals.* Advanced Functional Materials, 2009. 19(10): p. 1645-1649.

148. Kuzuya, T., et al., *Synthesis of copper and zinc sulfide nanocrystals via thermolysis of the polymetallic thiolate cage.* Science and Technology of Advanced Materials, 2005. 6(1): p. 84-90.

149. Li, N., et al., *One-pot self-assembly of flower-like Cu2S structures with near-infrared photoluminescent properties.* CrystEngComm, 2011. 13(21): p. 6549-6554.

150. Zhuang, Z., et al., *A Facile "Dispersion–Decomposition" Route to Metal Sulfide Nanocrystals.* Chemistry – A European Journal, 2011. 17(37): p. 10445-10452.

151. Nan, C., et al., *Solvothermal synthesis of lithium iron phosphate nanoplates.* J Mater Chem, 2011. 21: p. 9994 - 9996.

152. Choi, S.-H., et al., *Simple and Generalized Synthesis of Semiconducting Metal Sulfide Nanocrystals.* Advanced Functional Materials, 2009. 19(10): p. 1645-1649.

153. Saadat, S., et al., *Template Free Electrochemical Deposition of ZnSb Nanotubes for Li Ion Battery Anodes.* Chemical Communications, 2011 47(35): p. 9849-9851.

154. Hansen;, K. and K. West. *Lithium Insertion into Iron Sulfides* in *Batteries for Portable Applications and Electric Vehicles* 1997. The Electrochemical Society

155. Golodnitsky, D. and E. Peled, *Pyrite as cathode insertion material in rechargeable lithium/composite polymer electrolyte batteries.* Electrochimica Acta, 1999. 45(1-2): p. 335-350.

156. Zhu, J.X., et al., *Facile synthesis of metal oxide/reduced graphene oxide hybrids with high lithium storage capacity and stable cyclability.* Nanoscale, 2011. 3(3): p. 1084-1089.

157. Chen, J.S., et al., *Constructing Hierarchical Spheres from Large Ultrathin Anatase TiO2 Nanosheets with Nearly 100% Exposed (001) Facets for Fast Reversible Lithium Storage.* Journal of the American Chemical Society, 2010. 132(17): p. 6124-6130.

158. Yang, Z., et al., *In situ synthesis of lithium sulfide-carbon composites as cathode materials for rechargeable lithium batteries.* Journal of Materials Chemistry A, 2013. 1(4): p. 1433-1440.

159. Ji, X., K.T. Lee, and L.F. Nazar, *A highly ordered nanostructured carbon-sulphur cathode for lithium-sulphur batteries.* Nat Mater, 2009. 8(6).

160. Zheng, S., et al., *In Situ Formed Lithium Sulfide/Microporous Carbon Cathodes for Lithium-Ion Batteries.* ACS Nano, 2013. 7(12): p. 10995-11003.

161. He, G., et al., *Tailoring Porosity in Carbon Nanospheres for Lithium–Sulfur Battery Cathodes.* ACS Nano, 2013. 7(12): p. 10920-10930.

162. Zhao, L., et al., *Bubble template synthesis of copper sulfide hollow spheres and their applications in lithium ion battery.* Materials Letters, 2012. 68(0): p. 28-31.

163. Wang, Q., et al., *CoS2 Hollow Spheres: Fabrication and Their Application in Lithium-Ion Batteries.* The Journal of Physical Chemistry C, 2011. 115(16): p. 8300-8304.

164. Wu, B., et al., *Iron sulfide-embedded carbon microsphere anode material with high-rate performance for lithium-ion batteries.* Chemical Communications, 2011. 47(30): p. 8653-8655.

165. Yang, J., et al., *Mesoporous Zinc-Blende ZnS Nanoparticles: Synthesis, Characterization and Superior Photocatalytic Properties.* Nanotechnology, 2008. 19(25): p. 255603.

166. Xu, C., et al., *Controlled Soft-Template Synthesis of Ultrathin C@FeS Nanosheets with High-Li-Storage Performance.* ACS Nano, 2012. 6(6): p. 4713-4721.

167. Zeng, Y., et al., *One-Step Solvothermal Synthesis of Single-Crystalline TiOF2 Nanotubes with High Lithium-Ion Battery Performance.* Chemistry, 2012. 18(13): p. 4026-30.

168. Zhu, J., et al., *Facile Synthesis of Metal Oxide/Reduced Graphene Oxide Hybrids with High Lithium Storage Capacity and Stable Cyclability.* Nanoscale, 2011. 3(3): p. 1084-9.

169. Zhu, J., et al., *Synergetic Approach to Achieve Enhanced Lithium Ion Storage Performance in Ternary Phased SnO2–Fe2O3/rGO Composite Nanostructures.* Journal of Materials Chemistry, 2011. 21(34): p. 12770.

170. Han, W. and M. Gao, *Investigations on Iron Sulfide Nanosheets Prepared via a Single-Source Precursor Approach.* Crystal Growth & Design 2008. 8(3): p. 1023-1030.

171. Zhu, J., et al., *Nanohybridization of ferrocene clusters and reduced graphene oxides with enhanced lithium storage capability.* Chemical Communications, 2011. 47(37): p. 10383-10385.

172. Wang, Z., et al., *[small alpha]-Fe2O3 nanotubes with superior lithium storage capability.* Chemical Communications, 2011. 47(28): p. 8061-8063.

173. Wang, B., et al., *Quasiemulsion-Templated Formation of α-Fe2O3 Hollow Spheres with Enhanced Lithium Storage Properties.* Journal of the American Chemical Society, 2011. 133(43): p. 17146-17148.

174. France Patent 1490725, 1966.

175. Guan, D., C. Cai, and Y. Wang, *Amorphous and Crystalline TiO2 Nanotube Arrays for Enhanced Li-Ion Intercalation Properties.* Journal of Nanoscience and Nanotechnology, 2011. 11(4): p. 3641-3650.

176. Ku, J.H., et al., *Reversible Lithium Storage with High Mobility at Structural Defects in Amorphous Molybdenum Dioxide Electrode.* Advanced Functional Materials, 2012: p. n/a-n/a.

177. Zhang, F., et al., *Controlled synthesis and gas-sensing properties of hollow sea urchin-like α-Fe2O3 nanostructures and α-Fe2O3 nanocubes.* Sensors and Actuators B: Chemical, 2009. 141(2): p. 381-389.

178. Liang, J., et al., *Synthesis of spindle-shaped α-FeOOH and α-Fe2O3 nanocrystals.* Crystal Research and Technology, 2011. 46(5): p. 493-496.

179. Tabuchi, T., et al., *Surface reaction of β-FeOOH film negative electrode for lithium-ion cells.* Journal of Power Sources, 2009. 191(2): p. 636-639.

180. Zhu, J., et al., *Hierarchical hollow spheres composed of ultrathin Fe2O3 nanosheets for lithium storage and photocatalytic water oxidation.* Energy & Environmental Science, 2013. 6(3): p. 987-993.

181. Zhang, W., et al., *Fe2O3 nanocluster-decorated graphene as O2 electrode for high energy Li-O2 batteries.* RSC Advances, 2012. 2(22): p. 8508-8514.

182. Sun, Z., X. Feng, and W. Hou, *Morphology-controlled synthesis of α-FeOOH and its derivatives.* Nanotechnology, 2007. 18(45): p. 455607.

183. Mansour, A.N. and R.A. Brizzolara, *Characterization of the Surface of alpha-FeOOH Powder by XPS.* Surface Science Spectra, 1996. 4(4): p. 357-362.

184. Zhang, C., et al., *Synthesis of hexagonal-symmetry [small alpha]-iron oxyhydroxide crystals using reduced graphene oxide as a surfactant and their Li storage properties.* CrystEngComm, 2012. 14(1): p. 147-153.

185. Wang, Y., A. Muramatsu, and T. Sugimoto, *FTIR analysis of well-defined α-Fe2O3 particles.* Colloids and Surfaces A: Physicochemical and Engineering Aspects, 1998. 134(3): p. 281-297.

186. Sing;, K.S.W., et al., *Reporting physisorption data for gas/solid systems with special reference to the determination of surface area and porosity.* Pure Appl. Chem., 1985. 57(4): p. 603-619.

187. Lou, X., X. Wu, and Y. Zhang, *Goethite nanorods as anode electrode materials for rechargeable Li-ion batteries.* Electrochemistry Communications, 2009. 11(8): p. 1696-1699.

188. Pinson, M.B. and M.Z. Bazant, *Theory of SEI Formation in Rechargeable Batteries: Capacity Fade, Accelerated Aging and Lifetime Prediction.* Journal of The Electrochemical Society, 2012. 160(2): p. A243-A250.

189. Arora, P., R.E. White, and M. Doyle, *Capacity Fade Mechanisms and Side Reactions in Lithium-Ion Batteries.* Journal of The Electrochemical Society, 1998. 145(10): p. 3647-3667.

190. Sikha, G., B.N. Popov, and R.E. White, *Effect of Porosity on the Capacity Fade of a Lithium-Ion Battery: Theory*. Journal of The Electrochemical Society, 2004. 151(7): p. A1104-A1114.

191. Guerrero, A., et al., *Recombination in Organic Bulk Heterojunction Solar Cells: Small Dependence of Interfacial Charge Transfer Kinetics on Fullerene Affinity*. J. Phys. Chem. Lett., 2012. 3: p. 1386−1392.

192. Li, X., et al., *Batteries: Tin Oxide with Controlled Morphology and Crystallinity by Atomic Layer Deposition onto Graphene Nanosheets for Enhanced Lithium Storage (Adv. Funct. Mater. 8/2012).* Advanced Functional Materials, 2012. 22(8): p. 1646-1646.

193. Wang, Z., et al., *Amorphous CoSnO3@C nanoboxes with superior lithium storage capability*. Energy & Environmental Science, 2013. 6(1): p. 87-91.

194. Xiang, J.Y., et al., *Electrochemical Impedance Analysis of a Hierarchical CuO Electrode Composed of Self-Assembled Nanoplates.* The Journal of Physical Chemistry C, 2011. 115(5): p. 2505-2513.

195. Wang, C., A.J. Appleby, and F.E. Little, *Electrochemical impedance study of initial lithium ion intercalation into graphite powders.* Electrochimica Acta, 2001. 46(12): p. 1793-1813.

196. Wang, C. and J. Hong, *Ionic/Electronic Conducting Characteristics of LiFePO4 Cathode Materials: The Determining Factors for High Rate Performance.* Electrochemical and Solid-State Letters, 2007. 10(3): p. A65-A69.

197. Ponrouch, A. and M.R. Palacín, *Optimisation of performance through electrode formulation in conversion materials for lithium ion batteries: Co3O4 as a case example.* Journal of Power Sources, 2012. 212(0): p. 233-246.

198. Khatib, R., et al., *Origin of the Voltage Hysteresis in the CoP Conversion Material for Li-Ion Batteries.* The Journal of Physical Chemistry C, 2013. 117: p. 837–849.

199. McKinnon, W.R. and R.R. Haering, *Physical mechanisms of intercalation*, in *Modern Aspects of Electrochemistry*, R.E. White, J.O.M. Bockris, and B.E. Conway, Editors. 1983, Plenum Press: New York. p. 235-304.

200. Gao, Y., J.N. Reimers, and J.R. Dahn, *Changes in the voltage profile of li/Li1+xMn2-xO4 cells as a fuction of x.* Physical Review B, 1996. 54: p. 3878-3883.

201. Bisquert, J. and V.S. Vikhrenko, *Analysis of the kinetics of ion intercalation. Two state model describing the cpupling of solid state ion diffusion and ion binding processes.* Electrochimica Acta, 2002. 47: p. 3977-3988.

202. Khatib, R., et al., *Origin of the Voltage Hysteresis in the CoP Conversion Material for Li-Ion Batteries.* J. Phys. Chem. C, 2013. 117: p. 837−849.

203. Bisquert, J., *Chemical Capacitance of Nanostructured Semiconductors: its Origin and Significance for Heterogeneous Solar Cells.* Phys. Chem. Chem. Phys., 2003. 5: p. 5360-5364.

204. Garcia-Belmonte, G., et al., *Relaxation processes in the coloration of amorphous WO3 thin films studied by combined impedance and electro-optical measurements.* Journal of Applied Physics, 2004. 96: p. 853-859.

205. Khatib, R., et al., *Origin of the Voltage Hysteresis in the CoP Conversion Material for Li-Ion Batteries.* The Journal of Physical Chemistry C, 2012. 117(2): p. 837-849.

206. Hong, E., D. Kim, and J.H. Kim, *Heterostructured metal sulfide (ZnS–CuS–CdS) photocatalyst for high electron utilization in hydrogen production from solar water splitting.* Journal of Industrial and Engineering Chemistry, 2014. 20(5): p. 3869-3874.

8. Publication List

1. **Chen Xu**, Yi Zeng, Xianhong Rui, Ni Xiao, Jixin Zhu, Wenyu Zhang, Jing Chen, Huiteng Tan, Huey Hoon Hng, Qingyu Yan*, "Controlled Soft-Template Synthesis of Ultra-thin C@FeS Nanosheets with High Li Storage Performance", ACS NANO 6, (2012), p4713.

2. **Chen Xu**, Yi Zeng, Xianhong Rui, Jixin Zhu, Huiteng Tan, Antonio Guerrero, Juan Toribio, Juan Bisquert, Germà Garcia-Belmonte*, Qingyu Yan*, "Amorphous Iron Oxyhydroxide Nanosheets: Synthesis, Li Storage and Conversion Reaction Kinetics". J. Phys. Chem. C 117 (34), (2013), p17462-17469.

3. **Chen Xu**, Shengjie Peng, Chaoliang Tan, Huixiang Ang, Huiteng Tan, Hua Zhang, Qingyu Yan*, "Ultrathin S-doped $MoSe_2$ nanosheets for Efficient Hydrogen Evolution", Journal of Materials Chemistry A 2 (16), (2014), p5594-5601.

4. Huiteng Tan, Xianhong Rui, Hong Yu, Weiling Liu, **Chen Xu**, Zhichuan Xu, Hueyhoon Hng, Qingyu Yan*, "An Aqueous-Based Chemical Route towards Ambient-Preparation ofMulticomponents Core-Shell Nanotubes", ACS NANO 8 (4), (2014), p4004

5. Wenyu Zhang, Jixin Zhu, Huixiang Ang, HaiboWang, Hui Teng Tan, Dan Yang, **Chen Xu**, Ni Xiao, Bing Li, Weiling Liu, Xin Wang, Huey Hoon Hng, Qingyu Yan*, "Fe-based metallopolymernanowall-based composites for Li-O_2 battery cathode", ACS Applied Materials & Interfaces (2014 accepted)

6. Hui Teng Tan, Xianhong Rui, Wenhui Shi, **Chen Xu**, Hong Yu, Harry E. Hoster, Qingyu Yan*, "Controlled Synthesis of Nanostructured Manganese Oxyhydroxide Nanotubes: Implication for High-Power High-Energy Supercapaitor", ChemPlusChem, 78 (3), (2013), p218.

7. Wenyu Zhang, Yi Zeng, **Chen Xu**, Huiteng Tan, Weiling Liu, Jixin Zhu, Ni Xiao, Huey Hoon Hng, Jan Ma, Harry E. Hoster, Rachid Yazami, Qingyu Yan*, "Fe_2O_3 Nanoclusters Decorated Graphene as O_2 Electrode for High Energy Li-O_2 batteries", RSC Advances 2 (22), (2012), p8508

8.Wenyu Zhang, Yi Zeng, **Chen Xu**, Ni Xiao, Yiben Gao, Lain-Jong Li, Xiaodong Chen, Huey Hoon Hng, Qingyu Yan*, "A facile approach to nanoarchitectured three-dimensional graphene-based Li-Mn-O composite as high-power cathodes for Li-Ion batteries", Beilstein Journal of Nanotechnology 3, (2012), p513

9. Jixin Zhu, Kuo Sun, Daohao Sim, **Chen Xu**, Hua Zhang, Huey Hoon Hng and Qingyu Ya*, "Nanohybridization of ferrocene clusters and reduced graphene oxides with enhanced lithium storage capability" Chemical Communications 47 (37), (2011) 10383 – 10385

10. Xianhong Rui, Jixin Zhu, Daohao Sim, **Chen Xu**, Yi Zeng, Huey Hoon Hng, Tuti Mariana Lim,* and Qingyu Yan*, "Reduced Graphene Oxide Supported Highly Porous V_2O_5 Spheres as a High-Power Cathode Material for Lithium Ion Batteries", Nanoscale 3 (11), (2011) 4752-4758.

11. Xianhong Rui, Daohao Sim, **Chen Xu**, Weiling Liu, Huiteng Tan, Kangming Wong, Huey Hoon Hng, Tuti Mariana Lim,* and Qingyu Yan*, "One-pot synthesis of carbon-coated VO_2(B)nanobelts for high-rate lithium storage", RSC Advances, 2(3), (2012), p1174 – 1180

9. Appendix

In the subcircuit modeling the conversion reaction, the chemical capacitance C_μ^c can be expressed as:

$$C_\mu^c = qL\frac{\partial c}{\partial V}. \tag{1}$$

(where q is the positive elementary charge, and L represents the electrode thickness.)

We assume that the MX lattice contains N_0 sites where Li^+ ions can diffuse and a total of N_1 atoms of type X per unit volume that form sites where Li^+ ions can react with. $n \le N_0$ is the concentration of diffusing ions in the framework with energy E_0 (we assume $n << N_0$) and $c \le N_1$ is the concentration of Li^+ that have reacted with the formation of LiX with energy E_1. The equilibrium chemical potential of Li^+ is

$$\mu = \mathrm{E}_0 + k_B T \ln\left(\frac{n}{N_0}\right) = E_1 + k_B T \ln\left(\frac{c}{N_1 - c}\right) \tag{2}$$

As lithiation or de-lithiation process proceeds, any change of voltage will bring about change in Li^+ concentration in the LiMX particle. The mobile Li^+ concentration at the surface relates to the voltage as

$$n = N_0 e^{-(E_0 - qV)/k_B T} \tag{3}$$

This process, including Li^+ entering the particle, diffuse inside the framework and participating in the conversion reaction, can be described by the kinetic equations

$$\frac{\partial n}{\partial t} = -\frac{\partial J_n}{\partial x} - k_1 n(N_1 - c) + k_2 c(N_0 - n) \tag{4}$$

$$\frac{\partial c}{\partial t} = k_1 n(N_1 - c) - k_2 c(N_0 - n) \tag{5}$$

Here J_n is the flux at position x, and $k_{1,2}$ correspond to the kinetic constants. For simplicity, we consider a one-dimensional system of thickness L so that the injected current is $j = qJ_n(0)$ and $J_n(L) = 0$. Considering homogeneous n and c, equation (4) can be integrated to equation (6):

$$\frac{\partial n}{\partial t} = \frac{J_n(0)}{L} - k_1 n(N_1 - c) + k_2 c(N_0 - n) \tag{6}$$

In equilibrium the current is zero and we obtain

$$\frac{k_1}{k_2} = \frac{N_0 \bar{c}}{\bar{n}(N_1 - \bar{c})} \tag{7}$$

Since we assume that k_1 and k_2 are constant, the detailed balance condition is

$$\frac{k_1}{k_2} = e^{(E_0 - E_1)/k_B T} \tag{8}$$

In transient or voltage modulated conditions, n is modulated by the external potential while c will change towards the equilibrium value indicated in Equation (2). For a modulation of the density $n = \bar{n} + \hat{n}$, we find by Equation (3) that the free ion density modulation depends on voltage modulation as

$$\hat{n} = \frac{c_\mu^n}{q}\hat{V} \tag{9}$$

Here the chemical capacitance can be represented by:

$$c_{\mu}^{n} = q\frac{\partial n}{\partial V} = \frac{q^2 n}{k_B T} \tag{10}$$

Similarly we define a chemical capacitance for the Li^+ occupying LiX sites:

$$c_{\mu}^{c} = q\frac{\partial c}{\partial V} = \frac{q^2 c(N_1 - c)}{N_1 k_B T} \tag{11}$$

It should be observed from Equation 11 that the chemical capacitance is correlated to the derivative of the voltage-composition curve, but is not related to charge separation at the interface.[203] In the simple model outlined here c_{μ} is given by the entropy of ions in equivalent cites. In general c_{μ} relates to the dependence of the chemical potential on the concentration and depends on any chemical force over the ions in the solid phase.

Modulation of the voltage with angular frequency ω changes the free ion density resulting in a change in the reacted density as $c(t) = \bar{c} + \hat{c}$. By a Laplace transform and expanding to first order, the reacted density can be represented by:

$$\hat{c} = \frac{k_1(N_1 - \bar{c})}{\omega_{cr} + i\omega}\hat{n} \tag{12}$$

Where

$$\omega_{cr} = k_1\bar{n} + k_2 N_0 \tag{13}$$

ω is the characteristic kinetic frequency of the conversion reaction. On the other hand, Equation (6) gives

$$\left[i\omega + k_1\left(N_1 - c\right)\right]\hat{n} = \left(k_1\bar{n} - k_2 N_0\right)\hat{c} + \frac{\hat{J}_n}{L} \tag{14}$$

Combining Equation (9), (10) and Equation (14):

$$\left(C_\mu^n i\omega + \frac{C_\mu^c i\omega}{1 + i\omega/\omega_{cr}}\right)\hat{V} = \hat{j} \tag{15}$$

In this equation, $C_\mu^n = Lc_\mu^n$ and $C_\mu^c = Lc_\mu^c$ are chemical capacitances per unit area. The admittance is defined as $Y = \hat{j}/\hat{V}$, therefore we have

$$Y = C_\mu^n i\omega + {Z_{cr}}^{-1} \tag{16}$$

Where

$$Z_{cr} = R_{cr} + \frac{1}{C_\mu^c i\omega} \tag{17}$$

Here we have introduced the resistance of the conversion reaction R_{cr} given by

$$\begin{aligned} {R_{cr}}^{-1} &= C_\mu^c \omega_{cr} \\ &= \frac{Lq^2}{N_1 k_B T}\bar{c}\left(N_1 - \bar{c}\right)\left(k_1\bar{n} + k_2 N_0\right) \end{aligned} \tag{18}$$

The impedance model in Eq. (16) is correlated to to the previously introduced equivalent circuit.